Computational studies in zeolite science : an investigation of guest-host interactions

COMPUTATIONAL STUDIES IN ZEOLITE SCIENCE;

AN INVESTIGATION OF GUEST-HOST INTERACTIONS

COMPUTATIONAL STUDIES IN ZEOLITE SCIENCE;

AN INVESTIGATION OF GUEST-HOST INTERACTIONS

Proefschrift

door

Constantinus Johannes Jacobus den Ouden

geboren te Dordrecht

Dit proefschrift is goedgekeurd door de promotoren:

prof. dr. R.A. van Santen
en
prof. dr. A.K. Cheetham

copromotor: dr. M.F.M. Post

Voor Karin
Aan mijn ouders

The chapters of this thesis have been published recently:

Chapter II
1. B. Smit, C.J.J. den Ouden, J. Phys. Chem, 1988, <u>92</u>, p. 7169
Chapter III
2. S.D. Pickett, A.K. Nowak, J.M. Thomas, B.K. Peterson, J.F.P. Swift, A.K. Cheetham, C.J.J. den Ouden, B. Smit, M.F.M. Post, J. Phys. Chem, 1990, <u>94</u>, p. 1233
3. A.K. Nowak, C.J.J. den Ouden, S.D. Picket, B. Smit, A.K. Cheetham, M.F.M. Post, J.M. Thomas, J. Phys. Chem, 1991, <u>95</u>, p. 848
Chapter IV
4. C.J.J. den Ouden, K.P. Datema, F. Viser, M. Mackay, M.F.M. Post, Zeolites, in press
Chapter V
5. C.J.J. den Ouden, A.F.H. Wielers, H.P.C.E. Kuipers, M. Vaarkamp, M. Mackay, M.F.M. Post, Stud. Surf. Sc. and Catal., 1989, <u>32</u>, p. 825
6. C.J.J. den Ouden, R.A. Jackson, C.R.A. Catlow, M.F.M. Post, J. Phys. Chem, 1990, <u>94</u>, p. 5286
Miscellaneous
7. C.J.J. den Ouden, B. Smit, A.F.H. Wielers, R.A. Jackson, A.K. Nowak, Mol. Sim., 1989, <u>4</u>, p. 121
8. B. Smit, C.J.J. den Ouden, Nederlands Tijdschrift voor Natuurkunde, 1989, <u>A55</u>, p. 82
9. K.P. Datema, C.J.J. den Ouden, W.D. Ijlstra, M.F.M. Post, H.P.C.E. Kuipers, J. Am. Chem. Soc., Far. Trans. II, in press
10. R.A. van Santen, D.P. de Bruyn, C.J.J. den Ouden, B. Smit, Stud. Surf. Sc. and Catal., 1991, <u>58</u>, p. 317

Published work but not described in this thesis:

11. G. Ooms, R.A. van Santen, C.J.J. den Ouden, R.A. Jackson, C.R.A. Catlow, J. Phys. Chem., 1988, <u>92</u>, p. 4462
12. R.A. van Santen, G. Ooms, C.J.J. den Ouden, B.W. van Beest, M.F.M. Post, Symp. Proc. "Advances in Zeolite Synthesis", ACS meeting, Los Angeles 1988
13. J.J. Keijsper, C.J.J. den Ouden, M.F.M. Post, Stud. Surf. Sc. and Catal., 1989, <u>32</u>, p. 237
14. C.J.J. den Ouden, R.W. Thompson, J. Coll. Int. Sci., in press
15. C.J.J. den Ouden, R.W. Thompson, Ind. Eng. Chem., submitted

CONTENTS

CHAPTER I

INTRODUCTION

At present, a new way of thinking is introduced in science. Although the questions asked are rather simple, the answers seem to be too complex to be expressed in terms of *Euclidean* geometry, classical mechanics or even quantum mechanics. Imagine yourself asking the question what causes the shape of a particular cloud at a particular place and time. You can take a photograph of this cloud and use this photograph to find an exact copy of the cloud, anytime, anywhere. You may find clouds which are very similar and just differ in a very few details. You may find clouds which are even more similar, but differ slightly in color. But no matter how long your search goes on, you will never find an exact copy of your cloud.

Clearly, classical *Euclidean* geometry cannot describe the existence and time-evolvement of the shape of the cloud since it would take an infinite number of *Euclidean* "building units" (lines, triangles, circles etcetera) for the entire description of the shape of the cloud. Modern mathematics, however, offers an opportunity for this description. But not only clouds. Also the shapes of the waves in the ocean, the paths of blood vessels, the shape of the Mount Everest and even the shapes of the trees in your back yard. The description stems from a theory which is based on chaos: Fractal theory. This theory states that all (chaotic) natural shapes can be described by a few input parameters and a set linear transformations. In this way, the complexity of natural shapes is reduced to a mathematical formulation. The visualization is realized by computer algorithms and a graphical interface.

Another question you may be asking yourself is how a gas molecule behaves in time. This question can readily be answered by quantum mechanics by solving the time-dependent *Schrodinger*-equation. The accuracy of the answer depends solely on the level of sophistication of the method chosen (size of basis set, Extended *Huckel* or a full Configuration Interaction calculation). Quantum mechanics orders nature and provides us with an answer applicable for isolated molecules only. However, quantum mechanical calculations become too complex and too time-consuming for a system consisting of hundred or thousand molecules interacting with each other; the number of molecules in a real system is typically of the order of 10^{23} and doesn't look orderly anymore. If it is proven in some way or another that this system can be simulated properly with hundred molecules, then it has to be concluded that quantum mechanics fails to describe the system under consideration. Particular for this reason, new computational (computer) techniques have been developed to bridge the gap between quantum mechanics and the chaotic reality which manifests itself by macroscopic properties such as adsorption enthalpies for gas-solid systems and phase equilibria for gas-liquid interfaces. In many cases, however, the basis of computer simulation is founded by quantum mechanics since intermolecular interactions, and especially the form and

parameters of these interactions, can readily be determined with quantum mechanical methods.

Chaos is difficult to deal with. A chaotic system is hard to study since possible regularities are obscured and it never exposes itself in a steady state. Taking a snapshot of a dynamic chaotic system will not be representative for the state the system is in since every other snapshot would have yielded a different state. Taking ten snapshots and averaging over these snapshots would be quite an improvement for the description of the system. Taking hundred snapshots and subsequent averaging would be better, however. The question arises: how may snapshots are required in order to arrive at a representative image of the system under study. This question is the basic issue of computer simulation, and computer simulation is the basic issue of this thesis.

To simulate chaos, one first has to create order. The natural shapes evolving from fractal theory are obtained by applying well defined algebraic transformations. In principle, all shapes are pre-determined, but the human mind loses control due to the increasing complexity.

Apart from chaos in shaping as described by fractal theory, also chaos in the dynamics of many-body systems is recognized. Examples are the movements of people in a crowed street or the dynamics of a number of gas molecules compressed in a volume as has already been discussed before. The simulation of the chaos for such a dynamic system consists of creating interaction "rules", and subsequently let the system go while applying the rules.

The correspondence between shape description by fractal theory and the simulation of a chaotic dynamic system will be obvious. In principle both theories are deterministic, but due to the complexity you can never predict the result. Furthermore, both theories have gained interest over the last few years due to increasing computer power and the development of numerical procedures for the realization of these theories.

This thesis deals with the simulation of processes which occur in the extended field of zeolite science and technology. These processes might be either static or dynamic, but since they are processes occurring in a natural system, they seem to be based on chaos. The aim of this thesis is to define rules with which this chaos can be described and understood. Because the computational methods used in this thesis have their basis outside the scope of zeolite research (especially computer simulation of liquids), the fundamentals have been described in detail elsewhere. Therefore, the main point of interest in this thesis is the application of these computational techniques in zeolite research. Before going into detail about the studies described in this thesis, however, first a brief description of the nature, composition and applications of zeolites will be given in the following part of this chapter.

Zeolites are microporous (alumino-) silicates. Since all zeolites are highly crystalline, the zeolite class of crystalline solids has been a subject of interest for many crystallographers and hence many structure determinations have been performed. In general, a zeolite lattice is built up from SiO_4 and AlO_4^- tetrahedra which are linked together via bridging oxygen atoms thus forming a three-dimensional network. If aluminum is built in the zeolite lattice at framework sites (also denoted as T-sites), a negative charge is introduced on the lattice which has to be compensated. Either inorganic or organic cations can serve for charge compensation. A further point worth mentioning is that the so-called *Loewenstein's* rule forbids Al-O-Al sequences to occur. This rule effectively restricts the zeolitic Al/Si ratio to vary between 0 (siliceous zeolites) and 1. This ratio can be considered as an indication for the zeolite chemical composition.

It can be envisaged that the linkage of the SiO_4 and AlO_4^- tetrahedra can be performed in many ways. Each way of linking will yield a different three-dimensional network, resulting in numerous possible network topologies. Quite a number of these structures represent zeolite networks, some of these structures being characterized by the presence of cages and other by the presence of one-, two- or three-dimensional channel systems. The number of known zeolite structures has increased considerably over the last three decennia with the discovery of new (synthetic) zeolites. In early times, zeolites were mainly natural minerals. The development of zeolite synthesis procedures, however, has resulted in a number of novel structures which have not been found in nature. Generally speaking, synthetic zeolites are characterized by low Al/Si ratios, although exceptions do occur.

Only very recently, a new class of microporous solids has been discovered and explored. The framework structures found in this class strongly resemble the structures found in the zeolite class. Instead of aluminum and silicon, the frameworks in this class are built up from aluminum and phosphorus and that is the reason that this class is denoted as AlPO's.

What makes zeolites so special and what makes them worthwhile to study? First of all, the number of (possible) zeolite structures appears to be nearly unlimited. This abundance of possible structures and the factors governing the formation of certain networks is a challenge for zeolite chemists.

Secondly, since zeolites are crystalline structures, their frameworks exhibit an infinite regularity. Furthermore, due to the presence of micropores, the internal surface of zeolites is very large which is advantageous in catalytic applications. The regularity combined with a large internal surface guarantees a constant catalytic activity throughout the entire zeolite crystal. As will be clear from the foregoing, zeolites are used as catalysts in several processes in the (petro-) chemical and oil industries which explains the high activity of zeolite research in both academic and industrial laboratories.

One of the main applications of zeolites is as a cracking catalyst in the oil-processing industries. For cracking reactions of heavy hydro carbon molecules, an extreme acidic catalyst has to be used. For this purpose, zeolite Y is ion-exchanged to the NH_4^+ form (as-synthesized Y has commonly Na^+ occluded for charge balancing purposes) and subsequently calcined to the H^+ form (the acidic form). This proton serves as an acidic catalytic site for cracking reactions. Furthermore, since the cations in zeolites are easily exchangeable, also catalytic active metal ions can be introduced in the micropore void space to catalyze reactions other than those requiring carbenium ions as intermediates (e.g. Ni^{2+}). In this way, catalytic activity can be fine-tuned to every desired degree. Finally, zeolites are unique for catalysis applications because the micropores have dimensions comparable to the sizes of the molecules which have to be converted. These micropore dimensions allows one to introduce and influence product selectivity by choosing different zeolite structures. This feature is the underlying reason for the high selectivities sometimes observed in zeolite catalysis. Such high selectivities can never be realized by amorphous microporous catalysts.

This thesis is a collection of various computer simulations applied in various areas of zeolite science and technology. As will become clear in the course of this thesis, comparison with experimental data plays a central role in computer simulation. Especially comparison with

spectroscopic data (such as e.g. NMR and IR) will appear to yield interesting results since spectroscopy techniques give direct information on a microscopic (molecular) level. Because computer simulation aims at the prediction of macroscopic properties starting from a microscopic level, spectroscopy is an indispensable tool to verify computational results. However, as will be shown in this thesis, computer simulation techniques have come up to such a level of sophistication that they can be used the other way around; spectroscopy results can be interpreted by computer simulation.

As already said before, computer simulation facilities require close contacts between theorists and experimentalists. Furthermore, these contacts are challenging and give new directions and guidelines to both experimental and theoretical research. The problems under study in this thesis clearly illustrate the close collaboration between various disciplines in chemistry in general and catalysis research in particular. Without this collaboration, the systems under study would probably have been quite different and the interpretation of the computational results less meaningful. All simulations described in this thesis were performed next to the laboratory where the zeolites used for the measurements were synthesized. All researchers, including the author of this thesis, were involved in every stage of the study; spectroscopists talked directly to zeolite chemists and theorists discussed about their results with catalysis experts. It is hoped that the atmosphere of this thesis represents the multidisciplinar collaboration which has taken place over the past four years.

The description of heterogeneous catalysis, such as zeolite catalysis, falls apart in a chemical and a physical part. The chemical part obviously describes the chemical processes which are taking place on the catalytic surface. The (molecular) mass transport processes are purely physical from origin. Phenomenological descriptions of heterogeneous catalysis processes generally make use of the *Thiele* modulus concept. The *Thiele* modulus is the ratio of the chemical reaction rate at the catalytic surface and the mass transport rate. The molecular basis of mass transport and adsorption in microporous solids is suitable to study with computer simulation techniques. This implies that the physical aspects of heterogeneous catalysis can be studied on a molecular level. This knowledge may ultimately be of direct importance for the development of shape selective zeolite catalysts for a particular application.

Adsorption characteristics are easily simulated by means of Monte Carlo procedures. Chapter II deals with these methods, and the features of such simulations are illustrated by the study of methane adsorption in various zeolites and under various conditions. The dynamics of adsorbates occluded in the zeolite micropores are highlighted in Chapter III. This chapter describes Molecular Dynamics procedures and simulations of xenon, methane, ethane and propane diffusion in various zeolites under various conditions. The strengths and potentials of both the Monte Carlo and Molecular Dynamics procedures will be pointed out, but also the weaknesses and pitfalls of the procedures and underlying assumptions will be discussed. Both in Chapter II and Chapter III, a thorough comparison with experimental data will be made in order to verify the computational results.

Whereas Chapter II and III dealt with the interactions between zeolite hosts and adsorbed (organic) guest molecules, Chapter IV describes the interactions between zeolite hosts and organic guest molecules which are occluded during the zeolite synthesis. During synthesis, the

crystallization of zeolites might be accompanied with the encapsulation of organic cations which are thought to act as structure directing agents. For example, the conventional structure directing agent for the synthesis of zeolite Sodalite is the Tetra-Methyl Ammonium (TMA) cation. In Chapter IV, the dynamics of TMA occluded in zeolite Sodalite is investigated. For this study, deuterated TMABr has been synthesized and subsequently been used for Sodalite synthesis. The as-made Sodalite with the deuterated TMA occluded was subjected to ^{2}H-NMR and ^{13}C-NMR analyses in order to elucidate the dynamics of the occluded TMA species. Molecular Dynamics simulations with a high degree of complexity were applied to interpret the experimental results; it appeared that the dynamics of the zeolite lattice was of utmost importance for the interpretation of the NMR results.

In a foregoing part of this chapter, it has already been discussed that the catalytic activity of zeolites can be modified by introducing (transition) metal ions in the zeolitic void spaces. Usually, these metal ions are introduced via ion-exchange methods. In Chapter V the question is raised how ion-exchange phenomena can be rationalized and where the metal ions are located after ion-exchange. The study will focus on exchange phenomena observed with siliceous zeolites and an analytical statistical model and a Monte Carlo random sampling model has been developed in order to describe the ion-exchange observations for divalent cations (Ni^{2+}). The models are further justified by IR spectroscopy. The assumptions made in the models concerning the locations of the divalent cations were verified by applying lattice energy minimization calculations.

CHAPTER II

MONTE CARLO SIMULATIONS OF METHANE ADSORPTION IN ZEOLITES

II.1 Introduction

Zeolites are characterized by the presence of micropores and thus the presence of a large internal surface formed by the inner walls of the micropores. Therefore, zeolites are used as ion-exchangers, gas separators and catalysts on a very large scale in several industrial processes[1a,1b]. Zeolites are particularly useful because of their ability to adsorb selectively various chemical compounds and/or to convert them into more useful products. So, both from a scientific point of view and a practical point of view, it is of vital importance to have a detailed understanding of the factors which govern the adsorption of molecules in zeolites. However, our knowledge of the energetics of the interaction of the adsorbate with the zeolitic environment and the influence of the geometric parameters of the zeolite lattice as well as its chemical composition on the energetics of interaction is rather poor.

This gap in knowledge motivated *Yashonath et. al.*[2] to use computer simulations to study the adsorption of methane in zeolite Na-Y (Faujasite or FAU structure). In their work, the influence of the temperature on the heat of adsorption has been studied and special attention has been paid to the average distribution of the methane molecules inside the micropores of Na-Y as a function of the temperature. A good agreement with the experimental heat of adsorption for this particular zeolite was obtained.

A well known problem in computer simulations of complex systems, such as eg. the methane-zeolite system, is that the choice of the potentials and the parameters of these potentials is not unique. So, a practical justification of this choice could be a comparison with various experimental values. In order to be able to make a more extensive comparison with experimental results, the work of *Yashonath et. al.*[2] has been extended by studying the influence of the temperature and Al/Si ratio on the heat of adsorption of methane in a series of different zeolite structures. The results of this study are described in this chapter.

The zeolites under consideration are Mordenite (MOR), ZSM-5 (MFI) and zeolite Y (FAU). The choice of this particular set of zeolite structures allows the study of differences in pore diameter. Zeolite FAU is considered as a wide pore structure (i.e. an effective pore diameter of approximately 8 A). MOR also belongs to the class of wide-pore zeolites but exhibits a slightly smaller pore diameter (7 A). Finally, MFI belongs to the class of medium pore zeolites (with an effective pore diameter of approximately 5.5 A). Furthermore, the different zeolite structures show some interesting differences in lattice topology. Zeolite FAU is built up from cavities. MOR and MFI on the other hand, are characterized by the presence of an one- and three-dimensional channel system, respectively.

The adsorption behavior, especially average siting of methane molecules in the different zeolite lattices, will be visualized by using computer graphics.

II.2 Model and Computational Details

In the simulations, the following approximations have been used:
- no adsorbate-adsorbate interactions are considered, indicating that all calculations correspond to low coverage of adsorbates in the zeolite host lattice (zero-filling approximation),
- the zeolite lattice as well as the adsorbate molecules are considered to be rigid.

With these assumptions, the potentials contain only adsorbate-zeolite interactions and can be approximated by[3]:

$$U - \sum_i \sum_j \phi_{ij} \qquad (II.1)$$

wherein i and j run over all the atoms in the adsorbate molecule and in the zeolite, respectively.

It is assumed that Φ_{ij} is a *Lennard-Jones* type potential combined with a Coulombic interaction term:

$$\phi_{ij} - \frac{B_{ij}}{r_{ij}^{12}} - \frac{A_{ij}}{r_{ij}^{6}} + \left(\frac{N_{av}e^2}{4000\pi e_0} \right) \left(\frac{q_i q_j}{r_{ij}} \right) \qquad (II.2)$$

The charge on atom i is given by q_i, e is the unit charge and N_{av} is *Avogadro's* number. The interatomic distance between atom i and atom j is represented by r_{ij}. A_{ij} and B_{ij} are the constants of dispersion attraction and repulsion, respectively.

Table II.1
Lennard-Jones parameters and atomic charges

Adsorbate	Lennard-Jones parameters Zeolite			
	A (kJ.Å6.mol-1) O	Na	B (kJ.Å12.mol-1) O	Na
C	1715.9	554.7	1016900	698500
H	508.2	169.6	111800	75800
Atomic charges				
Atom			q	
C (adsorbate)			0.0700	
H (adsorbate)			-0.0175	
Si, Al (zeolite)			equation II.6	
Na (zeolite)			1.0000	
O (zeolite)			-0.7000	

The values of the parameters A_{ij} and B_{ij} for the interaction between a hydrocarbon and a zeolite are listed in Table II.1. The values of the parameters are derived from the *Kirkwood* relation[2,3]:

$$A_{ij} = \frac{6mc^2\alpha_i\alpha_j}{\dfrac{\alpha_i}{X_i} + \dfrac{\alpha_j}{X_j}} \tag{II.3}$$

wherein α and X are the atomic polarizability and magnetic susceptibility, respectively. The value of the parameter B is obtained via the constraint that for $r_{ij}=r_0$, r_0 being the sum of the atomic radii of atom i and atom j, the *Lennard-Jones* interaction energy between both atoms is most favourable:

$$\left(\frac{d\phi_{ij}}{dr_{ij}}\right)_{r_{ij}=r_0} = 0 \tag{II.4}$$

from which, with the aid of equation (II.2), it readily follows that:

$$B_{ij} = \frac{1}{2}A_{ij}(r_i+r_j)^6 \tag{II.5}$$

Note that, owing to the size and polarizability of the silicon and aluminum atoms in the zeolite lattice, the contribution of these atoms to the *Lennard-Jones* potential is negligible, and therefore only the contribution of oxygen and sodium is considered. The atomic charges for the case of methane as the adsorbate are also listed and are derived from MNDO (Modified Neglect of Differential Overlap) calculations[2,4,17]. The (negative) charges on the zeolite oxygen atoms are assumed to be constant. No distinction is made between silicon and aluminum atoms in the lattice. These atoms are regarded as equivalent sites with the same charge. In order to ensure that the total charge on the zeolite is zero, the charge, q_T, on the sites occupied by either silicon or aluminum is dependent on the Al/Si ratio. For a zeolite with chemical composition $Na_xAl_xSi_{(y-x)}O_{2y}$, q_T is given by:

$$q_T = 2q_O - \left(\frac{x}{y}\right)q_{Na} - 1.4 - \left(\frac{x}{y}\right) \tag{II.6}$$

wherein q_O and q_{Na} denote the charges on oxygen and sodium, respectively. More attention to the choice of this charge distribution will be paid in a subsequent section of this chapter.

The Monte Carlo calculations are performed within the usual Metropolis algorithm[5]. A methane molecule is initially placed inside a micropore of the zeolite. One Monte Carlo step consists of two parts: first the centre of mass of the adsorbate is given a random displacement followed by an arbitrary rotation of the entire adsorbate. The resulting new configuration is either accepted as a valid one or rejected according to some criterion related to the energy difference between the former configuration and the new one. The appendix deals in more depth with the features of this algorithm.

In order to eliminate the effect of boundaries, periodic boundary conditions have been used with a period equal to the size of one zeolite unit cell. Furthermore, to save computer time, the potentials are truncated at a cut-off radius which is of the order of the size of one unit cell. The position and orientation of the adsorbate as well as the interaction energy are stored every 20th Monte Carlo step. In order to make an estimate of the statistical reliability, the simulations were divided into subruns of 10,000 Monte Carlo steps each. The standard deviation of the interaction energy was calculated from these subruns. One single run took from 10 up to 20 subruns.

Table II.2
Structural information on the zeolites considered

Zeolite	Pore diameter (A)	Lattice param. (A)	Unit cell comp. $Na_xAl_xSi_{(y-x)}O_{2y}$	Range of x
FAU	8	a=24.92 b=24.92 c=24.92	y=192	0-80
MOR	7	a=18.33 b=20.72 c= 7.60	y=48	0-16
MFI	5.5	a=20.07 b=19.92 c=13.42	y=96	0-20

Zeolite	Relative coordinates of extra-framework sites. The number between brackets indicate the multiplicity				Spacegroup	Ref.
FAU	Site	x	y	z	Fd3m no. 227	6
	I(32)	0.0656	0.0656	0.0656		
	II(32)	0.2310	0.2310	0.2310		
	III(16)	0.0000	0.0000	0.0000		
MOR	I(4)	0.0000	0.5000	0.0000	CmCm no. 63	7
	II(4)	0.0000	0.1825	0.7500		
	III(8)	0.0000	0.4517	0.8090		
MFI	I(4)	0.0000	0.0000	0.0000	Pnma no. 62	8
	II(4)	0.0000	0.0000	0.5000		
	III(4)	0.4725	0.2500	0.9012		
	IV(4)	0.3977	0.2500	0.8854		
	V(4)	0.3383	0.2500	0.8386		

For clarity, the notation for the extra-framework sites as given in this Table has been used. The official notation as proposed by Mortier et. al.[18] has not been followed.
The order of occupying the extra-framework sites with sodium ions is:
FAU: Site I/Site I+III/Site I+III+II
MOR: Site I/Site I+II/Site I+II+III
MFI: Site I/Site I+II/Site I+II+III/Site I+II+III+IV/Site I+II+III+IV+V

The various zeolite structures used are obtained from crystallographic data which are summarized in Table II.2. The zeolitic Al/Si ratio is varied by placing sodium ions at extra-framework positions and adjusting the charge on the silicon/aluminum sites according to equation (II.6). The extra-framework sites for the sodium ions are also listed in Table II.2. For low Al/Si ratios, it is assumed that only the sites labelled I are occupied. Upon a further increase of the Al/Si

ratio, sites II, III, etcetera are being occupied additionally. The lattice parameters a, b, and c are fixed at the values as presented in Table II.2. This implies that changes in the unit cell dimensions caused by variations in the aluminum content in the zeolite lattice are not taken into account. The validity of this assumption will be discussed in a subsequent section.

II.3 Results and Discussion

The heat of adsorption, Q_s, of methane adsorbed in the zeolites FAU, MOR and MFI at different temperatures and Al/Si ratios has been calculated. It is noted that the different zeolite structures considered do not only differ in topology, but may also differ in chemical composition. The Al/Si ratio in synthetic FAU materials may differ from about 0.20 up to 1 and for synthetic MOR samples, this ratio normally ranges from 0.05 to 0.25. Subsequent de-alumination of FAU and MOR makes it possible to obtain a ratio of almost 0.0 for both zeolites. MFI, on the other hand, is originally a siliceous zeolite with Al/Si ratios ranging from 0 to about 0.1. In order to be able to compare the adsorption characteristics of the different zeolites in a range of identical chemical compositions, adsorption in MOR and MFI with rather unrealistic compositions (high Al/Si ratios) is simulated.

Table II.3
Heats of adsorption (Q_s) of methane in various zeolites (kJ/mol)

Zeolite	Al/Si	T(K)	Experimental	Calculated	Ref.
FAU	0.33	300	15.2	14.1 +/- 0.4 13.8*	9
MOR	0.09	300	23.0	21.4 +/- 2.6	10
MFI	0.00	300	28.0	22.3 +/- 0.4	11

* Yashonath et. al.[2]

Effect of zeolite topology

For a comparison with literature adsorption data, Q_s for the three zeolites with realistic chemical composition has been calculated. Table II.3 displays Q_s for adsorption in FAU (Al/Si=0.33), MOR (Al/Si=0.09) and MFI (Al/Si=0.0) at T=300 K. Furthermore the experimental values for Q_s are also quoted in Table II.3 as well as the value calculated by *Yashonath et. al.*[2]. From Table II.3 it is seen that the computed Q_s is in very good agreement with the result of *Yashonath et. al.*

The agreement with experimental Q_s values is satisfactory. All experimental values agree with the computed values if the standard deviations in both the computational results and the experimental results are taken into account.

Effect of temperature and zeolite topology

Using the same zeolite chemical composition as in the preceding section, Q_s has been calculated as a function of temperature. The results are presented in Figure II.1. As the temperature increases, a decrease of Q_s is observed which levels off at high temperatures.

Figure II.1 demonstrates that for wide-pore zeolites (such as FAU and MOR), Q_s is more influenced by temperature variations than in the case of medium-pore zeolites represented by MFI. This temperature dependence can be explained in terms of mobility and average siting of methane inside the zeolite micropores.

At low temperatures (T<200 K), there is a strong siting effect of the adsorbate. The methane molecules are localized at specific low energy sites inside the zeolite. At higher temperatures, the mobility of the adsorbate molecules increases resulting in an average siting which is energetically less favourable. Owing to the smaller dimensions of the micropores of zeolite MFI compared to FAU and MOR, the decrease in interaction energy with increasing mobility is less in zeolites with medium-pore diameters.

Given the larger channel diameter of zeolite MOR compared to MFI, it is expected that Q_s in the case of adsorption in MOR is smaller than in the case of adsorption in MFI. As a matter of fact, this trend is observed in Figure II.1, but only for temperatures above 250 K. For lower temperatures, however, the opposite is observed which is due to the presence of low-energy adsorption sites for methane in the MOR framework. This feature will be discussed in more depth in a subsequent section.

Effect of zeolite chemical composition

The results of Monte Carlo simulations of the adsorption of methane in FAU, MOR and MFI as a function of Al/Si ratio are shown in Figures II.2 and II.3.

In the case of FAU, an increase of the Al/Si ratio from 0.0 to 0.7 and accordingly the increase in concentration of sodium ions hardly influences the adsorption of methane (cf. Figure II.2, lower curve). Since no literature on experimental data of methane adsorption in FAU as a function of Al/Si ratio exists, the computed data is compared with experimental data on ethane and ethene[13] which are also shown in Figure II.2. Q_s values reported ranged from 22 to 29 kJ/mol for ethane adsorption in FAU with Al/Si ratios varying between 0.01 and 1.0. On the other hand, Q_s for ethene adsorbed in Na-FAU showed a strong dependence on the Al/Si ratio. Within the same Al/Si range, Q_s varies from 20 to 42 kJ/mol. In both cases, Q_s increases with increasing Al/Si ratio.

From these results, it can be concluded that the presence of sodium ions has a large influence on a polarizable adsorbate such as ethene. However, the interaction of sodium ions on less polarizable adsorbates, such as ethane and also methane, is much smaller. Figure II.2 clearly shows the resemblance between the simulations and the experimental data; a very weak influence of the presence of sodium ions on the adsorption process is found for both adsorption of methane (computed) and ethane (measured). It is noted, however, that the simulations on methane adsorption show a small decrease of Q_s with increasing Al/Si ratio, whereas a small increase is measured in the case of ethane.

In the case of the zeolites MOR and MFI, the situation is drastically altered. Results of these simulations are presented in Figure II.3. For low Al/Si ratios, only a small (if any) influence

Figure II.1
Heat of adsorption as a function of temperature for methane adsorbed in the zeolites FAU, MOR and MFI. The standard deviations vary in the range 1 to 10%

of the presence of sodium ions is observed. This is in accordance with the results for adsorption in zeolite FAU. However, upon further increasing the sodium content (increasing Al/Si ratio) in both lattices a sharp decrease in Q_s is observed. This phenomenon can be understood with the aid of Figures II.4, II.5, II.6 and II.7.

Figure II.4 displays the average siting of methane inside the micro channels of MFI (Al/Si=0.09). From this figure, it is clearly seen that no specific siting occurs indicating that the methane molecules are free to move through the straight and sinusoidal channels. By increasing the Al/Si ratio to 0.14, the straight channels are effectively blocked by sodium ions as is demonstrated in Figure II.5. In this case, the adsorbate is forced to stay at a particular site and is not able to 'migrate' to an adsorption site which provides a more favourable interaction.

In the case of MOR, a similar situation is observed. For an Al/Si ratio of 0.09, the straight channels and the 'side-pockets' situated at the edges of the main channels are free for adsorption. It is found that especially siting in the side-pockets results in an energetically favourable situation (Figure II.6). These low-energy sites are not present in the MFI framework and this explains the larger Q_s for MOR at low (T<250 K, cf. Figure II.1) temperatures. Increasing the Al/Si ratio actually results in an effective blocking of the entrances to the side-pockets by sodium ions as is illustrated in Figure II.7. In this situation, the energetically favourable sites are blocked and the methane molecules are forced to the (wide-pore) channels where interaction with the zeolitic

Figure II.2
Heat of adsorption as a function of Al/Si ratio for methane, ethane and ethene adsorbed in zeolite FAU.
Standard deviations for the calculated methane curve are in the order of 1%. T=300 K.

internal surface is much less.

It should be noted that the sharp decrease of Q_s with increasing Al/Si ratio in the case of MOR and MFI is partially caused by an artificial manner of placing sodium ions in the zeolite lattices. In the range of low Al/Si ratios, sodium ions are put on extra-framework sites (see Table II.2) which cannot be reached by the adsorbed methane molecules. Upon a further increase of the Al/Si ratio (corresponding with an increasing sodium content), sodium ions are necessarily put on extra-framework sites which are easily accessible for methane. This manner of placing sodium ions is of course very unrealistic and thus the adsorption characteristics as given in Figure II.3 for MOR and MFI will not be observed in such an extreme way.

The influence of the presence of exchangeable cations on adsorption processes has been extensively studied by *Vansant*[14] and *Breck et. al.*[15]. It was generally found that varying the amount and nature (size and charge) of the exchangeable cations had an enormous influence on the selectivity towards adsorption of different adsorbates. In fact, Figure II.4, II.5, II.6 and II.7 indicate the reason of this observed selectivity.

Sensitivity of the model parameters

A glance at the atomic charges on the carbon atom and hydrogen atoms in the methane molecule (cf. Table II.1) reveals a peculiarity. The charge on the carbon atom is taken to be +0.07
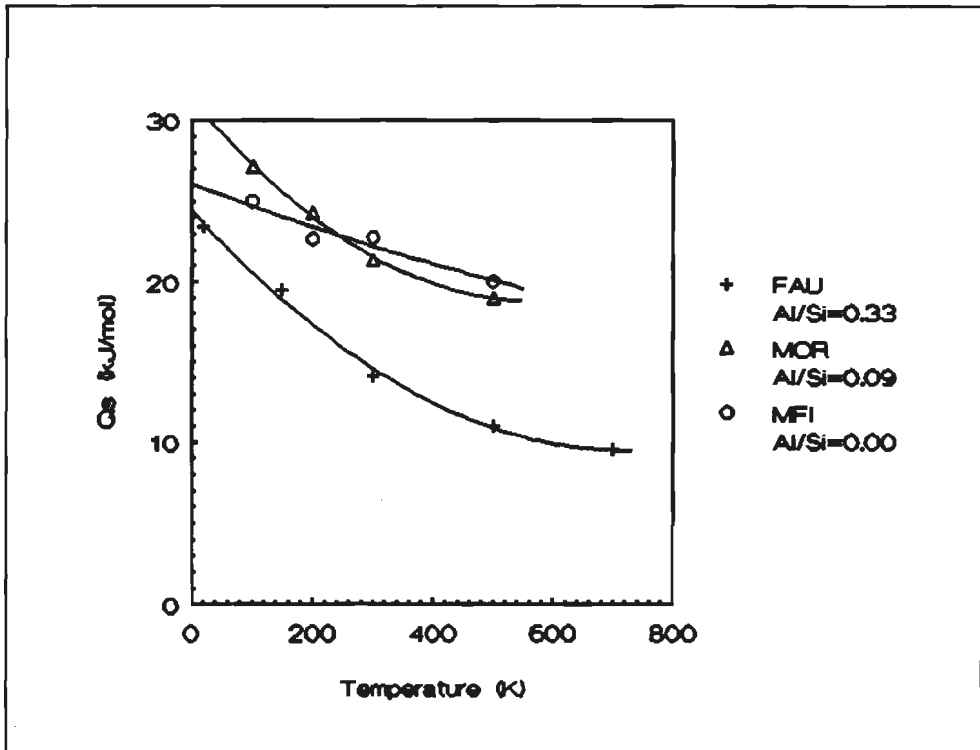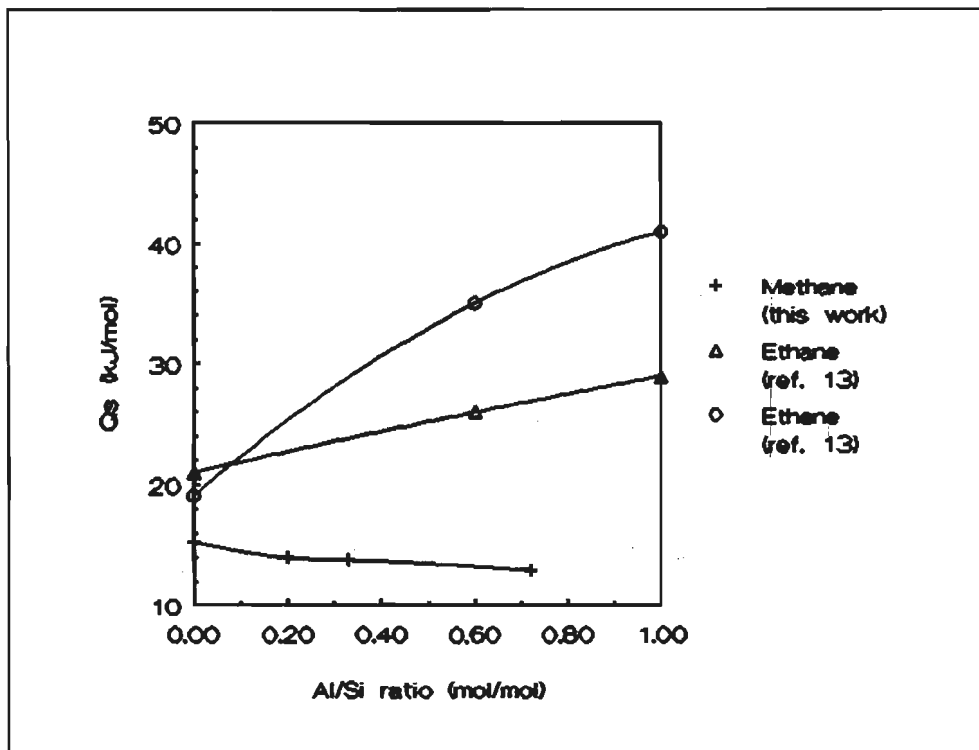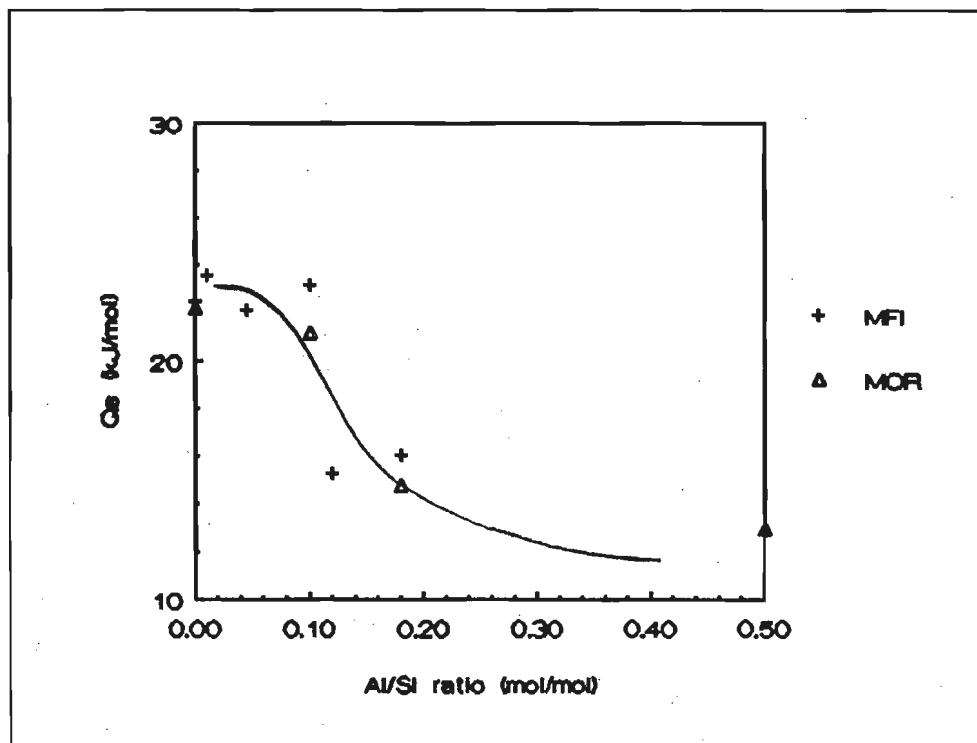
Figure II.3
Heat of adsorption as function of Al/Si ratio for methane adsorbed in the zeolites MOR and MFI. Standard deviations for the calculated curves vary in the range of 1 to 10%. T=300 K.

e whereas the charge on the hydrogen atoms is -0.0175 e. Since carbon is more electronegative, this charge distribution is physically rather unrealistic. One would expect a negative charge on the carbon atom and a positive charge on the hydrogen atoms.

Using the *GAMESS*[12] program, the atomic charges on the methane molecule have been checked. A multipole expansion[16] gave exactly the same atomic charges as given in Table II.1. However, a *Mulliken* population analysis gave the opposite result: a charge of -0.8 e on the carbon atom and the charge on the hydrogen atoms being 0.2 e was calculated[17]. Using these *Mulliken* charges resulted in adsorption energies which were completely overruled by coulombic interactions.

It is concluded that the electrostatic contribution in equation (II.2) is somewhat obscure. However, the magnitude of the electrostatic contribution is only 3% of the total interaction energy. So the effect of the methane atomic charges as used in this chapter is quite small. Since the electrostatic contribution is small and since the physical background is obscure, on can just as well leave this contribution out. Especially for adsorbates with a low polarizability and siliceous zeolites, a description of the adsorbate-zeolite interaction in terms of a *Lennard-Jones* interaction only suffices. Furthermore, the physical background of the A and B parameters in the *Lennard-Jones* potential has been thoroughly discussed before[3] and is therefore preferred. Also in Figure II.2, a very small electrostatic effect in experimental heats of adsorption was observed. It may be argued that this effect is more properly described by adsorbate polarization due to the presence of the
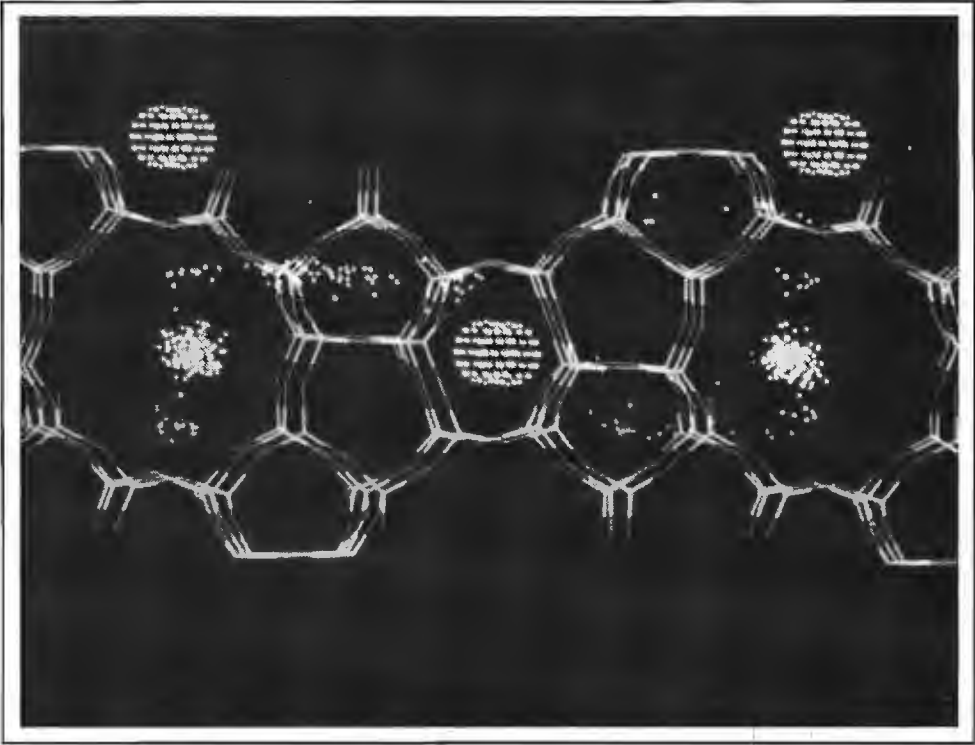
Figure II.4
Distribution of methane adsorbed in MFI at 300 K. Al/Si=0.09. Each spot represents the projection of the centre of mass of the methane molecule. Sodium ions are represented by dotted spheres.

sodium cations rather than by Coulomb interactions. This point is worthwhile to study in the future.

In the computational model, the variable charge, stemming from the variation in the Al/Si ratio, has been distributed over the silicon and aluminum sites in the zeolite framework while keeping the charge on the oxygen atoms constant (-0.7 e; cf. Table II.1). This choice is somewhat arbitrary. In order to investigate the effect of this manner of zeolite charge distribution, the heats of adsorption with the variable framework charge smeared out over the zeolite oxygen atoms have also been calculated. The charge on the zeolite oxygen atoms as a function of Al/Si ratio is in this case given by:

$$q_O - \left(\frac{x}{2y}\right)q_{Na} + \left(\frac{x}{2y}\right)q_{Si,Al} - \left(\frac{x}{2y}\right) + 0.7 \tag{II.7}$$

wherein the charge on the silicon and aluminum atoms is taken to be the constant value of 1.4. One calculation for FAU (Al/Si=0.7; T=300 K) has been performed for the zeolite charge distribution according to equation (II.7). Q_a was calculated to be -14.6 Kj/mol whereas with the charge distribution according to equation (II.6), Q_a turned out to be -13.0 kJ/mol. Taking into account the statistical standard deviations, it is concluded that the two calculated values nearly coincide.
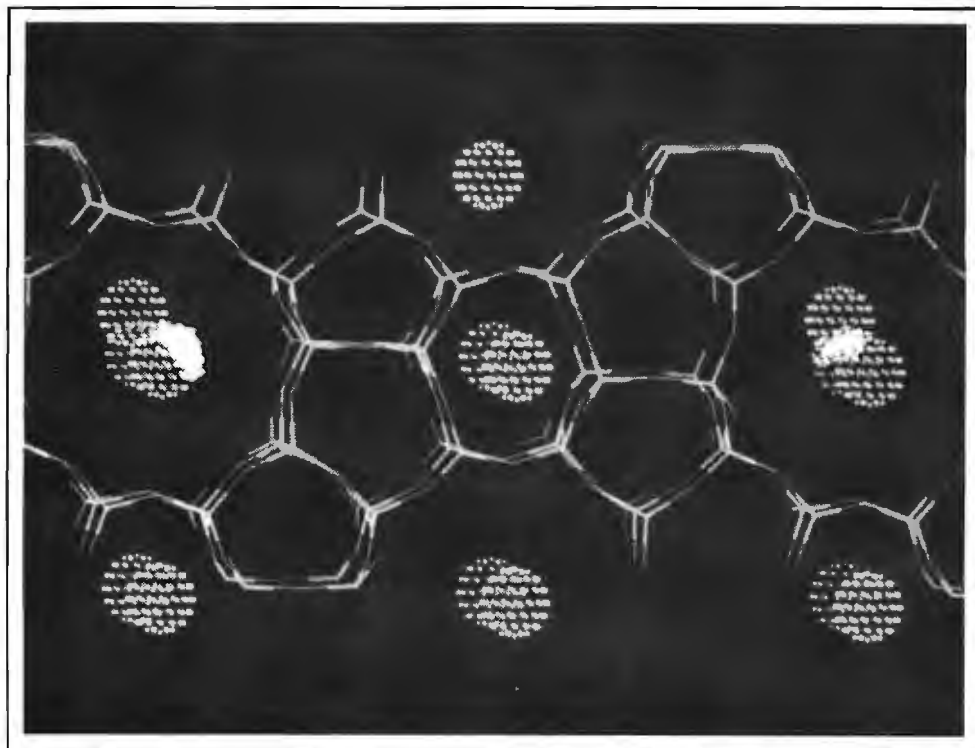
<u>Figure II.5</u>
Distribution of methane adsorbed in MFI at 300 K. Al/Si=0.12.

As has already been mentioned in a foregoing section, the lattice parameters a, b and c were kept fixed in all simulations. The values used for these parameters are quoted in Table II.2. As a check, Q_a has been calculated for methane adsorption in zeolite MOR (Al/Si=0.09; T=300 K) with two lattice parameter sets: a=18.64, b=21.07, c=7.73 and a=17.93, b=20.23, c=7.44. These two sets yielded adsorption energies of -23.7 +/- 2.9 kJ/mol and -19.3 +/- 2.9 kJ/mol, respectively. Obviously, neglecting unit cell contractions for the computation of adsorption energies does not seem to lead to a serious error.

II.4 Conclusions

In this chapter, it has been shown that Monte Carlo simulations can be advantageously used for studying the adsorption of methane in zeolites. Given the fact that the experimental heats of adsorption are nearly reproduced (cf. Table II.3), a practical justification is put forward that the potential parameters used by *Yashonath et. al.*[2] and in this chapter are generally applicable for methane adsorption in various zeolites. However, this does not mean that the potentials used, especially the electrostatic part, are reliable or have a well defined physical significance. More research in this area is required in order to arrive at reliable parameters to describe the adsorbate-zeolite interactions.
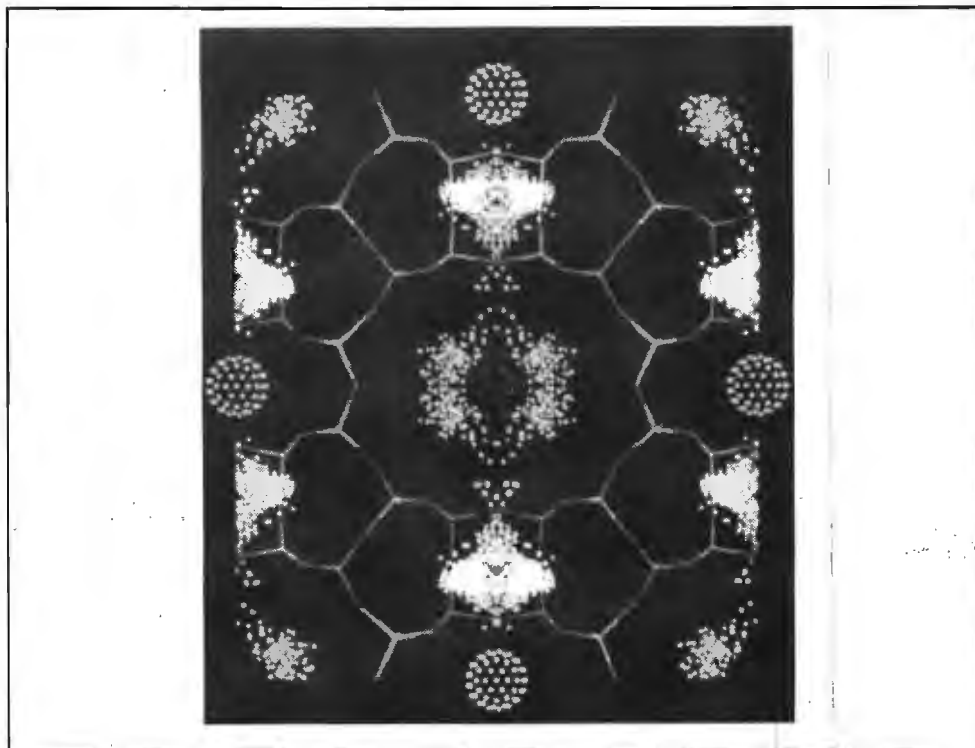
Figure II.6
Distribution of methane adsorbed in MOR at 300 K. Al/Si=0.09.

It is shown that the heat of adsorption increases with decreasing temperature (cf. Figure II.1). This feature especially shows up in the case of wide-pore zeolites (FAU) which can be explained in terms of higher adsorbate mobilities at elevated temperatures in these zeolite structures resulting in shorter adsorbate-zeolite contact times. It is noted, however, that no reference in the literature describing this phenomenon was found.

Computer graphics proved to be a good tool in visualizing the siting effects of adsorbates in zeolites and offer a fast and convenient way to display adsorption characteristics. The difference in the heats of adsorption of methane in MOR and MFI as a function of temperature could be explained by the presence of low energy adsorption sites in the MOR framework.

Finally, the results discussed in this chapter strongly advocate a combination of computer graphics and computer simulations in order to obtain more insight into several physical processes at a molecular level. These simulation techniques may also find potential applications in other related research areas such as diffusion in zeolites (cf. Chapter III) and shape selective catalysis using zeolitic catalysts. In this context, it is worth mentioning that pore blocking, caused by the presence of exchangeable cations, in zeolite Offretite directly influences the catalytic performance[19]. The phenomenon of pore blocking and its impact on the siting behaviour of adsorbates is clearly demonstrated in this chapter.
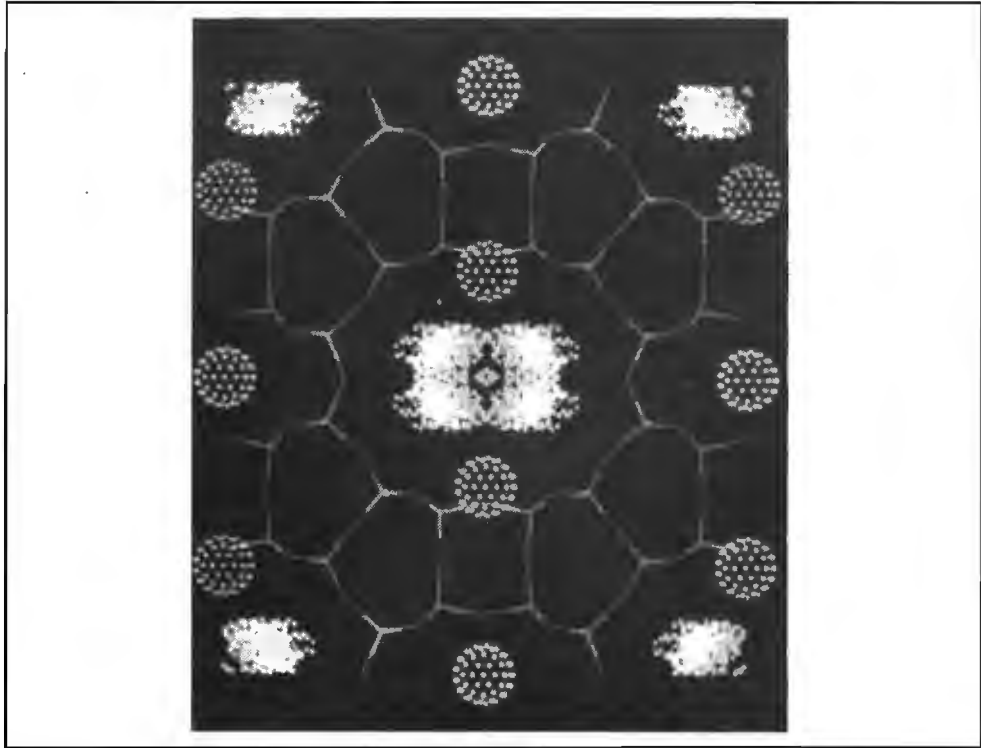
Figure II.7
Distribution of methane adsorbed in MOR at 300 K. Al/Si=0.2.

Appendix: Principles of the Monte Carlo Method

In this appendix, a review of the Monte Carlo method as proposed by *Metropolis et. al.*[5] is presented.

Principles

Consider a system consisting of N particles in a fixed volume V and at a constant temperature T. From statistical mechanics it can be derived that the thermodynamic average of a quantity A can be written as[20]:

$$<A> = \frac{1}{Z}\int A(\Gamma)e^{\left(\frac{-E(\Gamma)}{kT}\right)}d\Gamma \qquad (A.1)$$

wherein:

Γ : the configuration of all particles (the integration is over all possible configurations)
$E(\Gamma)$: (potential) energy of the configuration Γ

A(Γ): value of property A for configuration Γ

Z : the partition function given as:

$$Z = \int e^{\left(\frac{-E(\Gamma)}{kT}\right)} d\Gamma \tag{A.2}$$

The purpose of the Monte Carlo method is to calculate the integral as given in equation (A.1) numerically. A rather naive method of integration involves generating a set of randomly chosen configurations Γ_i (i=1,...,M). The average of property A can then subsequently approximated by:

$$\langle A \rangle = \frac{\sum_{i=1}^{M} A(\Gamma_i) e^{\left(\frac{-E(\Gamma_i)}{kT}\right)}}{\sum_{i=1}^{M} e^{\left(\frac{-E(\Gamma_i)}{kT}\right)}} \tag{A.3}$$

The statics of this integration method, however, will be very poor because most values of Γ_i will be chosen in a region where the exponential exp(-E(Γ_i)/k.T) is very small[20].

To circumvent this problem, *Metropolis et. al.*[5] proposed the method of importance sampling. In this method, the configurations are not chosen randomly but are selected with a probability P(Γ_i). In this case, the average of property A can be written as[5,21]:

$$\langle A \rangle = \frac{\sum_{i=1}^{M} \left(\frac{A(\Gamma_i)}{P(\Gamma_i)}\right) e^{\left(\frac{-E(\Gamma_i)}{kT}\right)}}{\sum_{i=1}^{M} \frac{e^{\left(\frac{-E(\Gamma_i)}{kT}\right)}}{P(\Gamma_i)}} \tag{A.4}$$

Choosing the equilibrium distribution $P^{eq}(\Gamma_i)$:

$$P^{eq}(\Gamma_i) = e^{\left(\frac{-E(\Gamma_i)}{kT}\right)} \tag{A.5}$$

for the distribution of configurations in the chain, then the average value of property A is easily calculated by:

$$<A> = \sum_{i=1}^{M} A(\Gamma_i) \tag{A.6}$$

Algorithm

Generating a chain a chain of configurations $(\Gamma_1,...,\Gamma_M)$ with a specific distribution can formally be described with the theory of *Markov* processes[21]. It can be proven that a chain generated by the following algorithm leads to the equilibrium distribution as represented by equation (A.4). The algorithm resembles the algorithm as used in this chapter:

```
A = 0.0
DO 1 for configuration i=1,...,M
    choose a random particle (molecule)
    give this particle a random new position and orientation:
    Γ = old configuration
    Γ'= new configuration
    δE = E(Γ') - E(Γ)
    IF (δE<0) THEN
      accept Γ'
      A = A + A(Γ')
    ELSE
      choose a random number 0≤ε≤1
      IF  ε < exp(-δE/k.T)  THEN
        accept Γ'
        A = A + A(Γ')
      ELSE
        reject Γ' and use Γ as the new configuration
      ENDIF
    ENDIF
1 CONTINUE
  A = A/M
```

A very important condition is that in the course of the simulation a representative part of the configuration space is sampled. Obviously this condition puts constrains on the run length of the simulation. Short simulations will yield large standard deviations in the average property values. Standard deviations are calculated by using subruns from which one run is built up.

References

1a. R.M. Csicsery, Pure & Appl. Chem., 1986, 58(6), p. 841.
1b. I.E. Maxwell, Catal. Today, 1987, 1(4), p. 385.
2. S. Yashonath, J.M. Thomas, A.K. Nowak, A.K. Cheetham, Nature, 1988, 331, p. 601.
3. A.V. Kiselev, A.A. Lopatkin, A.A. Schulga, Zeolites, 1985, 5, p. 261.
4. A.K. Cheetham, Private communications.
5. N. Metropolis, A.W. Rosenbluth, M.N. Rosenbluth, A.H. Teller, J. Chem. Phys., 1953, 21, p. 1081.
6. T. Hseu, 1972, PhD thesis University of Washington, University microfilms no. 73-13835, Ann Arbor.
7. W.M. Meier, Z. Kristallogr., 1961, 115, p. 439.
8. C. Baerlocher, Proc. 6th Int. Zeolite Conf., 1983.
9. A.K. Nowak, A.K. Cheetham, Proc. 7th Int. Zeolite Conf., 1986, p. 475.
10. R.M. Barrer in "Zeolites: Science and Technology", NATO ASI series, 1984, 80, p. 227, Martinus Nijhof Pub., The Hague.
11. H. Papp, W. Hinsen, N.T. Do, M. Baerns, Thermochimica Acta 1984, 82, p. 137.
12. GAMESS: General Atomic And Molecular Electronic Structure System. M.F. Guest, University of Manchester, Regional Computer Center Daresburry Laboratory..
13. H. Stach, U. Lohse, H. Thamm, W. Schirmer, Zeolites, 1986, 6, p. 74.
14. E.F. Vansant, Proc. Int. Symp. "Innovation in Zeolite Materials Science", 1987, p. 143.
15. D.W. Breck, W.G. Eversole, R.M. Milton, T.B. Reed, T.L. Thomas, J. Am. Chem. Soc., 1956, 78, p. 5963.
16. J.D. Jackson, "Classical Electrodynamics", 1975, p. 137, 2nd ed., John Wiley & Sons.
17. B.W. van Beest, Private communications.
18. W.J. Mortier, J. Phys. Chem., 1972, 76, p. 650.
19. C. Mirodatos, D. Barthomeuf, J. of Catal., 1985, 93, p. 246.
20. K. Binder, "Introduction: Theory and Technical Aspects of Monte Carlo Simulations" in "Monte Carlo Methods", 1981, Springer Verlag.
21. N.G. van Kampen, "Stochastic Processes in Physics and Chemistry", 1980, North Holland, Amsterdam.

<div align="center">

CHAPTER III

**MOLECULAR DYNAMICS SIMULATIONS OF ADSORBED SPECIES
IN ZEOLITES**

</div>

III.1 Introduction

As already discussed in chapter II, the interaction between organic adsorbates and a zeolitic environment plays an important role in the extended field of zeolite science and technology. Directly related to those interactions are adsorption and diffusion phenomena which are known to have a large impact on the catalytic activity and selectivity of zeolites.

In reactions catalyzed by porous solids, such as zeolites, catalytic selectivity is not only a matter of stoichiometry but also steric constraints for molecular transport in the zeolite void space can be the reason for the so called shape selectivity[1]. Shape selectivity can in principle be obtained by adjusting the size[2] and accessibilities[3] of the micropores. A distinction is made between three types of shape selectivity depending on whether the pore size limits the entrance of the reacting molecule (reactant selectivity), the desorption of the product molecule by diffusive transport (product selectivity) or the formation of certain transition states along the reaction coordinate (restricted transition state selectivity).

Evidently, the phenomenon of shape selectivity is directly related to adsorption and diffusion characteristics. Since it is difficult to obtain information on these characteristics at a molecular level by direct measurements, especially at elevated temperatures at which chemical conversions take place, computer simulations might offer alternative approaches to problems encountered in zeolite catalysis research.

Whereas chapter II dealt with a study on adsorption in zeolites, this chapter is devoted to the dynamics of adsorbed species in zeolites. The adsorbates under consideration will vary from simple mono-atomic (xenon) or adsorbates which can be approximated as mono-atomic (methane), up to rather complex molecules such as ethane and propane (complex in terms of Molecular Dynamics procedures). Special attention will be paid to the influence of temperature, adsorbate concentration and zeolite morphology on the diffusion characteristics. In this context, all zeolite structures under consideration (MFI, MOR and EU-1) are assumed to be all-silica and hence no electrostatic adsorbate-zeolite interactions are considered. Furthermore, this set of zeolite structures represents a wide variety of possible channel systems allowing a systematic study of differences in pore diameters and tortuosities.

Whenever possible, simulated diffusion characteristics will be compared with recent experimental data obtained from PFG-NMR spectroscopy.

III.2   Zeolite Structures, Adsorbates and Computational Details

Zeolite MFI[3] has a three-dimensional channel system with sinusoidal channels comprised of 10 membered rings running along the crystallographic a-direction and straight channels comprised of 10 membered rings along the crystallographic b-direction. Both channels have a pore diameter of approximately 5.5 A. The two channel systems are interconnected via the intersections which are cage-like with a diameter of 7 A. MOR[4] and zeolite EU-1[5] are both characterized by an one-dimensional channel system with side po^Xxets which can be entered from the main straight channels. However, whereas MOR has main channels comprised of 12 membered rings (7 Å in diameter) and side pockets with entrances comprised of 8 membered rings (4.5 Å in diameter), EU-1 has main channels comprised of 10 membered rings (5.5 Å in diameter) and side pockets with entrances formed by 12 membered rings (7 Å in diameter). This particular choice of zeolite structures covers a range of possible networks which allows the study on the influence of topology on the diffusion process.

All zeolites are in the all-silica form (Al/Si=0). Bearing this in mind, it is reasonable to assume that the zeolites excert no electrical field on the adsorbed species. Furthermore, due to the large size of the oxygen compared to silicon atoms in the zeolitic SiO_4 tetrahedra, it is assumed that silicon is effectively screened by oxygen. Hence, any short range interaction between an ad$xrbate and silicon is neglicible. All interaction energies are calculated using *Lennard-Jones* potentials in the atom-atom approximation following the approach of *Kiselev et. al.*[7,8,9,10]. This approach has already been discussed in chapter II.

In the mono-atomic case, the adsorbates under consideration are xenon and methane. For methane, the entire molecule is regarded as one atom with an effective radius and polarizability[6] which is to be used in the *Kirkwood* relation (Chapter II). Furthermore, diffusion of xenon and methane is simulated in MFI and MOR only. Interaction parameters A and B for the mono-atomic case are given in Table III.1. The cut-off radius for the *Lennard-Jones* potential is in the order of the size of one zeolite unit cell. Boundary effects have been taken into account by applying periodic boundary conditions.

Table III.1
Lennard-Jones potential parameters for mono-atomic adsorbates

Atom pair	$A.10^{-3}$ $(kJ.Å^6.mol^{-1})$	$B.10^{-7}$ $(kJ.Å^{12}.mol^{-1})$
Xe...O	8.6143	1.1051
Xe...Xe	33.621	15.139
CH4...O	5.9106	0.6190
CH4...CH4	9.9912	0.9503

The simplest adsorbate considered in the poly-atomic case is again methane. Diffusion of methane is simulated in MFI, MOR and EU-1. As a follow up on this methane study, ethane and propane diffusivities were examined in silicalite only. The experimental data available on methane, ethane and propane diffusivities in silicalite, will be used to check the computational results. In the

poly-atomic case, no adsorbate concentration effect were studied. In order to eliminate concentration effects when studying structural features and to ensure a constant loading per unit volume, the loading of the various zeolites were scaled according to the zeolite framework densities. As a reference, MFI was given a loading of 2.0 adsorbate molecules per $Si_{24}O_{48}$ unit. The framework density[11] of MFI is 17.9 T-sites/1000 A^3, so for MOR, having a framework density of 17.2, the loading is 2.0*(17.2/17.9)=1.9 adsorbate molecules per $Si_{24}O_{48}$ unit and for EU-1 (density 18.2) the loading is 2.0 adsorbate molecules per $Si_{24}O_{48}$ unit. The interaction between the adsorbates and the zeolite lattice and the adsorbates with each other is described by a *Lennard-Jones* atom-atom pair potential having the same form and containing the

Table III.2
Lennard-Jones potential parameters for poly-atomic adsorbates

Atom pair	A.10^{-3} (kJ.Å^6.mol^{-1})	B.10^{-7} (kJ.Å^{12}.mol^{-1})
C...C	2.87439	0.31284584
C...H	0.73389	0.03584790
H...H	0.19138	0.00370723
C...O	1.70067	0.14449978
H...O	0.53674	0.01499785

same assumptions as for the mono-atomic case. Potential parameters are given in Table III.2. The adsorbate molecules as well as the zeolite lattice are assumed to be rigid. So all internal degrees of freedom of the adsorbates are constrained with a tolerance of $\sigma \leq 10^{-4}$ Å^2. The poly-atomic simulations were carried out in a zeolite unit consisting of 192 T-sites. Thus the total number of adsorbates considered in the ensemble is 16 for MFI and EU-1 and 15 for MOR. Boundary effect were taken into account by applying periodic boundary conditions. The cut-off radius for the *Lennard-Jones* potential is in the order of 15 Å.

Details of the Molecular Dynamics methodology are given in the appendix at the end of this chapter. All simulations were performed within the NVT algorithm. Typical equilibration times were in the order of a few ps (1 ps=10^{-12} s) while sampling took place over a few up to several hundred ps. Diffusion coefficients are calculated by plotting the mean square displacement (MSD) of all adsorbates against the time. The slope of this line determines the diffusion coefficient D according to equation (A.18).

III.3 Results and Discussion I; Mono-atomic Adsorbates

In this section, results of Molecular Dynamics simulations for both xenon and methane in MFI and MOR will be presented. Properties under investigation are:
· the determination of self-diffusion coefficients as a function of temperature (only for xenon) and zeolite loading
· the anisotropy of diffusion

· adsorbate trajectories (methane only).

At the end of this section, a comparison with experimental data on adsorption and diffusion of xenon and methane in MFI will be made. Experimental diffusivity data of the adsorbates under consideration in MOR are not available.

All calculations in this section are carried out in a simulation box consisting of 2*2*2=8 unit cells. The cut-off radius for the interaction potentials was 12.3 A. The adsorbate molecules were initially placed at random positions inside the channels of the zeolite micropores. The equilibration period was typically of the order of 100 ps and data was collected over of few tens up to several hundred ps. Using a time step of 0.01 ps, this results in a total number of Molecular Dynamics sampling points of ≈50,000. All simulations were performed in the NVT ensemble.

III.3.1 Xenon in MFI

Effect of temperature

These calculations were performed with a xenon concentration, Θ_{Xe}, of 1 atom per $Si_{24}O_{48}$ unit. Since the unit cell of MFI is comprised of 96 T-sites, the total number of adsorbates

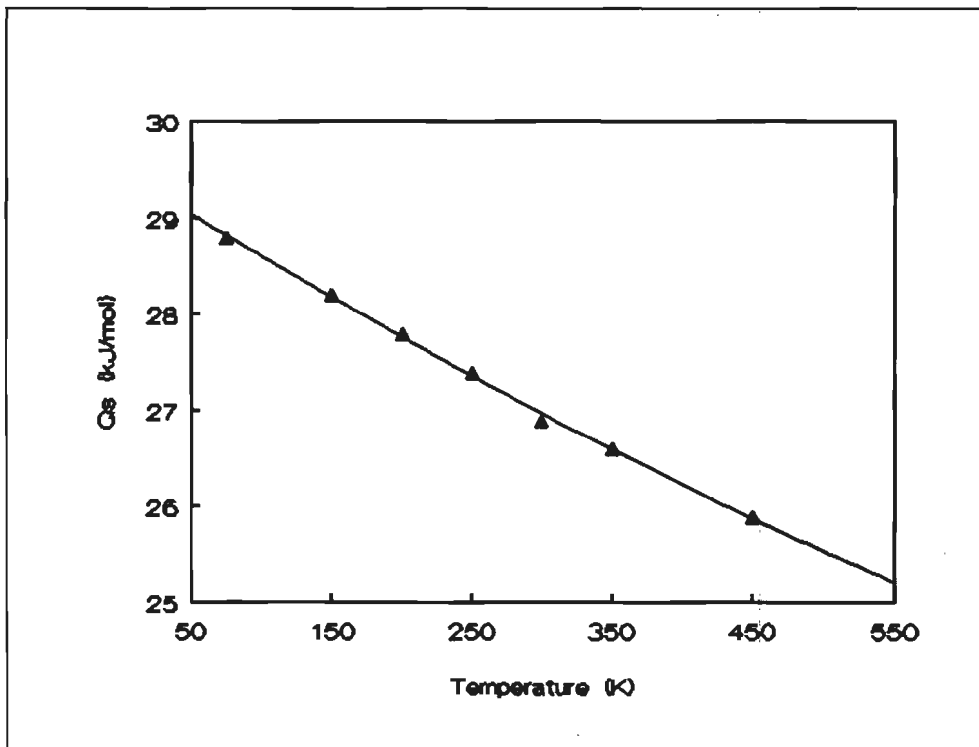

Figure III.1
Xenon in MFI; adsorption enthalpy versus temperature (Θ_{Xe}=1).

under consideration in the simulation equals 32. The temperature ranges from 77 K up to 450 K. As expected, a decrease in the internal energy of adsorption and an increase in diffusivity is
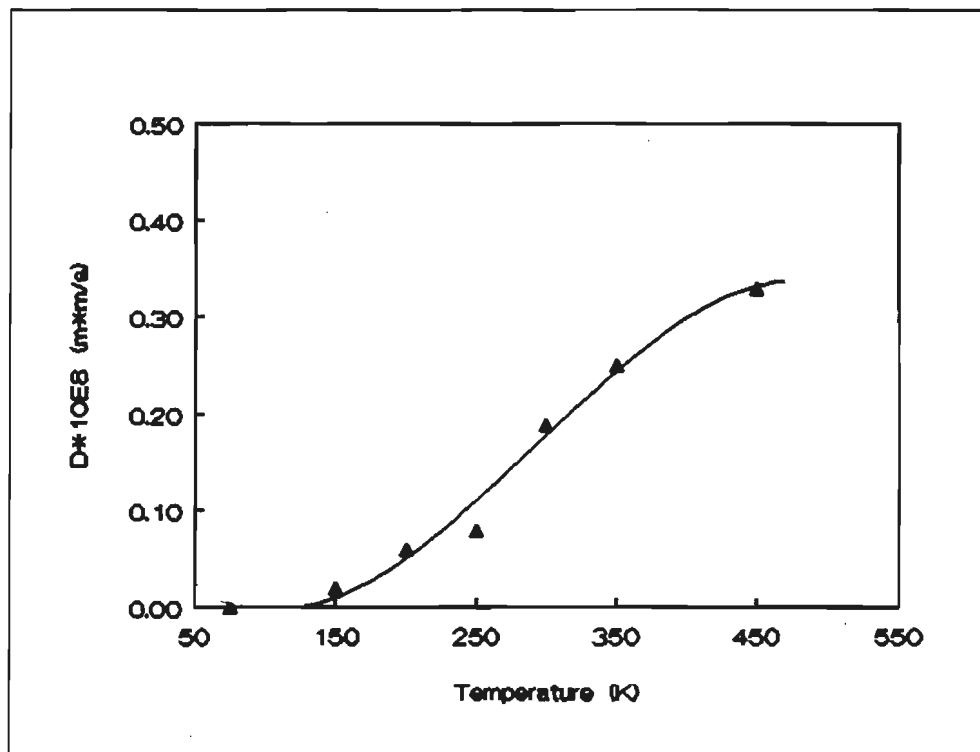
Figure III.2
Xenon in MFI; diffusion coefficient versus temperature ($\Theta_{xc}=1$). The relative errors in the diffusion coefficients are approximately 15 %.

observed with increasing temperature. The reason for this effect is that at high temperature particles have a higher kinetic energy, and thus greater velocities, and can therefore probe sites of higher (less favorable) potential energy. Calculated v^Xxues are given in Figure III.1 and III.2.

From Figure III.1, the adsorption enthalpy for xenon in MFI at room temperature is estimated to be 27 kJ/mol. As shown in Figure III.2, the diffusion coefficient at room temperature is of the order of $0.23.10^{-8}$ m^2/s.

The variation in diffusion coefficients suggests that atoms are hardly moving at temperatures below 110 K. This is confirmed by figures III.3a and III.3b showing the average xenon mean square displacement (MSD) as a function of time at 91 K and 298 K. Allthough the MSD varies at both temperatures, the variation at 91 K is a fluctuation around a near constant value given by the fitted line. This suggests that xenon atoms remain in the vicinity of their starting postions (which are not neccesarily at the origin).

A plot of ln(D) versus 1/T is shown in Figure III.4. The computed activation energy of self diffusion is 5.8 kJ/mol and $D_0=1.9.10^{-8}$ m^2/s. Those values are very low compared to the activation energy of 15 kJ/mol obtained for xenon in MFI from rate uptake measurements[12].

Effect of xenon concentration

Calculations were performed at 298 K with a number of different xenon concentrations
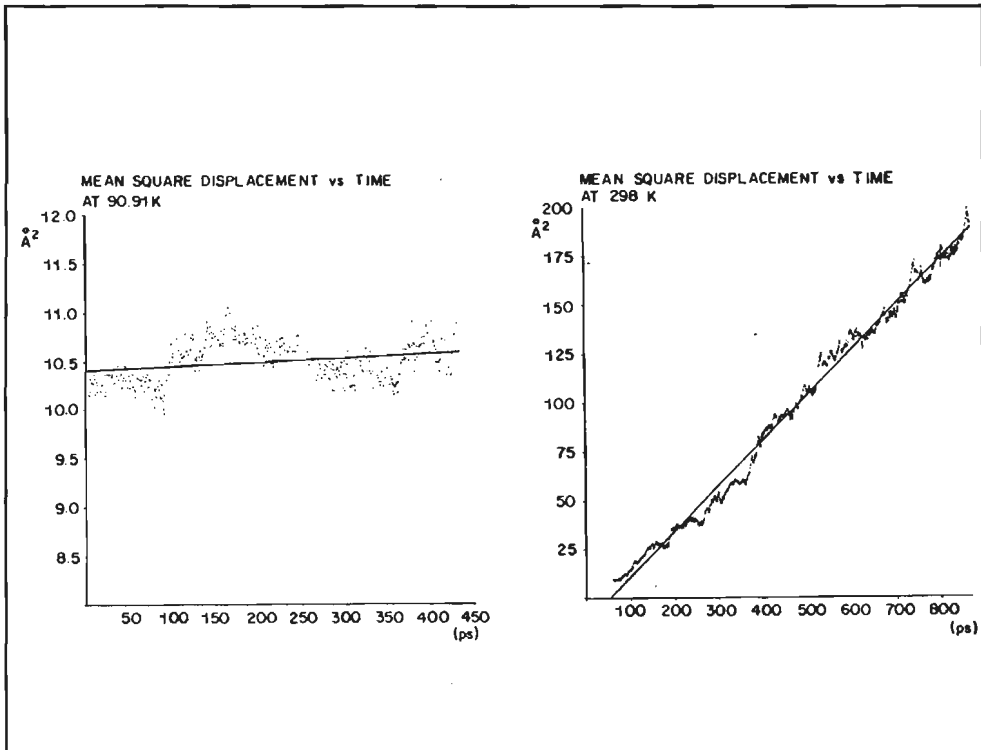
Figure III.3
Xenon in MFI; mean square displacement versus time at T=91 K (a) and T=298 K (b) ($\Theta_{Xe}=1$).

ranging from 1 to 128 xenon atoms in the simulation volume ($\Theta=1/32$ up to $\Theta=4$). This corresponds with a maximum of 16 xenon atoms per MFI unit cell. Figure III.5 shows the computed variation of the adsorption enthalpy with concentration. The internal energy of adsorption is expected to increase with xenon concentration because of additional interatomic interactions between the adsorbates among each other. A limit must be reached when xenon atoms can not be further accomodated in the zeolite micropores anymore, resulting in a sharp drop in the energy of adsorption (not shown in Figure III.5). Figure III.5 suggests that a loading of 16 xenon atoms per MFI unit cell ($\Theta=4$) is possible and it is assumed that this value is very close to the maximum packing.

Figure III.6 shows the variation of the diffusion coefficient, D, as a function of the number of adsorbates per unit cell. The diffusion coefficient at higher loadings decreases as more xenon-xenon collisions occur and thus more obstacles are encountered by a moving xenon atom.

Anisotropy of diffusion

Overall and separate diffusion coefficients for the x-, y- and z-direction are calculated using the *Einstein* relation (see appendix). This is of particular interest in zeolite systems because of the channels, which in the case of MFI coincide with the x- (sinusoidal) and y-direction (straight channels). Figures III.7a through III.7c show the calculated mean square displacement (MSD) in
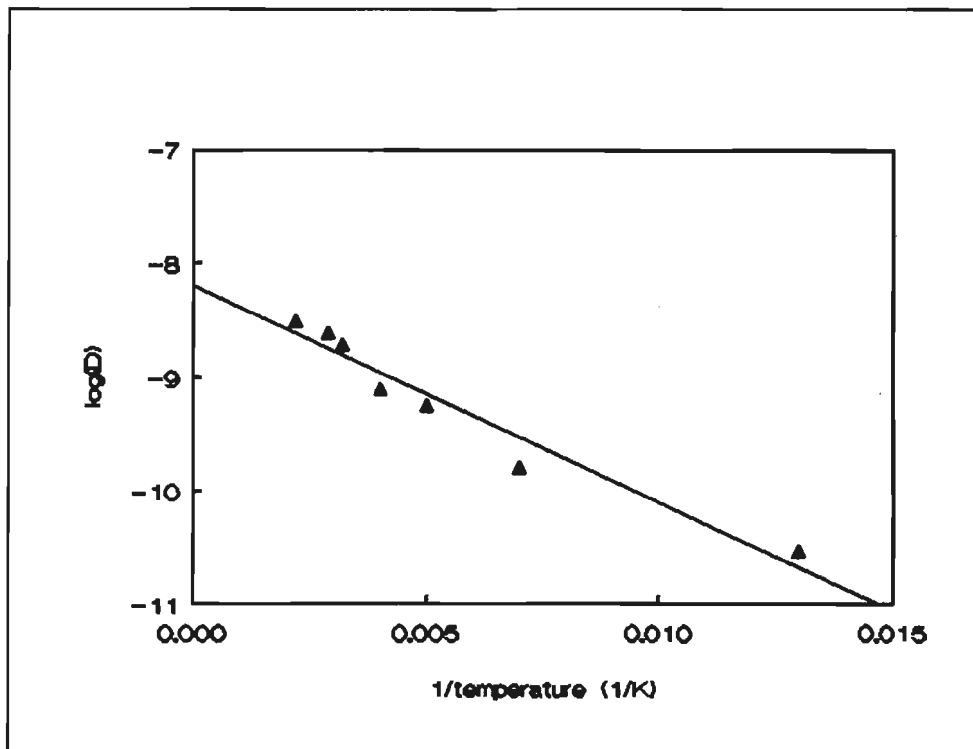
Figure III.4

Xenon in MFI; Arrhenius plot of ln(D) versus 1/T ($\Theta_{Xe}=1$). The relative errors in the diffusion coefficients are approximately 15%.

Table III.3

Anisotropy in the diffusion coefficient and overall diffusivities for the systems under study (D in 10^8 m^2/s).

	D_x	D_y	D_z	D
Section 1; xenon in MFI. T=298 K, Θ=1.	0.31	0.55	0.13	0.33±0.15
Section 2; methane in MFI. T=298 K, Θ=1.	2.04	3.50	0.30	1.80±0.20
Section 3; methane in MOR. T=298 K, Θ=1.	0.00	0.01	4.06	1.40±0.60

the separate directions as a function of simulation time at 298 K for a zeolite loading of 4 xenon atoms per MFI unit cell (Θ=1). The calculated diffusion coefficients D_x, D_y, D_z, and D together with the estimated computational errors are listed in Table III.3 (section 1). The diffusion coefficients for the three different directions suggest that diffusion is fastest along the straight channel (y-direction) and slower along the sinusoidal channels (x-direction). Diffusion along the z-direction requires the alternating motion of adsorbates between straight and sinusoidal channels. The non-neglicible diffusion coefficient D_z shows that this motion does occur, but the small value

suggests that only occasional transitions of adsorbates from one channel system to the other is observed.

III.3.2 Methane in MFI

Effect of methane concentration

The Molecular Dynamics calculations are performed at T=298 K with five different methane concentrations in MFI. The number of adsorbate molecules occluded ranges from 1 up to 8 per MFI unit cell ($\Theta=1/4$ up to $\Theta=2$).

Just as in the case of xenon, the diffusivity of methane decreases monotonically with an increasing zeolite loading as can be seen in Figure III.8. Furthermore, as shown in Figure III.9, also the dependence of the adsorption enthalpy on the zeolite loading is quite similar as in the case of xenon adsorbed in MFI; a slight increase of the adsorption enthalpy is observed with increasing loading due to additional intermolecular interactions. At the point were the maximum loading is approached, a decrease in heat of adsorption is observed due to adsorbate-adsorbate repulsions.

Anisotropy of diffusion and adsorbate trajectories

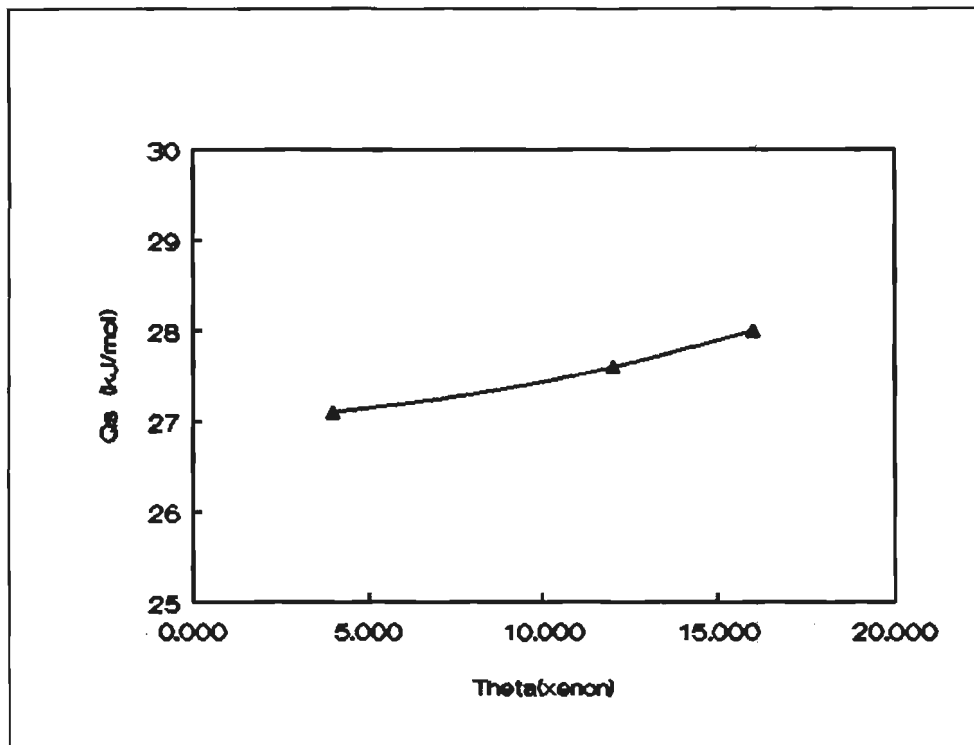The mean square displacements of the methane molecules migrating in MFI versus the

Figure III.6

Xenon in MFI; diffusion coefficient versus zeolite loading (T=298 K). The loading in this figure is defined as the number of xenon atoms per $Si_{96}O_{192}$ unit.

time are displayed in Figure III.10. The simulation temperature for this case is T=298 K whereas the zeolite loading is 4 methane molecules per MFI unit cell (Θ=1).

Diffusion coefficients for the three distinct directions x, y, and z (corresponding with the crystallographic a-, b-, and c-axis, respectively) and the overall diffusion coefficient together with the computational errors are determined from these plots and are represented in Table III.3, section 2.

As can be seen from Table III.3, the same distinction between diffusion in the x- and y-direction as observed in the xenon-MFI system also shows up here; diffusion in the x-direction (along the sinusoidal channels) is somewhat slower than diffusion along the y-direction (along the straight channels). Diffusion along the z-direction, thus hopping from one channel system to the other, is found to be approximately one order of magnitude slower, indicating that this phenomenon also in the case of methane in MFI only occasionally occurs.

Figure III.7

Xenon in MFI; anisotropy of diffusion. Mean square displacement versus time in the x- (a), y- (b) and z-direction (c) at T=298 K and Θ=1.
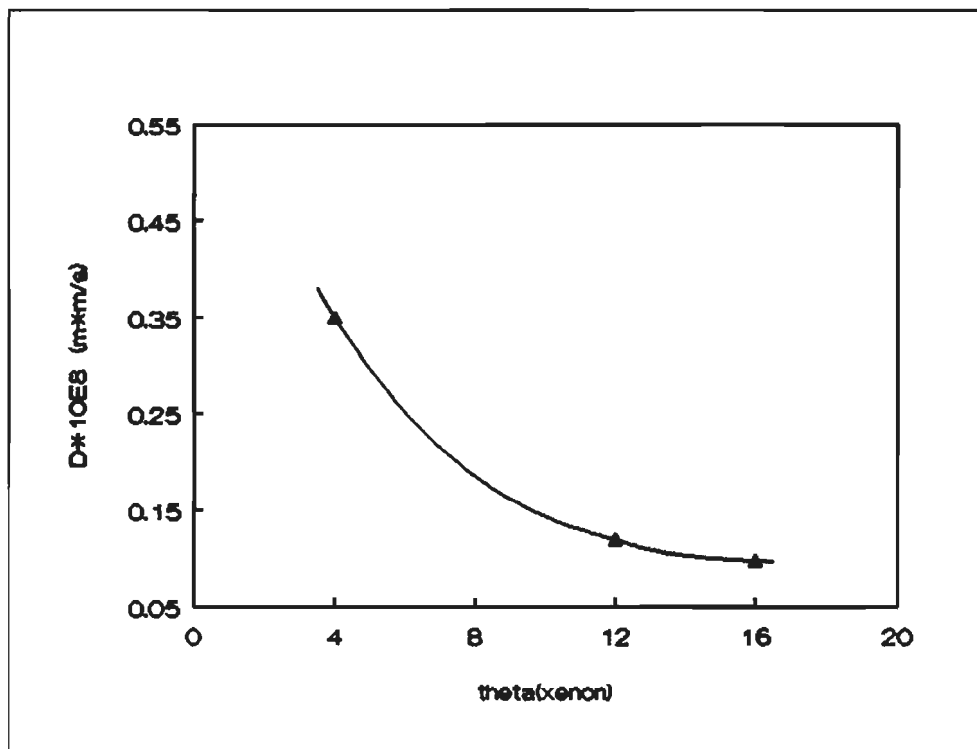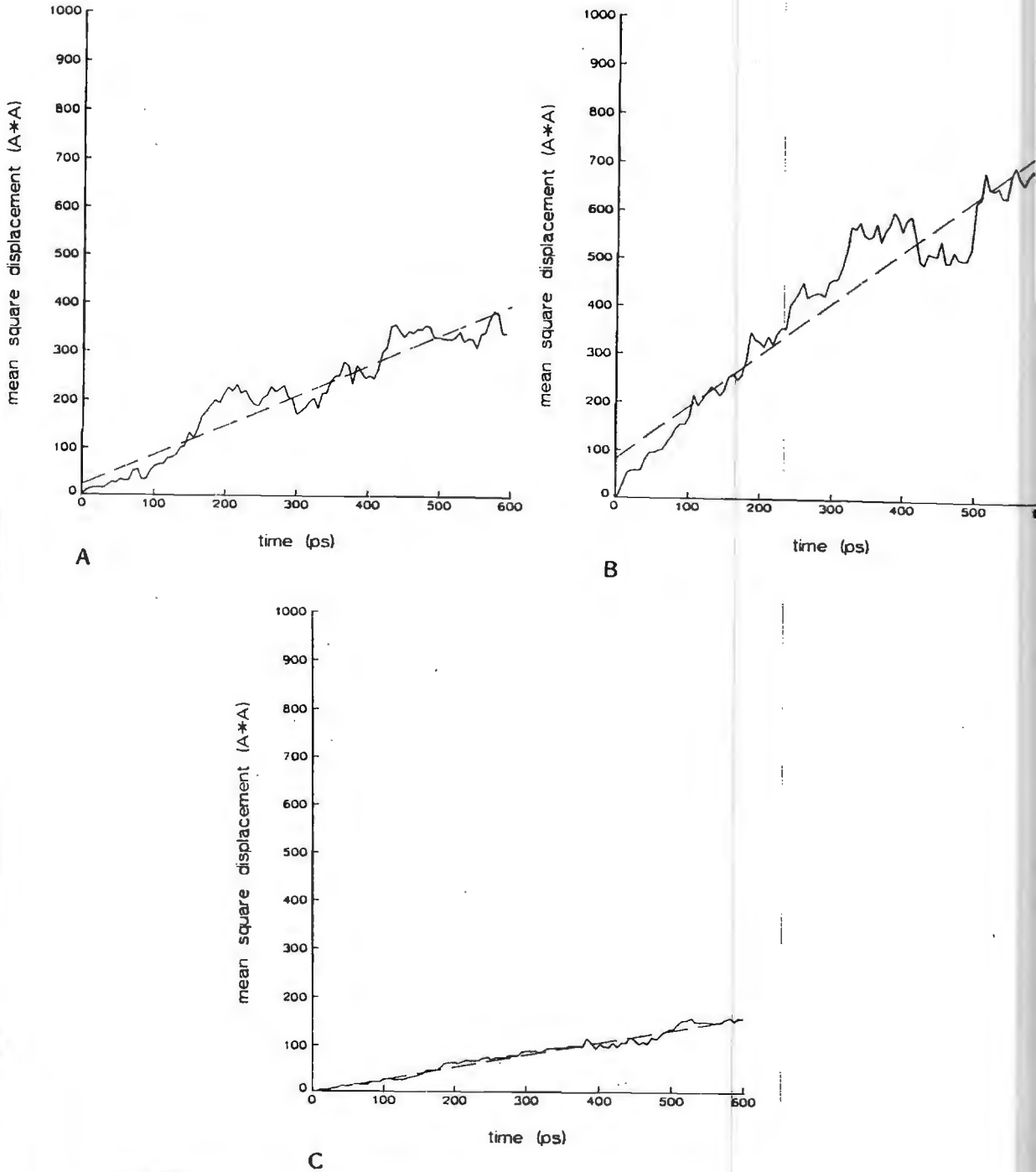
Figure III.8
Methane in MFI; diffusion coefficient versus zeolite loading (T=298 K). The loading in this figure is defined as the number of methane molecules per $Si_{96}O_{192}$ unit.

The difference in diffusivity of methane migrating along the straight and sinusoidal channels is graphically visualized in Figure III.11. This figure shows the trajectory over 100 ps of one selected methane molecule (out of 32) migrating in MFI. It goes without saying that the displayed adsorbate molecule is exhibited to the force fields caused by both the zeolite and the other adsorbate molecules which are not displayed. From the figure, it can be deduced that this particular methane molecule has a longer residence time in the sinusoidal channels (high density of dots) compared to the residence time in the straight channels (low density of dots). Obviously, this long residence time reduces the diffusivity along the y-direction as can be seen from Table III.3, section 2.

Figure III.9
Methane in MFI; adsorption enthalpy versus zeolite loading (T=298 K). The loading in this figure is defined as the number of methane molecules per $Si_{96}O_{192}$ unit.

Finally a point worth addressing is the remarkable difference between the diffusion coefficients of methane and xenon in MFI. The diffusion coefficient of methane is approximately a factor 5 larger than the one for xenon. This point will be discussed in more detail in a subsequent section of this chapter.

Figure III.10

Methane in MFI; anisotropy of diffusion. Mean square displacement versus time in the x- (a), y- (b) and z-direction (c) at T=298 K and Θ=1.
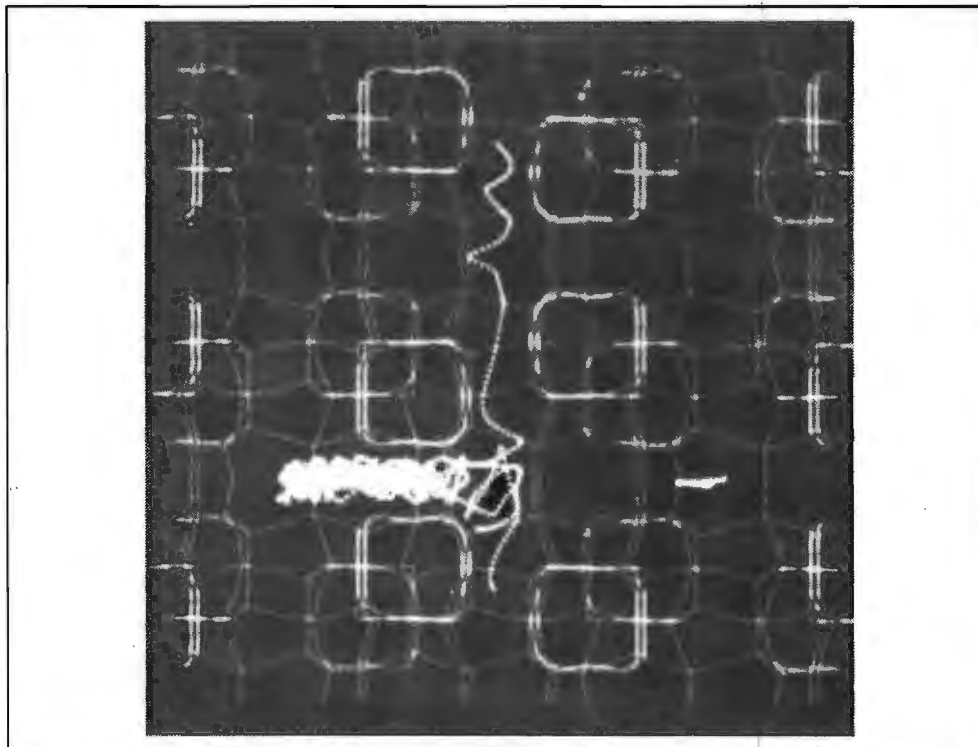
Figure III.11
Methane in MFI; trajectory of a selected methane molecule in MFI. The dots represent positions of the methane molecule at subsequent time intervals. T=298 K, Θ=1, time period=100 ps.

III.3.3 Methane in MOR

Effect of methane concentration

Concentration effects on the diffusivity and the adsorption enthalpy of methane in MOR are simulated at T=298 K. The zeolite loading, Θ, varied from 1 up to 6 methane molecules per MOR unit cell, $Si_{48}O_{96}$ (Θ=1/2 up to Θ=3).

Figure III.12 displays the dependency of the diffusion coefficient of methane in MOR on the zeolite loading. Interestingly, this figure shows some quite different features as Figure III.8 for the case of methane in MFI. In Figure III.12, at first instance an
increase in diffusivity with increasing zeolite loading up to 2-3 adsorbate molecules per MOR unit cell (Θ=1-1.5) is observed. This increase in diffusivity levels off when the zeolite loading is further increased and finally a decline of the difusivity is observed when the loading is increased from 3 up to 6 methane molecules per unit cell (Θ=1.5-3).

This phenomenon also shows up in Figure III.13, displaying the adsorption enthalpy of methane in MOR versus the zeolite loading. An initial decrease of the adsorption enthalpy with increasing loading is observed. Further increasing the zeolite loading results in a minimum of the
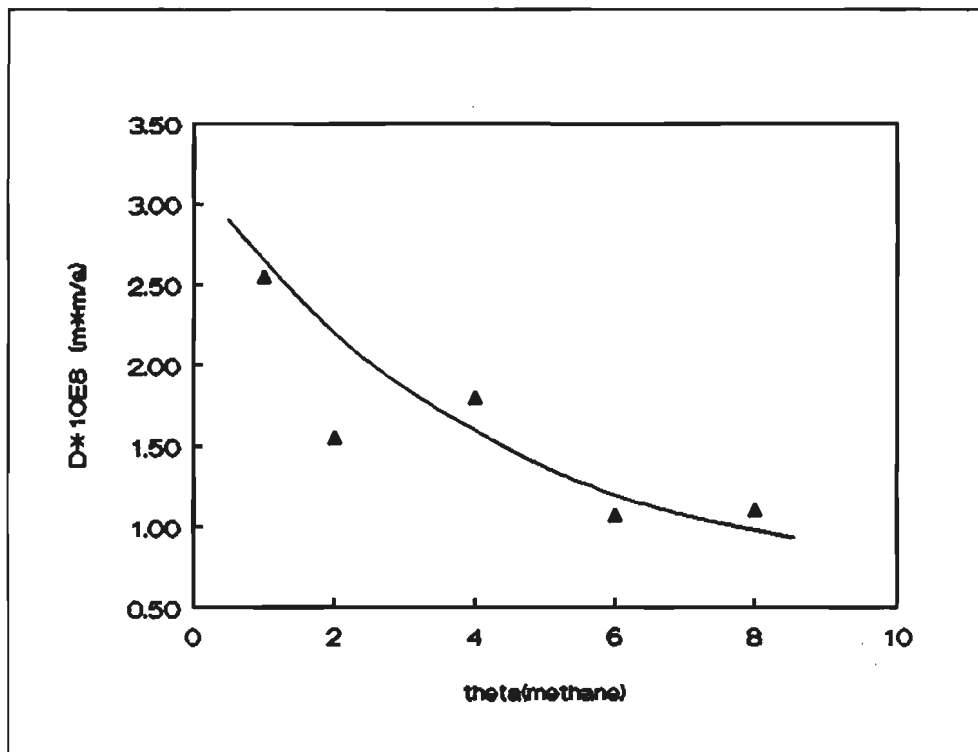
Figure III.12

Methane in MOR; diffusion coefficient versus zeolite loading (T=298 K). The loading in this figure is defined as the number of methane molecules per $Si_{48}O_{96}$ unit.

adsorption enthalpy after which a gradual increase in the adsorption enthalpy follows.

This peculiar behavior of methane in MOR has already been discussed in chapter II. The explanation is based on the finding that the side-pockets in the MOR structure obviously are strong adsorption sites for methane molecules. For low loadings, almost all adsorbate molecules are located in these side-pockets, resulting in a low mobility and a high adsorption enthalpy. When the loading is increased, the side-pockeHx are gradually filled and the remaining methane molecules are forced to migrate in the large 12-ring main channel. This results in an enhancement of the diffusivity and a decrease in adsorption enthalpy as visualized in figures III.12 and III.13, respectively. Further increasing the loading results in a decrease in diffusivity due to the occurrence of more adsorbate-adsorbate collisions and the adsorption enthalpy increases becuase more intermolecular interactions are involved.

Anisotropy of diffusion and adsorbate trajectories

The mean square displacement of the methane molecules migrating in MOR versus the time are plotted in Figure III.14. For these simulations, the same loading of methane molecules as in the case of MFI has been used in order to come to a proper comparison, thus $\Theta=1$ is considered. The simulation temperature is 298 K. Migration along the x- and y-axis is hardly observed whereas a normal diffusion along the z-axis (main channel) is observed. Since diffusion along the x- and
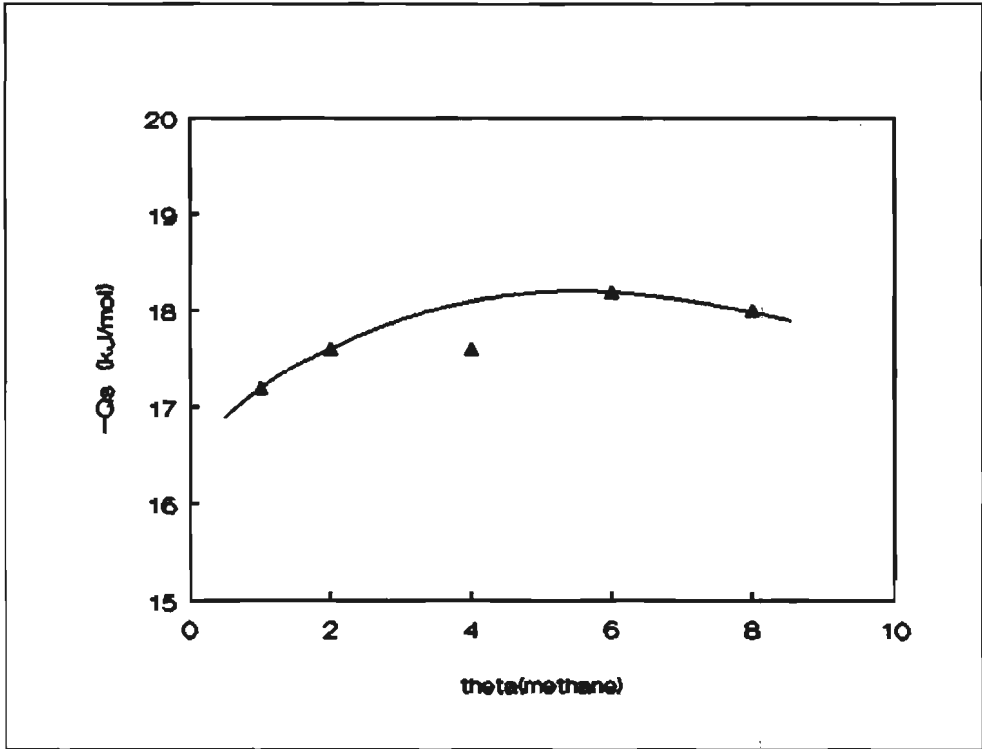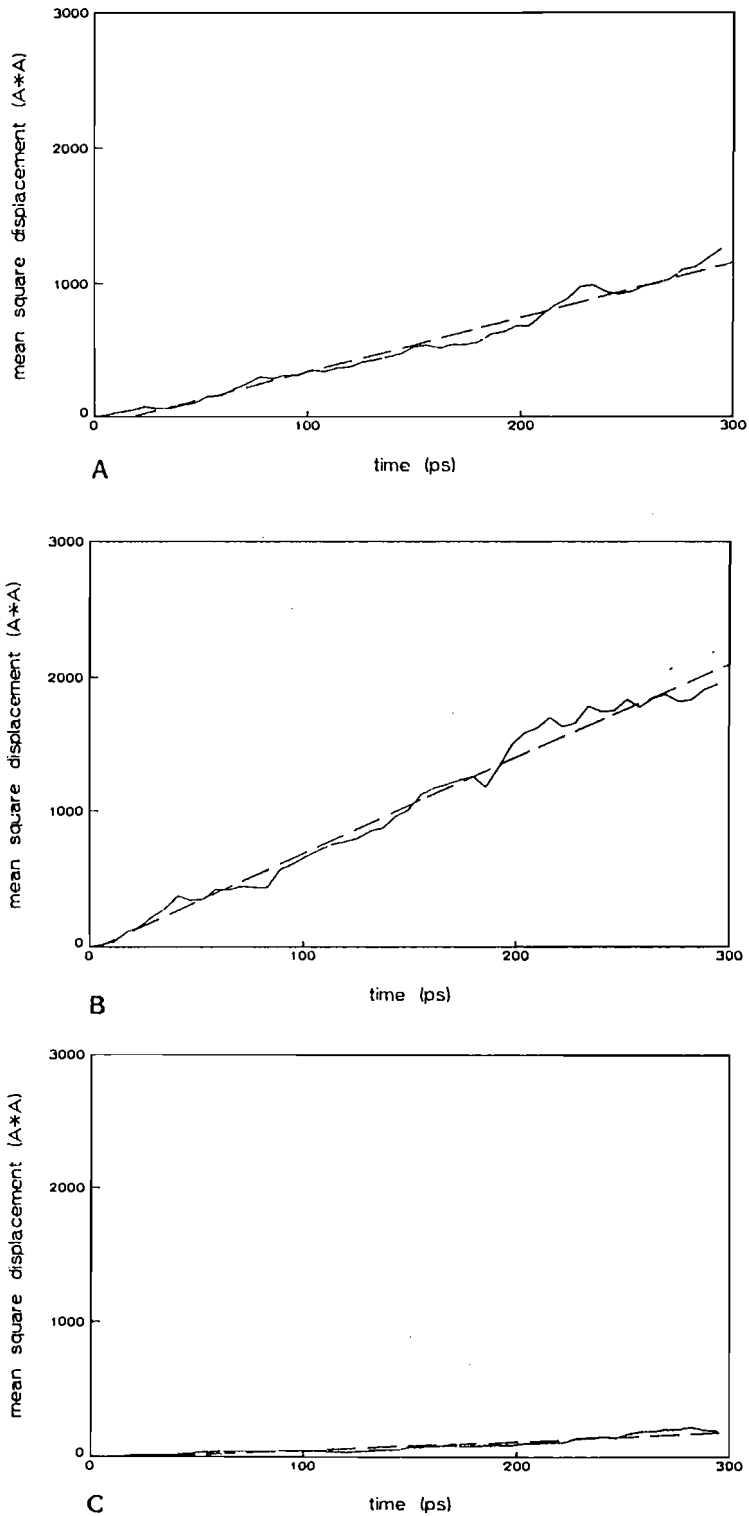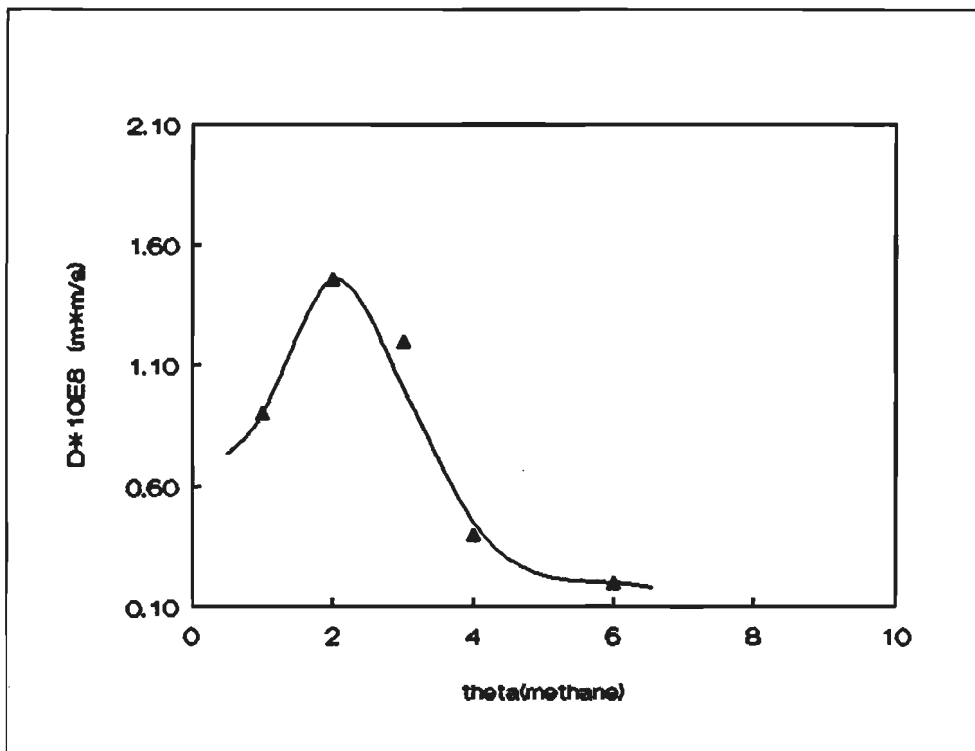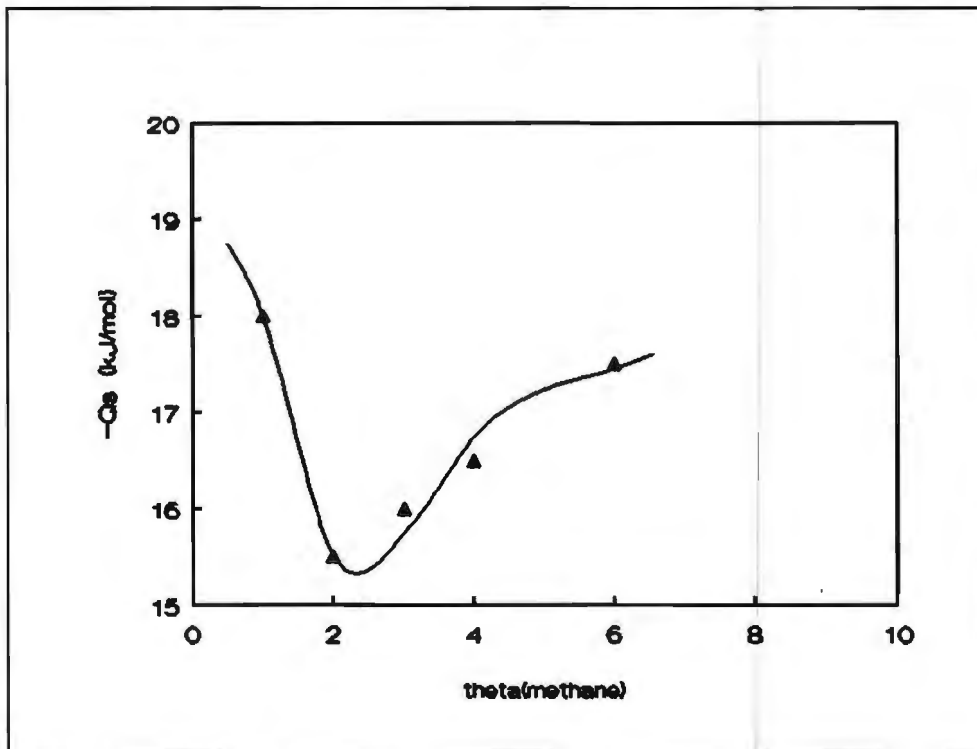
Figure III.13
Methane in MOR; adsorption enthalpy versus zeolite loading (T=298 K). The loading in this figure is defined as the number of methane molecules per $Si_{48}O_{96}$ unit.

y-axis is neglicible, only the mean square displacements along the z-direction are displayed in Figure III.14. The diffusion coefficient for the three separate directions and the overallHxiffusion coefficient together with the computational errors are given in Table III.3, section 3.

From Table III.3 it can be deduced that in line with expectations the anisotropy of the difusion for methane in MOR is quite severe. The diffusivities along the separate directions differ by at least two orders of magnitude. It is evident that, when the simulation time is increased, the diffusivity in the y-direction vanishes.

Figure III.15 displays the trajectory over 100 ps of one selected methane molecule (out of 16) migrating in MOR. The adsorbate is exposed to the force field caused by the zeolite and the presence of the other adsorbates which are not displayed. The high density of dots in the side-pocket indicate a long residence time for methane at these sites. A closer examination of Figure III.15 shows that this particular methane molecule under consideration is located in both the 12-ring main channel and the side-pocket. However, it also shows up that the methane molecule has tried to enter three other side-pockets. Apparently, these side-pockets were already occupied by other adsorbate molecules and hence penetration could not occur.
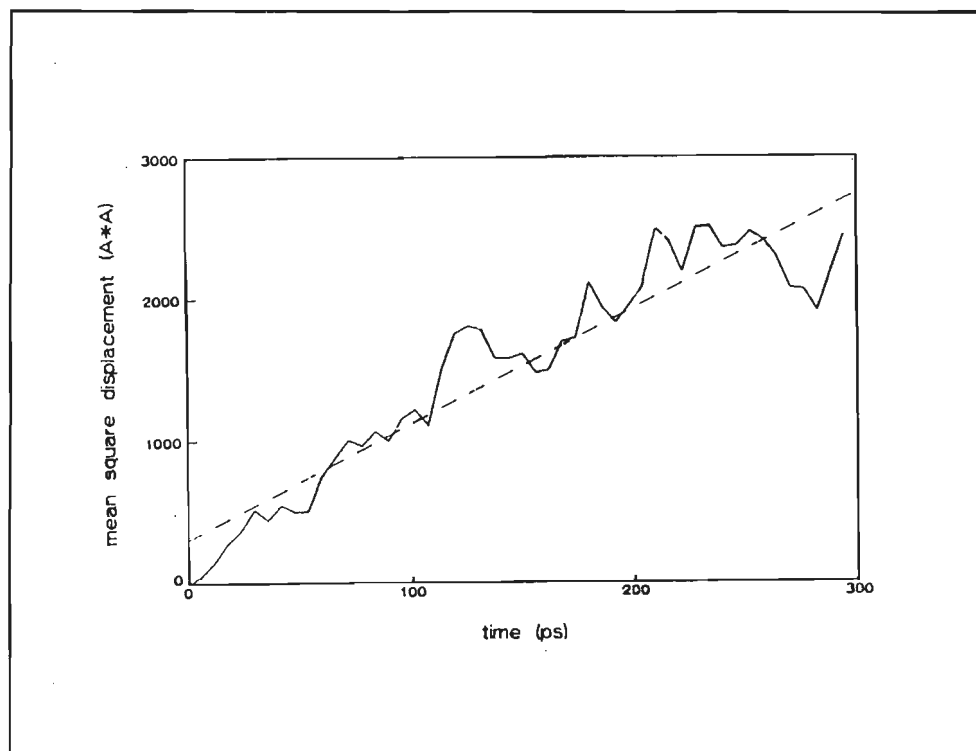
Figure III.14
Methane in MOR; anisotropy of diffusion. Mean square displacement versus time in the z-direction at T=298 K (Θ=1).

III.3.4 Discussion and comparison with experimental data

No dynamic experimental data for methane and xenon migrating in MOR seems to be available. This implies that the results presented for this system can be regarded as a theoretical prediction of the diffusion characteristics of methane and xenon in MOR. MHx is, however, a very interesting structure to study with PFG-NMR. As was anticipated, a very strong anisotropy of the diffusion along the three separate directions is observed in the calculations owing to the single dimensionality of the porous channel system in zeolite MOR. Anisotropy in diffusion is thought to be measurable by PFG-NMR techniques if the diffusivities in the different directions differ by one order of magnitude or more[13]. The computational results in this chapter indicate a difference of at least two orders of magnitude for methane in MOR, so in principle this should be detectable with PFG-NMR. The anisotropy for the case of methane in MFI is much less pronounced and is not observed acording to the literature[14].

Caro et. al.[14] have measured the diffusion coefficient of methane in MFI as a function of zeolite loading by means of the PFG-NMR technique. Their results, together with the computational results of this chapter are represented in Figure III.16. The agreement between the Molecular Dynamics calculations and experimental values is excellent. Computed and experimental values essentially lie on the same curve.

The adsorption enthalpy of methane in MFI was computed to be ≈18 kJ/mol. An
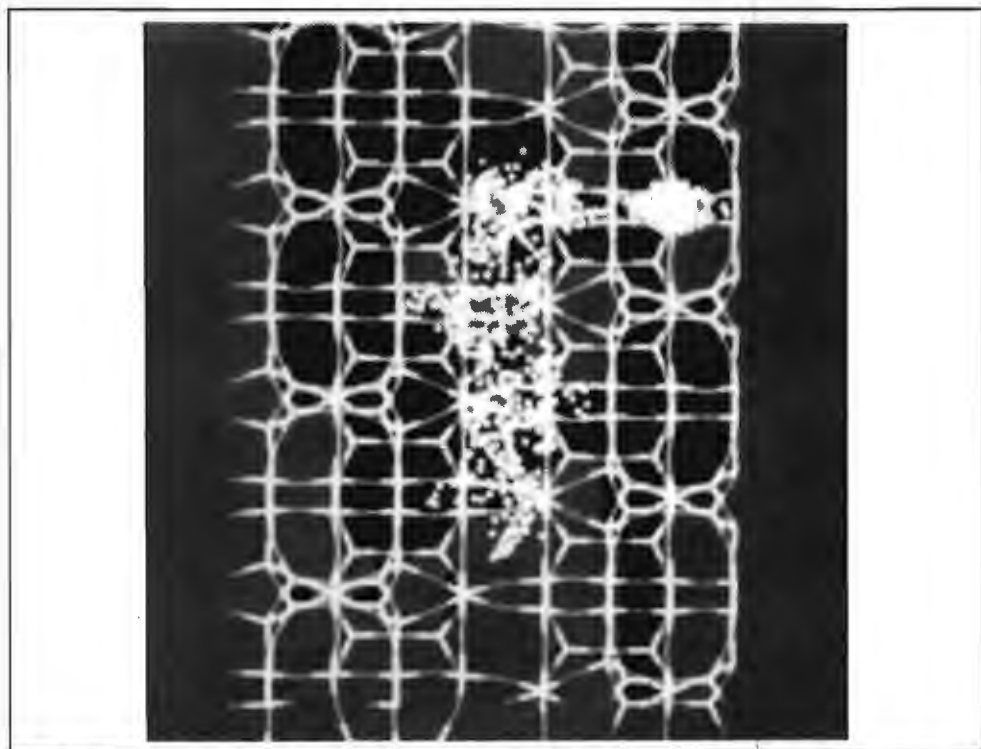
Figure III.15
Methane in MOR; trajectory of a selected methane molecule migrating in MOR. The dots represent positions of the methane molecule at subsequent time intervals. T=298 K, Θ=1, time period=100 ps.

experimentally determined value of 28 kJ/mol has been reported[15]. For the methane-MOR system, an adsorption enthalpy of ≈17 kJ/mol is calculated whereas 23 kJ/mol has been reported[16]. Definitely, a deviation between experimental and computed adsorption enthalpies exists. It is noted, however, that mHxhane is approximated by a single sphere with an effective radius and polarizability. For the calculation of the adsorption enthalpy, this might be a rather crude approximation. On the other hand, it can be envisaged that migration of adsorbates is more dominated by size effects and hence the dynamic features of the calculations show good agreement with experimental data.

Only very recently, *Karger et. al.*[17] reported PFG-NMR data on xenon diffusion in MFI. The measured diffusion coefficients as a function of zeolite loading together with the computed diffusion coefficients are presented in Figure III.17. Again the agreement is very good. The experimental and computed values fully match up with each other over the entire loading range.

At this point, it is noted that both the computed and experimental diffusion coefficients for xenon and methane in MFI differ by a factor 5 (xenon diffusion being slower). Apparently, Molecular Dynamics techniques are able to make a distinction between various diffusivity rates in such a narrow range (see also Table III.3).

Recently, uptake experiments have been performed by *Bulow et. al.*[18] for the xenon-MFI system. The diffusivity was determined to be of the order of 10^{-10} m^2/s and an activation energy
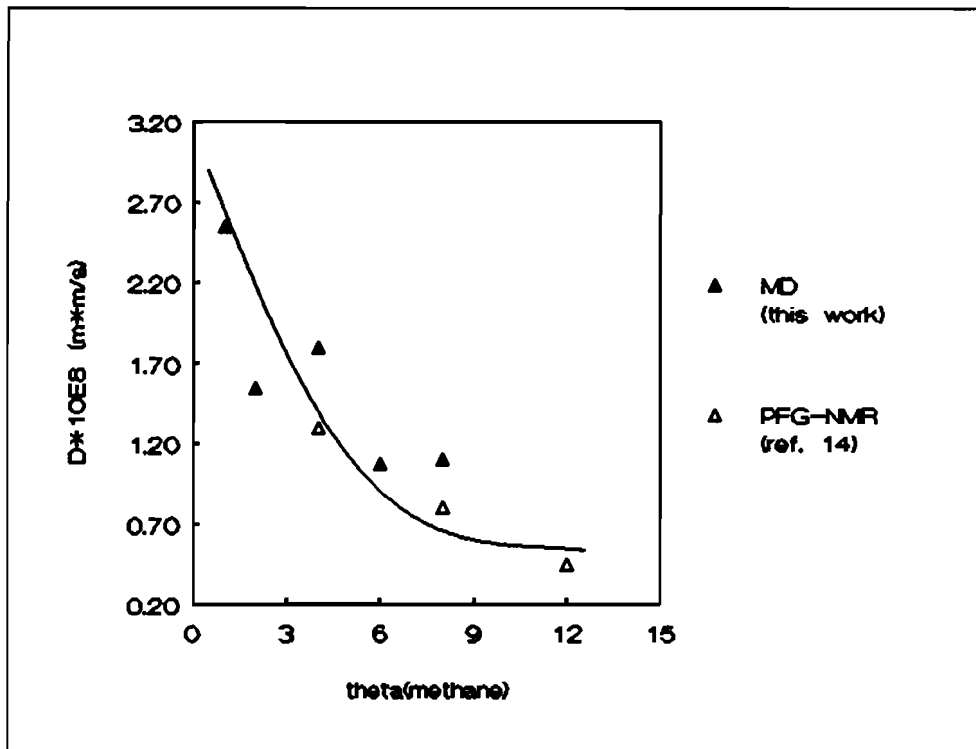
Figure III.16
Methane in MFI; comparison of experimental and computational results of the dependency of diffusion coefficient on zeolite loading (298 K). Loading=nr of methane molecules/$Si_{96}O_{192}$ unit.

for diffusion of 15 kJ/mol was measured. These experiments are in rather poor agreement with PFG-NMR measurements and our calculated diffusivities and activation energies for diffusion ($E_{calculated}$=5.8 kJ/mol). Also other xenon sorption studies report activation energies for diffusion which considerably deviate from the activation energy presented in this chapter. *Barrer*[19] for example, reported an activation energy of 12 kJ/mol for xenon diffusion in zeolite Ca-A. On the other hand, *Bulow*[18]measured an adsorption enthalpy for xenon in MFI of 26.7 kJ/mol which is in excellent agreement with our computed adsorption enthalpy of 27 kJ/mol. This further justifies the statement made earlier that dynamic features of adsorption are dominated by size effects (both methane and xenon simulations give good results) but that adsorption enthalpies are dominated by the quality of the potentials used (apparently, methane assumed as one single sphere is to approximate to yield good adsorption enthalpy results, but xenon is well described by such a potential).

III.4 Results and Discussion II; Poly-atomic Adsorbates

In this section, Molecular Dynamics simulations of diffusion of methane, ethane and propane are
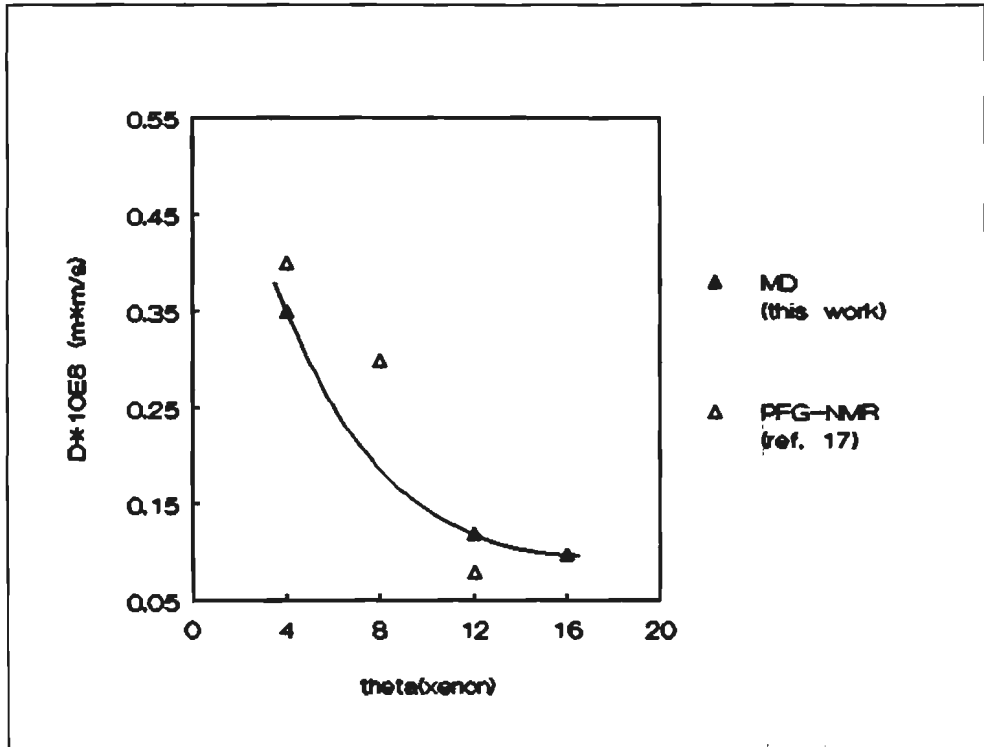
Figure III.17
Xenon in MFI; comparison of experimental and computational results on the dependency of diffusion coefficient on zeolite loading (298 K). Loading is number of xenon atoms/$Si_{96}O_{192}$ unit.

described. All adsorbates are now treated as being poly-atomic and rigid, hence no intramolecular deformations of the adsorbate molecules are considered. Just as in the case of the mono-atomic adsorbates, the zeolite lattice is also considered to be rigid.

Diffusion of methane will be simulated in the zeolites MFI, MOR and EU-1. This study serves to investigate the influence of pore structure and size on the migration process. The results will be interpreted in relation with PFG-NMR spectroscopy.

Since diffusion data for methane, ethane and propane in MFI is available, diffusion of these adsorbates is simulated in MFI. At the end of this section, a comparison with experimental data will be made.

As already mentioned before, all simulations are performed in the NVT ensemble. Concentration effects are eliminated by scaling the zeolite loading with the unit cell size. The loadings under consideration are 2.0, 1.9 and 2.0 adsorbate molecules per $Si_{24}O_{48}$ unit for MFI, MOR and EU-1, respectively. Zeolite units consisting of 192 T-sites are considered and so a total of 16, 15 and 16 adsorbates for MFI, MOR and EU-1, respectively, are involved.

III.4.1 Methane in MFI, MOR and EU-1

Figures III.18, III.19 and III.20 display the mean square displacements of the methane molecules adsorbed versus the time in the zeolites MOR, EU-1 and MFI, respectively. The subfigures a, b, and c represent diffusion in the x-, y-, and z-direction, respectively, while the subfigures d represent the overall mean square displacements versus the time. The x-, y-, and z-directions correspond with the crystallographic a-, b-, and c-axes. The straight lines drawn in the figures are obtained via a linear regression fit to the calculated data.

Although MOR and EU-1 (Figure III.18 and III.19, respectively) have a similar framework topology, the diffusion behavior of methane differs considerably. For MOR, effectively only diffusion in the z-direction is observed. The diffusion coefficients for the separate directions together with the effective pore diameters are listed in Table III.4. From this table, it is seen that diffusion along the z-direction in MOR is one to two orders of magnitude greater than for the x- and y-direction. For EU-1, this is not the case. An expected diffusion along the x-direction is observed, but also diffusion along the z-direction occurs. Table III.4 also lists the diffusion coefficients for methane in EU-1 along the separate directions.   Obviously, in zeolite EU-1, migration from one side-pocket to another occurs. In MOR, this kind of migration does not occur. A possible explanation for this difference might be the difference in the diameters through which migration takes place. The side-pockets of EU-1 are comprised of 12-membered rings while the side-pockets in MOR are comprised of 8-membered rings. The side-pockets in MOR have an entrance diameter which is approximately equil to the molecular diameter of methane (≈ 4.3 A). Thus, whereas methane can easily enter and leave the side-pockets in EU-1, the situation in MOR is different. It can be envisaged that methane is trapped in the MOR side-pockets (which has also been observed in preceeding sections of this thesis) and that the frequency of leaving and entering the side-pockets in MOR is much lower than in EU-1. This feature is displayed in Figure III.21 and III.22. These figures display the centers of mass at subsequent time intervals of all the methane molecules considered over a time $xriod of 50 ps. The density of dots at the various locations
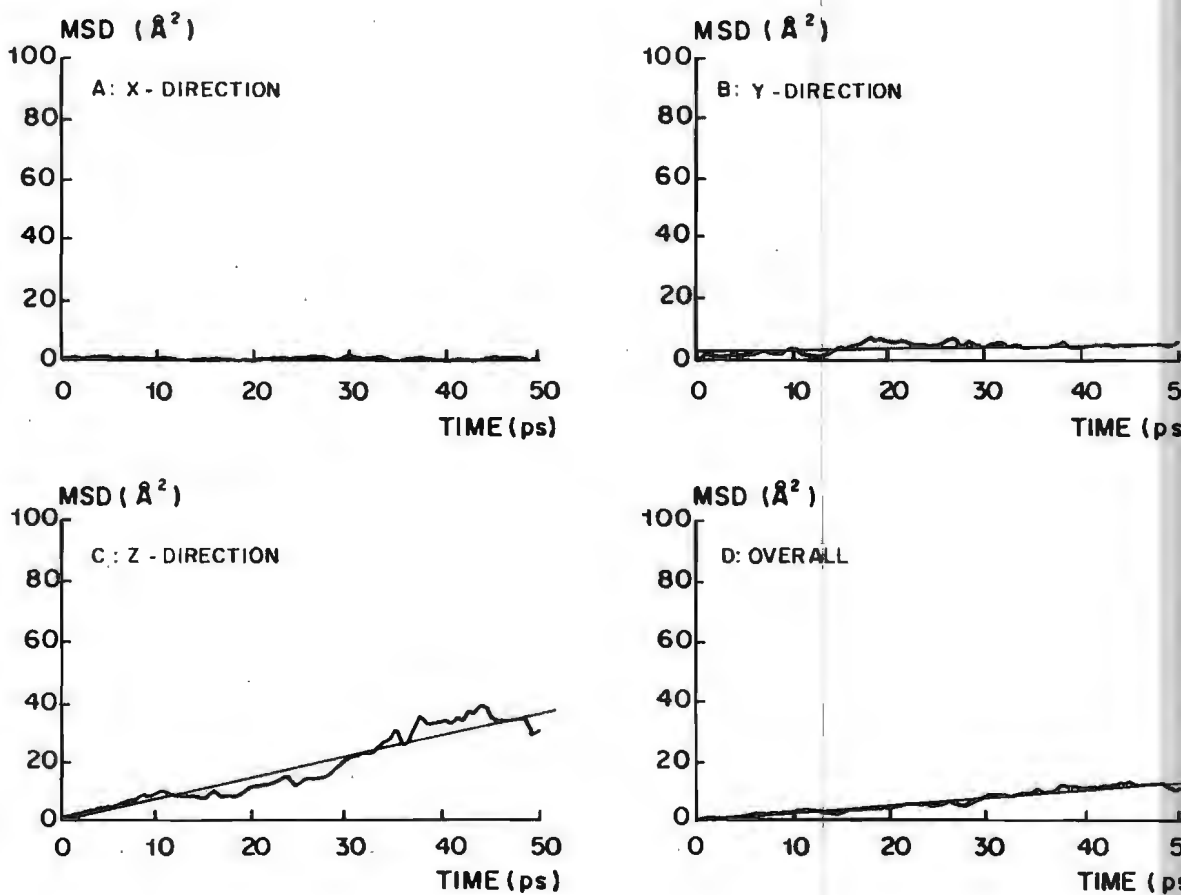
Figure III.20
Mean square displacement versus the time for methane molecules migrating in MFI (Θ=2, T=298 K).

Table III.4

Computed diffusivities (10^8 m²/s) for methane in MOR, EU-1 and MFI and predicted diffusivities ($\Theta=2$, T=298 K).

Anisotropic diffusion coefficients

	x			y			z		
	D_{MD}	D_{NMR}	pore	D_{MD}	D_{NMR}	pore	D_{MD}	D_{NMR}	pore
Zeolite									
MOR	0.01	0.00	-	0.07	-	4.5	0.77	0.77	7.0
EU-1	0.83	0.83	5.5	0.00	0.00	-	0.31	0.00	7.0
MFI	0.44	0.44	5.5	1.33	1.33	5.5	0.11	0.11	-

Overall diffusion coefficients

Zeolite	D_{MD}	D_{NMR}
MOR	0.28	0.77
EU-1	0.38	0.83
MFI	0.62	0.62
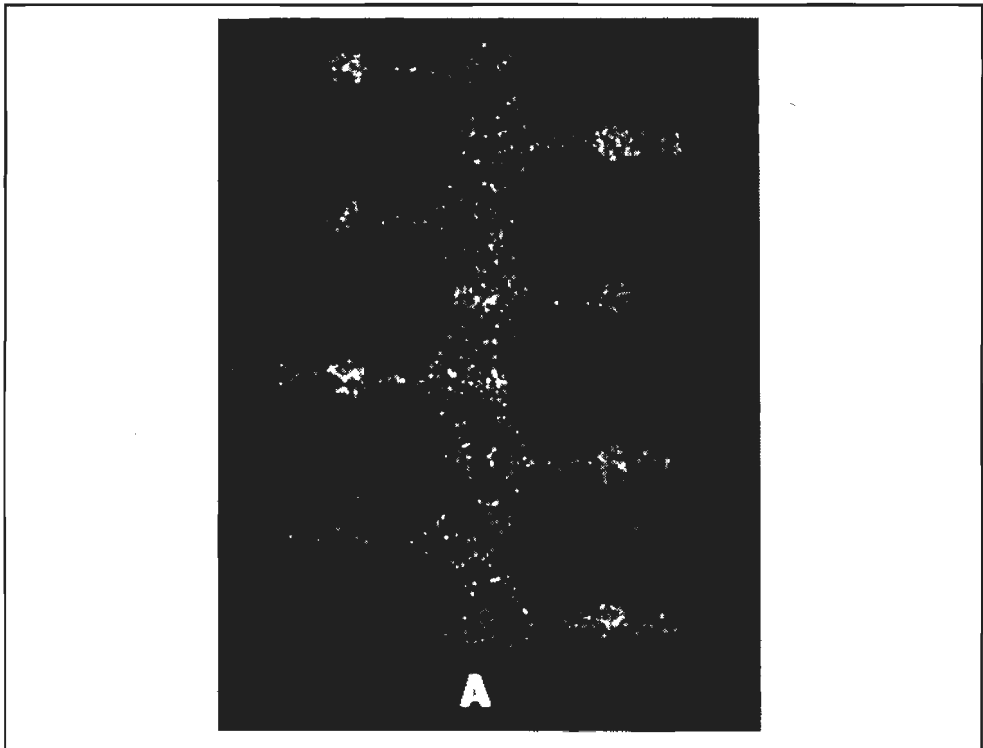
Figure III.21

Methane in MOR; the dots represent the centres of mass of the methane molecules at subsequent time intervals ($\Theta=1.9$, T=298 K).

inside the zeolite frameworks can be considered as a measure for the residence time at that

location. In the MOR framework (Figure III.21), the density of dots in the entrances to the side-pockets is low compared to other locations in the zeolite, indeed indicating that the jumping frequency between main channel and side-pocket is very low. However, in the EU-1 framework (Figure III.22) the methane molecules seem to be free to moveHxn and out the side-pockets since no concentration of dots is observed in the vicinity or inside the side-pockets. It is noted, however, that diffusivity in the y-direction averages out as the simulation time is increased.
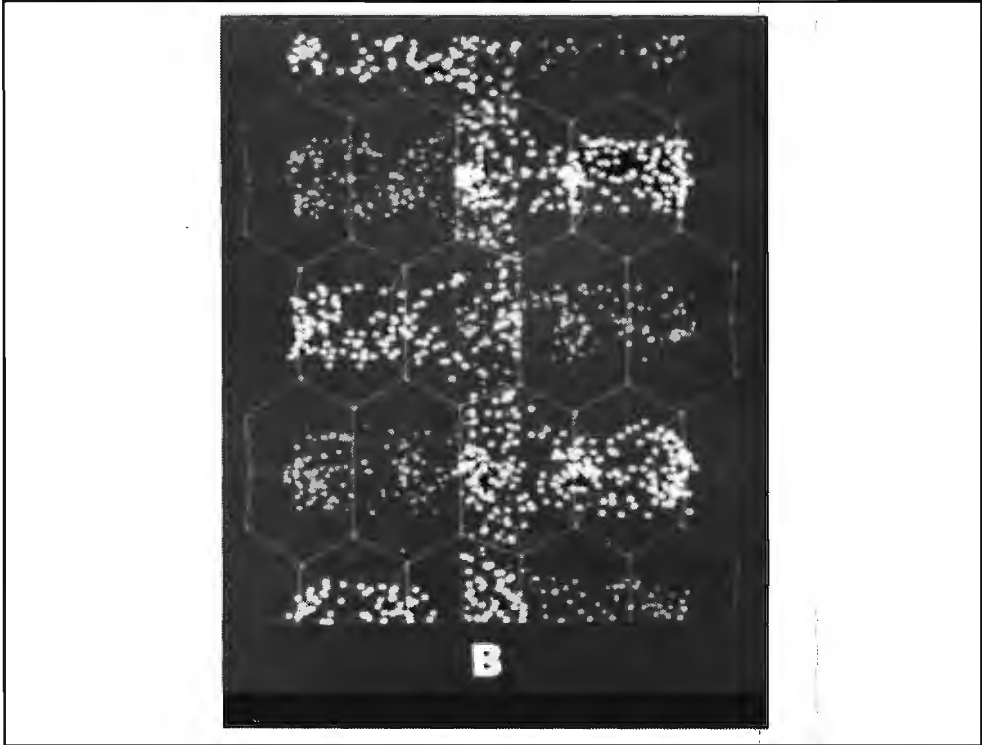
Figure III.22
Methane in EU-1; the dots represent the centres of mass of the methane molecules at subsequent time intervals (Θ=2, T=298 K).

Side-pockets seem to have a considerable effect on molecular masstransport. Considering the diffusion along along the main channels of EU-1 and MOR, no significant difference in diffusivity is observed although the pore diameter in MOR is much larger. It can be assumed that for the time being there are two factors determining the diffusion rate in zeolite micro channels.

The first factor which influences the migration rate is the pore diameter; an increase in pore diameter yields an increased migration rate. The second factor to be considered is the presence of side-pockets and their ability for trapping adsorbate molecules. For the MOR structure, the migration rate for methane in the main channel is greater than in EU-1 because this latter zeolite has a smaller pore diameter. However, as already observed before, the MOR side-pockets are quite effective in trapping methane adsorbates, resulting in a considerable reduction of the migration rate in the main channel. In the EU-1 structure, the adsorbates are much less effectively trapped (see also the difference in the density of dots in Figure III.21 and
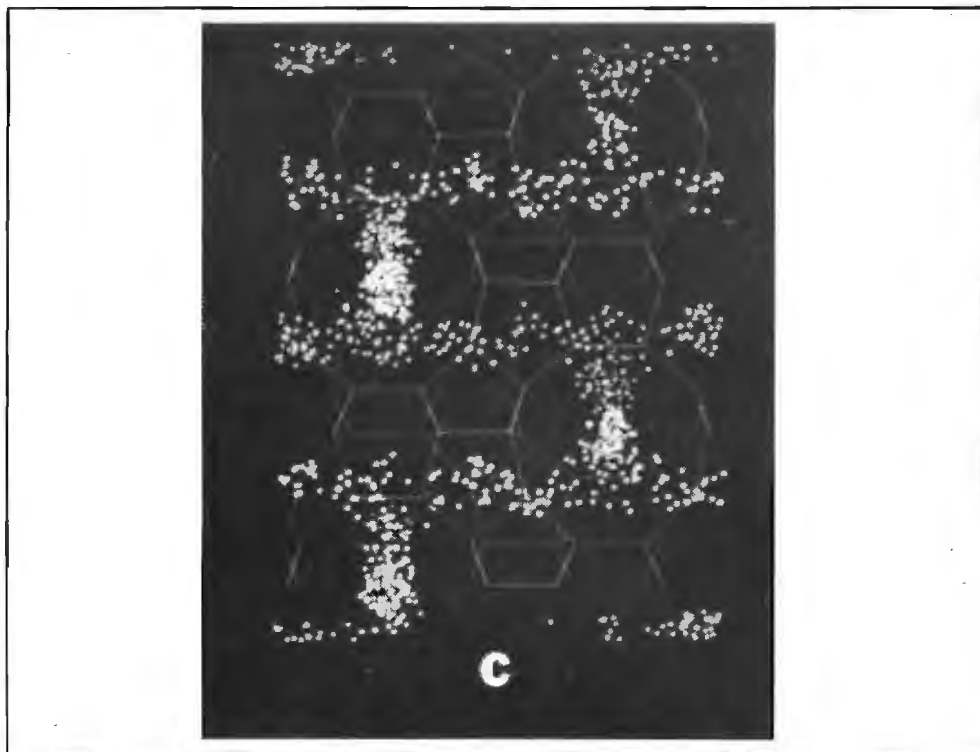
Figure III.23
Methane in MFI; the dots represent the centres of mass of the methane molecules at subsequent time intervals (Θ=2, T=298 K).

III.22) and thus migration rates are much less reduced. It can therefore be envisaged that the effective diffusion through the main channels of MOR and EU-1 is virtually the same.

Another interesting feature emerges if the difusivity of methane in MFI along the straight channel (Figure III.20) is compared with the diffusivity in the (straight) main channels of MOR and EU-1. The diffusion rate in MFI along the straight channel is approximately two times as fast as in EU-1 and MOR. This not only reflects the presence of side-pockets in the EU-1 and MOR structures, but also the openess of the MFI structure for diffusion. In the MFI void space, migration along the straight channels may be interrupted temporarily if an adsorbate enters one of the sinusoidal channels perpendicular to the straight channels. At a following intersection, however, the adsorbate has the possibility to proceed again along the original direction but now via another straight channel. It can be envisaged that following these kinds of trajectories, migration in MFI in any direction is never blocked. However, in the case of adsorbates trapped in side-pockets, only migration in one direction (out of the side-pocket, perpendicular to the main direction of migration) is possible and hence the diffusivity is strongly reduced.

By comparing the diffusivity of methane in MFI along the x- and y-direction, it is observed that the diffusivity along the sinusoidal channel is a factor 3 slower than along the straight channel. It is noted, however, that diffusion in the x-direction cannot proceed via a straight trajectory due to the tortuosity of the channels. Taking this tortuosity into consideration, the

diffusivity in the sinusoidal channels is still smaller compared to the diffusivity in the straight channels altough the pore diameters are of comparable size. Obviously, the tortuosity is a limiting factor for diffusion. This is the third factor following from this study which directly influences migration in zeolite micro pores (the other factors were determined to be the pore diameter and the presence of side-pockets and their ability of trapping adsorbates).

For MFI it is observed that diffusion in the z-direction readily occurs. Apparently, the adsorbate molecules are able to shift between the different channel systems since this is the only way in which migration along the z-direction can occur. Figure III.23 clearly shows the interconnection of the separate directions in the MFI framework. Although the framework density of MFI is smallest of all zeolites considered, its openess for diffusion of methane is highest of all.

Finally, the computational results will be interpreted in relation with experimental diffusivity measurements, in particular PFG-NMR.

In Table III.4, the overall Molecular Dynamics diffusion coefficients, designated as D_{MD}, are obtained by taking the average over the separate directions following from the Molecular Dynamics calculations. By interpreting these numbers, one should consider the time intervals between subsequent pulses in an PFG-NMR experiment and the time scale in which the Molecular Dynamics simulations take place. For example, in EU-1, a diffusion coefficient of $0.31 \cdot 10^{-8}$ m²/s in the z-direction is calculated. However, this diffusion coefficient will not reflect the diffusivity in the z-direction as would be observed by PFG-NMR since no molecular mass transport along the z-direction is possible on a macroscopical time scale. On the (macroscopical) time scale of PFG-NMR ($\approx 10^{-3}$ s), migration along the z-direction in EU-1 will be averaged out. Since the time scale in a Molecular Dynamics simulation is several orders of magnitude smaller ($\approx 10^{-10}$ s), migration along the z-direction can be observed. Thus the experimental diffusion coefficients for methane in MOR and EU-1 are predicted to be $0.77 \cdot 10^{-8}$ m²/s and $0.83 \cdot 10^{-8}$ m²/s, respectively. For MFI on the other hand, migration in all directions is possible, so the overall diffusion coefficient for methane stemming from a Molecular Dynamics simulation or a PFG-NMR measurement is the same. The predicted diffusion coefficients for methane in the zeolites EU-1, MOR and MFI as would be observed by PFG-NMR are also given in Table III.4 and are designated as D_{NMR}.

III.4.2 Methane, ethane and propane in MFI

In this section, results of Molecular Dynamics simulations on the diffusivities of methane, ethane and propane in MFI will be presented. The computational results will be compared with experimental data obtained by PFG-NMR techniques[14].

Figure III.24a, III.24b and III.24c display the mean square displacement of the ethane molecules in MFI versus the time. Figure III.24d displays the overall mean square displacement versus the time. Figures III.25a, III.25b, III.25c and III.25d display the same data for propane in MFI. The straight lines drawn in these figures are obtained via a linear regression fit to the computational data.
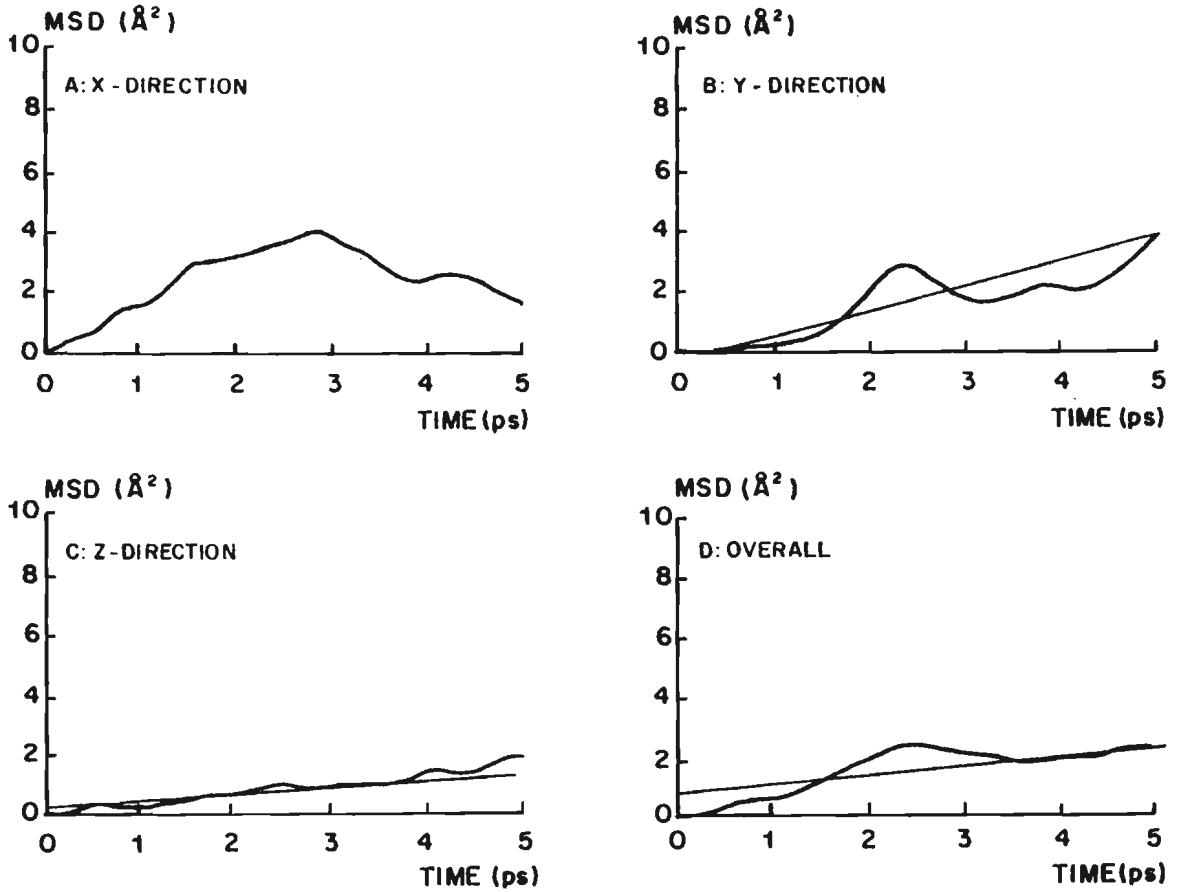
Figure III.24

Mean square displacement versus time for ethane molecules migrating in MFI. Θ=2, T=298 K.

Table III.5
Computed diffusivities (D in 10^8 m²/s) for methane, ethane and propane in MFI (Θ=2, T=298 K).

Adsorbate	D_x	D_y	D_z	D
methane	0.44	1.33	0.11	0.62
ethane	0.30	0.88	0.24	0.47
propane	0.30	0.90	0.03	0.41

Computed diffusion coefficients for the separate directions and the overall diffusion coefficient are listed in Table III.5. For comparison, also the computational results for methane in MFI are presented in this table.

Calculated overall diffusion coefficients are compared with experimental data in Figure III.26. In this figure, the diffusion coefficient as a function of alkane carbon number is represented for a loading of Θ=2 adsorbate molecules per $Si_{24}O_{48}$ at T=298 K.

From Figure III.26, it is seen that for methane and ethane the agreement with experimental data is good. However, in the case of propane, a large deviation shows up. The origine of this deviation might stem from the approximation of propane being rigid. Examination of the diffusion coefficients for the separate directions in Table III.5 and Figures III.25a through d shows that diffusion shows that diffusion in the straight and sinusoidal channels readily occurs, but that diffusion in the z-direction is virtually neglicible. This indicates that during the simulation the propane molecules were not able to diffuse from one channel system to the other probably due to their rigidness. This computational artefact enhances the diffusivity considerably. Furthermore, it is highly unlikely that propane molecules migrate in the micropores in the same fashion as bouncing balls. This, however, is the implication of the rigidness assumption. For smaller adsorbates (methane and ethane), this can be envisaged, but it is expected that higher alkanes such as propane migrate along the zeolite walls in a creeping motion[21] resulting in a considerable decrease of the diffusivity. The rigid constraint on the molecules, however, does not allow a creeping motion.

Finally, Figure III.27 displays computed and experimental adsorption enthalpies for MFI as a function of the alkane carbon number. For all three adsorbates considered, a good agreement between experiment and simulation is found. This agreement indicates that the potentials used are reliable. Therefore, the mismatch of

the propane diffusion coefficient in MFI can be ascribed to approximations considering the rigidness of the adsorbate molecules.
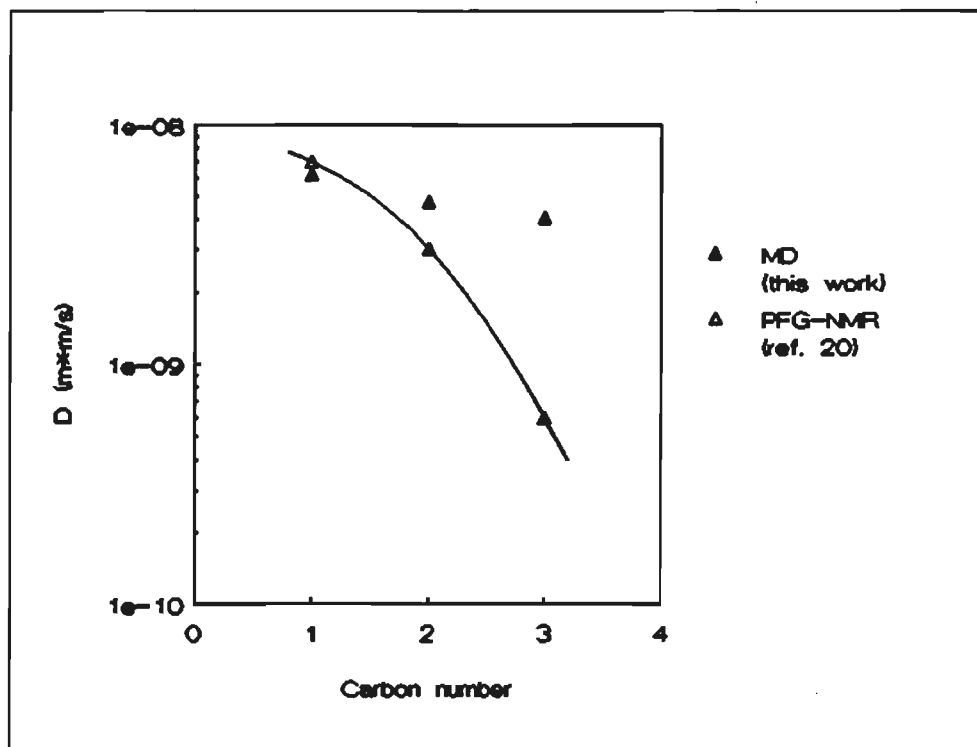
<u>Figure III.26</u>
Diffusion coefficient in MFI as a function of alkane carbon number (Θ=2, T=298 K).

III.5 Conclusions

In this chapter, it has clearly been shown that MD simulations can be conveniently used to describe the molecular basis of diffusion in zeolitic void spaces. Especially the simulation of small adsorbates yielded very good agreement with experimental data.

The simulation of larger adsorbates was somewhat more troublesome. This was probably due to the assumption of both the adsorbate and zeolite lattice being rigid. Heats of adsorption were very well predicted, indicating that migration characteristics are dominated by steric effects and heats of adsorption by the choice and quality of the interaction potentials used.

Finally, computer graphics turned out to be clarifying tools in visualizing the computational results. Especially the effect of strong adsorption sites on the migration process was nicely demonstrated in the case of methane diffusion in MFI.
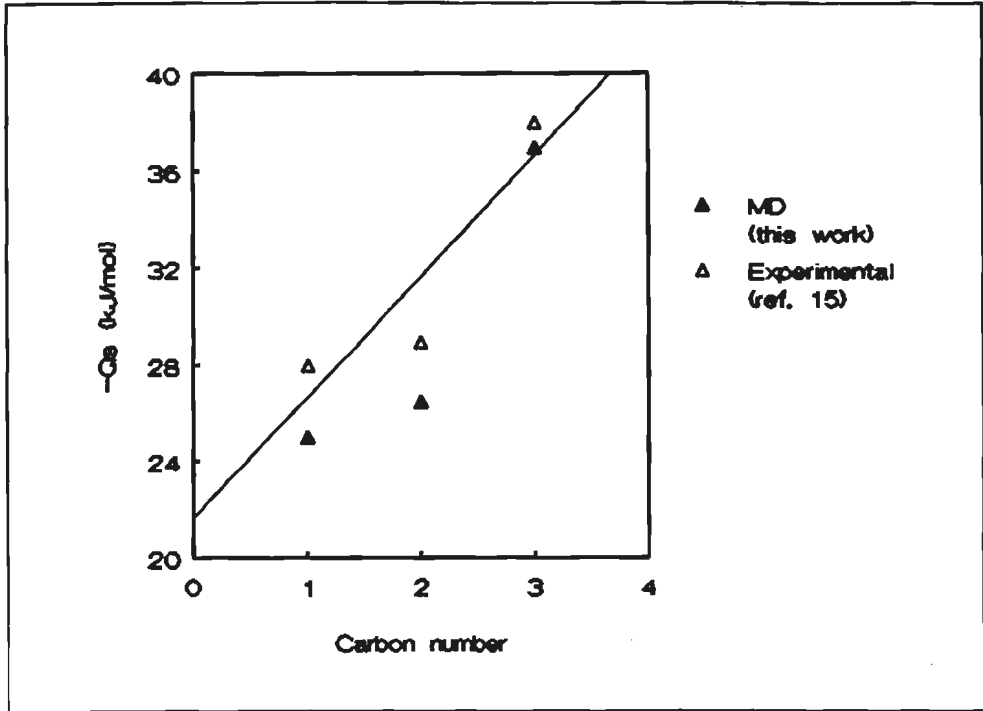
Figure III.27
Adsorption enthalpy in MFI as a function of alkane carbon number ($\Theta=2$, T=298 K).

Appendix: Principles of Molecular Dynamics

Determination of thermodynamic properties

In chapter II, a Monte Carlo procedure for the simulation of adsorption phenomena in various zeolites covering a range of Al/Si ratios and temperatures has been employed. Monte Carlo simulations deal with systems which are in equilibrium and so static thermodynamic properties such as heats of adsorption and average siting behavior can be derived. In a Monte Carlo procedure, these properties are derived from averaging over an ensemble of equilibrium configurations. For a static thermodynamic property A, the averaged value of A following from a Monte Carlo simulation is given by (see chapter II):

$$<A> = \left(\frac{1}{M}\right)\sum_{\Gamma=1}^{M} A_{\Gamma} \tag{A.1}$$

wherein M is the number of Monte Carlo sampling points, i.e. the number of configurations generated in the chain. A_{Γ} is the actual value of the property A in the configuration τ. At this point, it is noted that the time interval between two Monte Carlo sampling configurations $\Gamma=i$ and $\Gamma=i+1$ is entirely arbitrary. This point will be further treated in a subsequent part of this appendix.

Molecular Dynamics simulations simulate the time evolution explicitly. So Molecular Dynamics not only allow the evaluation of static thermodynamic properties but also allow the determination of dynamic properties such as diffusivities and site residence times of molecules adsorbed in zeolitic pores. These dynamic properties are derived by generating a system trajectory followed by averaging over the time. Thus, for any thermodynamic property A, the time averaged

value of A following from a Molecular Dynamics simulation is given by:

$$\langle A \rangle = \left(\frac{1}{t}\right)\sum_{\theta=1}^{M} A_\theta \delta t_\theta \tag{A.2}$$

wherein t is the total simulation time and δt_θ is the length of step Θ. A_θ is the value of property A at time $t = t_\theta$. Obviously, if M is the total number of time steps in the simulation, then:

$$\sum_{\theta=1}^{M} \delta t_\theta = t \tag{A.3}$$

From equation (A.2) it follows that the computation of properties might be cumbersome if the system under consideration is evolving very slowly in time. For these kinds of system, generally a very long Molecular Dynamics run will be neccessary. When one is interested in static properties only, a Monte Carlo procedure will shorten the simulation considerably since with this technique, also 'unphysical' system changes will occur: that is, changes which do not proceed along the path of the time trajectory.

Algorithm

Generating a Molecular Dynamics trajectory is purely based on classical *Newtonian* mechanics. An ensemble of N particles moving in a force field is considered. The force on particle i at time t is denoted by the vector $F_i(t)$ and its position at time t by $r_i(t)$. A *Taylor* expansion of $r_i(t)$ around t results in:

$$r_i(t+\delta t) = r_i(t) + \left(\frac{dr_i(t)}{dt}\right)_t \delta t + \frac{1}{2}\left(\frac{d^2 r_i(t)}{dt^2}\right)_t \delta t^2 +)(\delta t^3) + O(\delta t^4) \tag{A.4}$$

$$r_i(t-\delta t) = r_i(t) - \left(\frac{dr_i(t)}{dt}\right)_t \delta t + \frac{1}{2}\left(\frac{d^2 r_i(t)}{dt^2}\right)_t \delta t^2 - O(\delta t^3) + O(\delta t^4) \tag{A.5}$$

and combination of equation (A.4) and (A.5) yields:

$$r_i(t+\delta t) = 2r_i(t) - r_i(t-\delta t) + \left(\frac{d^2 r_i(t)}{dt^2}\right)_t \delta t^2 + O(\delta t^4) \tag{A.6}$$

or, recalling *Newton's* law F=m.a:

$$r_i(t+\delta t) = 2r_i(t) - r_i(t-\delta t) + \left(\frac{F_i(t)}{m_i}\right)_t \delta t^2 + O(\delta t^4) \tag{A.6}$$

Analogeously, it can be easily derived that:

$$\left(\frac{dr_i(t)}{dt}\right)_t = v_i(t) = \frac{r_i(t+\delta t) - r_i(t-\delta t)}{2\delta t} \tag{A.7}$$

wherein m_i is the mass of particle i and $v_i(t)$ its velocity at time t. Equation (A.6) clearly shows that, given the forces on the particles, it is possible to generate a trajectory in time without having any knowledge about the particle velocities. However, determination of the velocities might be

useful for the evaluation of the particle ensemble temperature from the kinetic energy of the system:

$$E_{kin}(t) = \frac{1}{2}\sum_{i=1}^{N} m_i v_i^2(t)$$ (A.8)

and hence

$$T(t) = \left(\frac{2}{3Nk}\right)E_{kin} = \left(\frac{1}{3Nk}\right)\sum_{i=1}^{N} m_i v_i^2(t)$$ (A.9)

wherein k is the *Boltzmann* constant.

Equations (A.6) through (A.9) define the body of a Molecular Dynamics algorithm. From equation (A.9), it follows that the temperature of the ensemble of particles is not constant in time but fluctuates around the average temperature. Hence, the kinetic energy of the system is not constant in time either. It is noted, however, that the total energy, E_{tot}, is conserved throughout the whole simulation. The total energy is given by:

$$E_{tot} = E_{pot} + E_{kin}$$ (A.10)

wherein the potential energy, E_{pot}, is related to the forces acting on the particles in the ensemble via:

$$F = \frac{-dE_{pot}}{dr}$$ (A.11)

Such an algorithm is referred to as a NVE algorithm[22] (constant number of particles, N, constant volume, V, and constant total energy, E). The simulation temperature, T_s, in a NVE simulation can be determined afterwards by integrating over the time:

$$T_s = \left(\frac{1}{t}\right)\int T(t)dt$$ (A.12)

The NVE algorithm is employed in cases wherein the conservation of the total energy is required, that is, when a microcanonical (NVE) ensemble has to be sampled. However, in many actual situations, a constant temperature, rather than a constant total energy, has to be maintained. In these cases, the canonical ensemble is sampled and one needs to employ a NVT algorithm[22] (constant number of particles, N, constant volume, V, constant temperature, T). This algorithm is basically the same as the NVE algorithm but a temperature correction step is incorporated in order to ensure a constant temperature. Equation (A.6) is used in order to predict the new positions of the particles. Equations (A.8) and (A.9) are used to calculate the temperature, $T_{calc}(t)$ of the ensemble. Let $T_w(t) = T_w$ be the desired simulation temperature, then

$$T_w - \left(\frac{T_w}{T_{calc}(t)}\right) T_{calc}(t) \tag{A.13}$$

and so, applying equation (A.9):

$$T_w - \left(\frac{T_w}{T_{calc}(t)}\right)\left(\frac{1}{3Nk}\right)\sum_{i-1}^{N} m_i v_i^2(t)$$

or:

$$T_w - \left(\frac{1}{3NK}\right)\sum_{i-1}^{N}\left[\sqrt{\frac{T_w}{T_{calc}(t)}} v_i(t)\right]^2 \tag{A.14}$$

Equation (A.14) implies that the velocities of the particles at time t need to be scaled by a factor $\sqrt{T_w/T_{calc}(t)}$ in order to ensure a constant temperature T_w. With these scaled velocities and the forces on the particles, the new (corrected) positions of the particles are calculated via equation (A.6) with $d^2r_i(t)/dt^2=0$.

Basically, the implications of equation (A.14) is that the surrounding of the system under consideration is regarded as a medium with an infinite heat capacity (isothermic bath). All heat which is added or withdrawn from the system comes, respectively goes to the isothermic bath. In this chapter, the NVT algorithm has been used since self-diffusion in zeolites can be considered as being an isothermic process. It is noted that temperature scaling for every MD step is rather rigorous. Obviously, more elegant way of temperature scaling are available and described in literature[22]. However, it goes beyond the scope of this thesis to discuss these methods in detail.

Molecular Dynamics simulations of diffusion and adsorption in zeolites

Molecular Dynamics procedures for the simulation of diffusion and adsorption processes in zeolites (or microporous materials in general) are analogous to those procedures applied for the simulation of liquids[22]. So, the same algorithms as outlined in the preceeding section can be used.

In this section, the derivation of the force field F as defined in equation (A.11) will be discussed. Furthermore, it will be pointed out how to simulate diffusion and adsorption using Molecular Dynamics techniques. This section will be restricted to mono-atomic adsorbates only. In a subsequent section of this appendix, also diffusion and adsorption simulation of poly-atomic adsorbates will be treated.

Using Lennard-Jones type potentials (chapter II) for the adsorbate-zeolite and adsorbate-adsorbate interactions, the total interaction energy for adsorbate j is given by:

$$E_j - \sum_{i-1}^{N_{ox}} \frac{B_{ij}}{r_{ij}^{12}} - \frac{A_{ij}}{r_{ij}^{6}} + \sum_{k \neq j}^{N} \frac{B_{kj}^*}{r_{kj}^{12}} - \frac{A_{kj}^*}{r_{kj}^{6}} \tag{A.15}$$

A_{ij}, A_{kj}^*, B_{ij} and B_{kj}^* are the van der Waals attraction and repulsion constants, respectively. The labels i run over all the oxygen atoms in the zeolite (total number zeolite oxygen atoms considered: N_{ox}) whereas k runs over all the adsorbates except adsorbate j. The interatomic distances are denoted by r_{ij} and r_{kj}, respectively.

The average potential energy of the ensemble under consideration, *i.e.* the adsorption enthalpy, at a given time $t=t_m$ in the Molecular Dynamics trajectory of the adsorbates interacting with the zeolite and each other is given by:
with N the number of adsorbates in the zeolite. The factor 1/2 is introduced to avoid double counting.

$$<E_{pot}>_m = -\left(\frac{1}{N}\right)\sum_{j=1}^{N}\sum_{i=1}^{N_{ox}}\frac{B_{ij}}{r_{ij}^{12}} - \frac{A_{ij}}{r_{ij}^{6}} + \frac{1}{2}\sum_{k\neq j}^{N}\frac{B_{kj}^{*}}{r_{kj}^{12}} - \frac{A_{kj}^{*}}{r_{kj}^{6}} \tag{A.16}$$

From equation (A.11), an expression for the force acting on adsorbate j can be derived:

$$F_j(t) = \sum_{i=1}^{N_{ox}}\left(\frac{12B_{ij}}{r_{ij}^{14}} - \frac{6A_{ij}}{r_{ij}^{8}}\right)(r_i - r_j) + \sum_{k\neq j}^{N}\left(\frac{12B_{kj}^{*}}{r_{kj}^{14}} - \frac{6A_{kj}^{*}}{r_{kj}^{8}}\right)(r_k - r_j) \tag{A.17}$$

Note that $F_j(t)$ is a function of the time since $r_{ij \text{ and } rkj}$ are time-dependent. Note also that $F_j(t)$ is a vector whereas $E_{pot,j}$ is a scalar. Equation (A.17) defines a force field for adsorbates migrating in the micropores of a zeolite. This force field can be directly applied in the Molecular Dynamics algorithms as discussed in the previous section to generate a system trajectory in time. From this trajectory, dynamic properties such as overall diffusivities are easily computed via the *Einstein* relation[16]:

$$D = \frac{<r^2>}{6t} \tag{A.18}$$

wherein $<r^2>$ is the mean square distance travelled by the adsorbate molecules during a time t. Diffusivities along the x-, y-, or z-direction follow from:

$$D = \frac{<r_x^2 + r_y^2 + r_z^2>}{6t} = \frac{D_x + D_y + D_z}{3} \tag{A.19}$$

with

$$D_u = \frac{<r_u^2>}{2t} \tag{A.20}$$

wherein u denotes one of the three directions x, y or z.

Adsorption enthalpies (Q_s) are calculated by using equation (A.4):

$$<Q_s> = \left(\frac{1}{t}\right)\sum_{m=1}^{M}<E_{pot}>_m \delta t_m \tag{A.21}$$

wherein $<E_{pot}>$ is given by equation (A.16), M is the number of time steps taken for the simulation and δt_m is the time step length of step m. Usually, the time step length is fixed at a given value δt.

Finally, assuming that diffusion in zeolites obeys the *Arrhenius* equation:

$$D = D_0 e^{\frac{-E_A}{kT}} \tag{A.22}$$

then, by plotting ln(D) versus 1/T, the activation energy, E_A, for diffusion can be determined.

Molecular Dynamics of poly-atomic adsorbates

In Molecular Dynamics studies of an ensemble of poly-atomic adsorbate molecules, one has to consider both the dynamics of the molecules as a whole (translational and rotational) and the deformation of the molecular geometry due to inter- and intra-molecular interactions. Furthermore, in some cases also the dynamics of the zeolite lattice is taken into account. Since the zeolite is considered to have an infinite weigth, only lattice deformations are taken into account. It will be obvious that the degree of complexity of the Molecular Dynamics simulation is accompanied with a fast increase in the demand of computer power.

In this section, the methodolgy of the dynamics of poly-atomic adsorbates in a zeolite will be discussed. Both the rigid molecule (fully constrained) and the flexible molecule (partially constrained or fully unconstrained) approximation will be considered. In all cases, the dynamics of the zeolite lattice is neglected.

In the dynamics of poly-atomic molecules, a formal distinction is made between inter- and intra-molecular forces on the atoms of the molecule. The forces acting within a molecule (intra-molecular) are in general at least an order of magnitude greater than those acting between molecules (inter-molecular). The underlying reason is that intra-molecular forces stem from bond vibrations and deformations of bondangles from the equilibrium value. The inter-atomic force between two adjacent atoms i and j within one molecule is the derivative of the inter-atomic interaction potential ϕ_{ij}^{bond}:

$$F_{ij}^{intra} = \frac{-d\phi_{ij}^{bond}}{dr_{ij}} \tag{A.23}$$

in which ϕ_{ij}^{bond} is usually approximated by a harmonic interaction potential:

$$\phi_{ij}^{bond} = k_{ij}(r_{ij} - r_{ij0})^2 \tag{A.24}$$

with k_{ij} being a force constant and r_{ij0} the equilibrium inter-atomic distance and r_{ij} the actual value. A graphical illustration of ϕ_{ij}^{bond} is given in Figure A.1. Both variations in bondlengths and variations in bondangles can be described by an expression as given by equation (A.24).

Inter-molecular forces are much weaker. Considering pair potentials between atoms in different molecules, the inter-atomic force between two atoms i and j of different molecules is the derivative of a (weak) *van der Waals* potential:

$$F_{ij} = \frac{-d\phi_{ij}^{vdw}}{dr_{ij}} \tag{A.25}$$

with ϕ_{ij}^{vdw} represented in Figure A.1. The general form of such a potential is given in Figure A.1.

A non-linear and non-planar poly-atomic molecule has $3n-6$ internal degrees of freedom with n being the total number of atoms from which the molecule is built up. The degrees of freedom are the intra-molecular stretch- and bend vibrations. The potentials involved in these vibrations are represented by equation (A.24). To incorporate the intramolecular movements in a Molecular Dynamics simulation, a knowledge of the intra-molecular potentials (k_{ij} and r_{ij0} in equation A.24 is required. If all the internal degrees of freedom are taken into account, then there are no constraints on the molecular geometry.. This case is denoted as fully unconstrained dynamics.

For any molecule of moderate complexity, such an approach would be very complicated because the intra-molecular potential has to be defined for each distinct atom pair within every
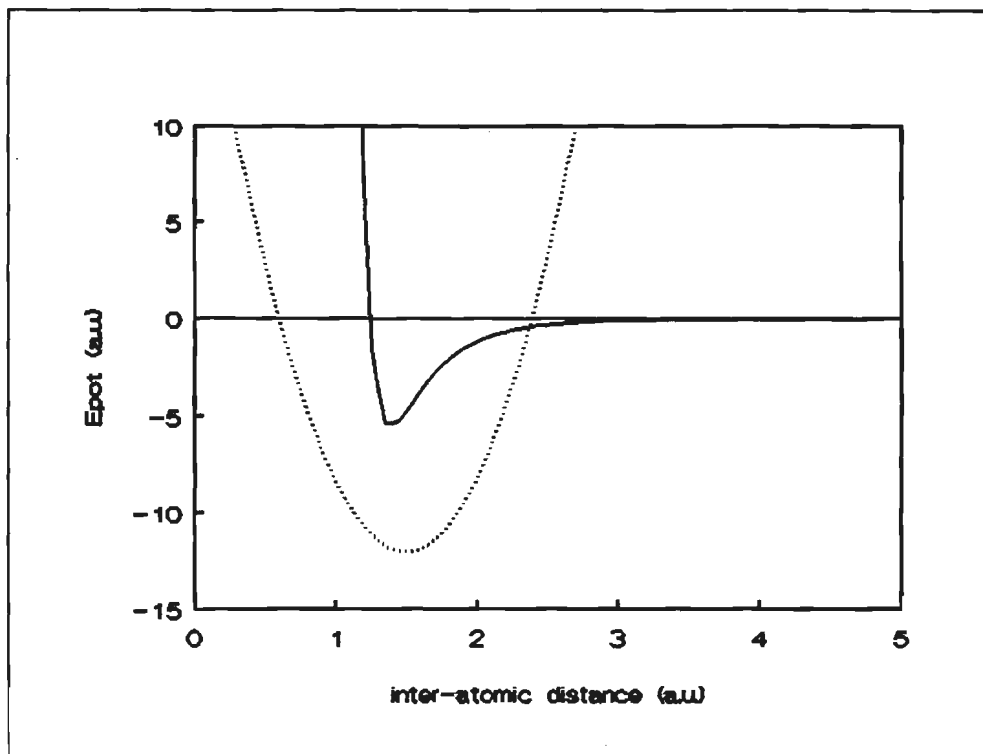
Figure A.1
General form of atom-atom pair potentials for intra- (dotted curve) and inter-molecular (solid curve) interactions.

adsorbate molecule. The potential energy for one adsorbate molecule labeled μ consisting of n atoms migrating in the force field due to the zeolite and the presence of N-1 other adsorbate molecules is given by:

$$E_{pot,\mu} = \sum_{i=1}^{N_{ox}} \sum_{j=1}^{n} \phi_{ij}^{(1)} + \sum_{\tau \neq \mu}^{N} \sum_{j=1}^{n} \sum_{k=1}^{n} \phi_{\tau kj}^{(2)} + \frac{1}{2} \cdot \sum_{j=1}^{n} \sum_{m \neq j}^{n} \phi_{mj}^{(3)} \qquad (A.26)$$

wherein $\phi_{ij}^{(1)}$ is the interaction potential between zeolite oxygen atom i and adsorbate atom labeled j, $\phi_{\tau kj}^{(2)}$ is the interaction potential between atom j of adsorbate μ and atom k of adsorbate τ, and $\phi_{mj}^{(3)}$ is the intra-molecular interaction potential of atom j with atom m within adsorbate μ.

In most cases, one does not want to incorporate all intra-molecular motions and so a number of constraints, $W \leq 3n-6$, on the molecular geometry of the adsorbates is introduced; this case is denoted as constrained dynamics. For example, the time scale in which the bond stretching vibrations take place is much smaller than the time scale in which translation of the molecular centre of mass occurs. Thus, incorporating these intra-molecular vibrations effectively results in a Molecular Dynamics simulation over a very small time period in which the vibrations are properly accounted for but the molecular centre of mass hardly changes position.

In the constrained dynamics case, the equation of motion of the ith atom of an adsorbate molecule is given by:

wherein m_i is the atomic mass of atom i, r_i its position and F_i is the force due to inter-molecular interactions and to those intra-molecular interactions that are explicitly included in the potential. The constraint force on atom i is represented by G_i. The constraint forces are introduced to ensure

$$m\left(\frac{d^2r_i}{dt^2}\right)-F_i+G_i \tag{A.27}$$

that the constraints

$$\sigma_{km}-r_{km}^2(t)-r_{km0}^2\le e_{km} \tag{A.28}$$

are satisfied at all times. In equation (A.28), $r_{km0}2$ is the square of the equilibrium distance between atom k and m in the adsorbate molecule while $r_{km}^2(t)$ is the actual value. The parameter ε_{km} represents the setpoint of the constraint and usually is a small number (eg. 10^{-4} Angstrom^2).

Having W$\le$3n-6 constraints, the constraint forces can be written as:

$$G_i-\frac{1}{2}\cdot\sum_{j=1}^n \nabla_{r_i}(\Gamma_{1,2}\cdot\sigma_{1,2}+\Gamma_{1,3}\cdot\sigma_{1,3}+...+\Gamma_{1,W}\cdot\sigma_{1,W}+\Gamma_{2,3}\cdot\sigma_{2,3}+...+...+\Gamma_{W-1,W}\cdot\sigma_{W-1,W}) \tag{A.29}$$

wherein the Γ's are undetermined (*Langrangian*) multipliers. Equations (A.27) together with (A.29) are the *Langrangian* equations of motion. Because the constraints are defined by equation (A.28), the constraint forces G_i are linear in the inter-atomic distances r_{km}.

The constraint forces enter into the *Verlet* algorithm via[22]:

$$r_i(t+\delta t)-r_i^*(t+\delta t)+\frac{\delta t^2}{m_i}G_i(t) \tag{A.30}$$

where $r_i^*(t+\delta t)$ is the position which would have been reached in the absence of any constraints. Equations (A.30) (n in number, n being the number of atoms in the adsorbate molecule) can be combined to yield the set of interatomic distances as defined in equations (A.28). This set consists of W equations, W being the number of constraints. Taking the square moduli of both sides of these equations and applying the constraints (A.28), the result is a set of quadratic equations in $\Gamma_{1,2}$, $\Gamma_{1,3}$, ..., $\Gamma_{1,W}$, $\Gamma_{2,3}$, ..., $\Gamma_{W-1,W}$ which can be solved for the multipliers Γ. In practice, since terms linear in Γ are proportional to δt^2, while second order terms are proportional to δt^4, these equations are solved by an iterative procedure. This procedure consists of dropping the quadratic terms and solving the remaining set of linear equations for Γ. These calculated values are substituted back in the quadratic terms of the original set yielding another set of linear equations which is again solved for Γ to yield improved values until convergence is reached.

References

1. I.E. Maxwell, J. Incl. Phenom., 1986, 4(1), p. 1.
2. E.F. Vansant, Proc. Int. Symp. 'Innovation in Zeolite Materials Science', 1988, p. 143.
3. H. Lermer, M. Draeger, J. Steffen, K.K. Unger, Zeolites, 1985, 5, p. 131.
4. W.M. Meier, Z. Kristallogr., 1961, 115, p. 439.
5. N.A. Briscoe, O.W. Johnson, G.T. Kokotailo, L.B. Cusker, M.D. Shannon, Zeolites, 1988, 8, p. 74.
6. A.V. Kiselev, A.A. Lopatkin, A.A. Schulga, Zeolites, 1985, 5, p. 261.
7. A.G. Bezus, A.V. Kiselev, A.A. Lopatkin, P.A. Du, J. Chem. Soc. Far. Trans. II, 1978, 74, p. 367.
8. A.V. Kiselev, P.A. Du, J. Chem. Soc. Far. Trans. II, 1981, 77, p. 1.
9. A.V. Kiselev, A.A. Lopatkin, A.A. Schulga, J. Chem. Soc. Far. Trans. II, 1981, 77, p. 17.
10. A.V. Kiselev, A.A. Lopatkin, A.A. Schulga, Zeolites, 1985, 5, p. 261.
11. W.M. Meier, D.H. Olsen, 'Atlas of Zeolite Structure Types', 1987.
12. M. Bulow, private communications.
13. J. Karger, private communications.
14. J. Caro, M. Bulow, W. Schirmer, J. Chem. Soc, Far. Trans. I, 1985, 81, p. 2541.
15. H. Papp, W. Hinsen, N.T. Do, M. Baerns, Thermochim. Acta., 1984, 82, p. 137.
16. R.M. Barrer, 'Zeolites: Science and Technology', NATO ASI series E, 80, p. 227.
17. W. Heink, J. Karger, M. Pfeifer, F. Stallmach, J. Chem. Soc., in press.
18. M. Bulow, private communications.
19. R.M. Barrer, 'Zeolites and Clay Materials', 1978, Ac. Press, London.
20. H. Stach, H. Thamm, K. Fiedler, B. Grauert, W. Wieker, E. Jahn, G. Ohlmann, "New Developments in Zeolite Science and Technology', Stud. Surf. Sc. and Catalysis, 1986, 28, p. 539.
21. E.G. Derouane, J.M. Andre, A.A. Lucas, Chem. Phys. Lett., 1987, 137(4), p. 336.
22. M.P. Allen, D.J. Tildesley, 'Computer Simulation of Liquids', 1988, Clarendon Press, Oxford.

CHAPTER IV

ON THE DYNAMICS OF ORGANIC-ZEOLITE INTERACTIONS: TETRAMETHYLAMMONIUM IN SODALITE

IV.1. Introduction

Various organic molecules and/or (organic) cations are generally used in the synthesis of different zeolites. The role of the organics has often been, and still is, a subject of much debate. At least four roles of the organics can be distinguished from several studies.

Very often, only the templating or structure directing role as proposed by *Flanigen*[1] back in 1973 is stressed. A clear example in this context is the role of the tetrapropylammonium (TPA) cation in ZSM-5 synthesis. It is thought that TPA stabilizes certain alumino-silicate species which replicate themselves through structure specific interactions. There is, however, no one-to-one correlation between the molecular geometry of the organic and the macroscopic zeolite structure ultimately obtained. This indicates that the templating role is certainly not the only one.

Lok[2] reviewed the role of the organic and he assumed that the presence of the organic has a large influence on the (reaction) gel chemistry (Ph, composition, solubility and presence of various precursor species, etc.). It was indicated that a structure directing role was only operative only if the right gel chemistry is present.

Recently, zeolite crystallization mechanisms have been proposed in which the crystalline phase evolved from specific double n-ring alumino-silicate species in solution[3]. It was suggested that the presence of such species is related to the organics used.

Finally, the stabilizing role of the organic has been highlighted by *Barrer*[4]. It was proposed that the organics act like pore fillers and hence prevent water to interact with the hydrophobic zeolitic inner surface (in the case of siliceous zeolites). Obviously, the void filling role is strongly related to the templating role, as has also been shown previously[5].

Although the influence of organics on the formation of various zeolites has been extensively studied, only little attention has been paid to the dynamic features of organic-zeolite interactions. Information that can be deduced from such studies might involve insight into the time scale on which organic-zeolite interactions occur and the influence of both organic dynamics and zeolite lattice dynamics.

In this chapter we report the results of a comparative investigation of the dynamics of the tetramethylammonium cation occluded in the ß-cages of zeolite Sodalite. TMA is generally considered as the conventional template for Sodalite synthesis[6]. however, recently a strong structure directing effect towards (all-silica) Sodalite formation has been recognized for trioxane as the organic species[7] as well. Although nothing can be deduced from this study concerning the gel chemistry during synthesis, observations concerning the molecular fit (templating) and pore filling ability of TMA in Sodalite can be made. The two complementary methods for studying the (dynamic) interactions of organic material with zeolites are Molecular Dynamics (MD) and solid-state NMR (deuterium, ^2H, NMR and cross-polarization magic-angle-spinning, CP-MAS, NMR).

MD techniques applied in zeolite adsorption studies have gained much interest over the

last few years. However, due to the limited computer power and the just upcoming development of MD methodologies in this field of research, simulations are normally devoted to rather small systems only[8]. To reduce the complexity and required computer time, intramolecular adsorbate dynamics are usually neglected. The typical time scale of MD calculations is of the order of 100 ps. Up until now, MD calculations have never been applied to investigate the templating effect of organic molecules used in zeolite synthesis; neither have MD studies been reported in which the zeolite lattice dynamics were taken into account.

^{2}H NMR can be conveniently used to determine the mobility of 'solid-like' material on the microsecond time scale[9,10]. As shown before, very detailed information on molecular mobility in polymers can be obtained via this technique[11,12]. Recently, the technique was also introduced in the field of zeolite research to study the rotational mobility of adsorbed species[13-19]. However, the technique has not yet been used to monitor the dynamics of organic-zeolite interactions *in situ*, i.e. after the use of a deuterated organic in a zeolite synthesis.

CP-MAS ^{13}C NMR can also be used since it independently yields additional information about molecular mobilities on the millisecond time scale[20,21]. This technique has been used by *Boxhoorn et al*[22] to study the structure and position of TPA in zeolite ZSM-5. Concerning TMA trapped in various zeolite pores and cages, *Hayashi et al*[23,24] have performed very interesting ^{13}C NMR studies. They were able to relate the observed chemical shift to the diameter of the zeolite pore in which the TMA species are occluded. Furthermore, using various line-broadening techniques, they investigated the dynamics of TMA trapped in various zeolite pores and cages. For TMA in the Sodalite ß-cage, they concluded that TMA rotates freely on the millisecond time scale.

As already mentioned, this chapter is devoted to the special case of TMA occluded in the Sodalite ß-cages. For the ^{2}H NMR experiments, Sodalite has been prepared with deuterated TMA and *in situ* measurements have been carried out. Furthermore, ^{13}C NMR methods have also been applied to study the mobility of TMA in Sodalite ß-cages. With the MD simulations, special attention will be paid to the interpretation of the NMR results and a description of the molecular fit of TMA in Sodalite ß-cages will be given. For this molecular description, it appeared to be necessary to include zeolite lattice dynamics.

IV.2. Experimental and Computational

Synthesis

Deuterated TMABr was prepared by reaction of deuterated methylbromide (*ex Merck*) with ammonia gas. For this purpose, methylbromide was dissolved in a large excess of ethanol (9.6 mmol CD$_3$Br/ml C$_2$H$_5$OH). The solution was placed in a flask which was equipped with a reflux condenser and kept cool using an ice bath. The solution was stirred while ammonium gas was bubbled through the solution for 8 hours. The resulting deuterated TMABr (N(CD$_3$)$_4$Br) precipitated from the solution as a white suspension (yield 13%). TMABr was filtered off, thoroughly washed and ion-exchanged with a slurry of Ag$_2$O in water to produce an 18% deuterated TMAOH solution in water. The purity of the product was checked with high resolution ^{13}C NMR spectroscopy (data

not shown).

Sodalite was prepared using deuterated TMAOH from a synthesis gel with molar composition: $11.1SiO_2/1Al_2O_3/1.25Na_2O/4.6TMAOH/217H_2O$. This gel was placed in an autoclave and agitated under hydrothermal conditions at 190 °C for 63 hours. X-ray powder diffraction (XRD) revealed the crystalline product to be Sodalite with a trace of zeolite Omega. Another Sodalite batch for the ^{13}C NMR measurements was prepared following the same recipe as pointed out above, but this time, protonated TMAOH (*ex Fluka*) was used. The crystalline product showed the same XRD characteristics as the Sodalite batch prepared with the deuterated organic.

The maximum amount of organic material that can be occluded in the Sodalite void space is one TMA per Si_5AlO_{12} unit (which is equivalent with one TMA per Sodalite ß-cage), thus 21 %wt. Differential Thermal Analysis (DTA) of our Sodalite samples revealed a weight loss of 18 %wt of organic material, indicating that the samples used for our NMR analyses contained occluded TMA in about 90% of the ß-cages.

For the ^{2}H NMR experiments, two NMR tubes, one containing pure deuterated TMABr as a reference and another containing Sodalite with deuterated TMABr occluded, were filled under vacuum in a *Braun MB200G-K* glove box to ensure that the material was absolutely dry. Before filling the tubes, the samples were dried overnight in the glove box under a dry nitrogen flow. The NMR tubes were subsequently sealed using a two-component epoxide resin to ensure that the cap of the tube was completely air-tight. Prior to being placed in the glove box, the samples were dried in an oven at 393 K overnight.

NMR spectroscopy

^{2}H NMR spectra were recorded at 46.06 Mhz with a *Bruker MSL300 Fourier* Transform spectrometer. The quadrupolar pulse sequence[9,10] with 5 µs, 90° pulses and pulse intervals of 30 µs was used. In all cases, the relaxation delay was 1 s, which was sufficient to eliminate saturation effects. The temperature of the sample was controlled by a *Bruker* variable temperature unit *B-VT 1000*. For temperatures below room temperature, nitrogen gas, evaporated from a dewar containing liquid nitrogen, was used. Measurements were started at high temperature, and after each temperature decrease, the samples were allowed to equilibrate for at least 20 minutes.

^{13}C NMR spectra were recorded on a *Bruker MSL300* instrument (carbon frequency 75.46 MHz). The spectra were obtained in a double bearing CP-MAS probe operating with 4 µs, 90° pulses. Other experimental parameters are specified in the figure captions. The MAS experiments were carried out with spinning rates in the range 2-5 kHz.

Molecular Dynamics

All MD simulations were performed in the NVT ensemble (constant number of particles, constant volume, constant temperature)[25] using the *Sybyl* modelling software[26] implemented on a *Silicon Graphics 4D120* computer. The model consists of a single all-silica Sodalite ß-cage with one TMA occluded. The presence of aluminum atoms in the zeolite lattice is neglected. The silicon atoms of the ß-cage are attached to terminal dummy atoms that are fixed in space to mimic the effect of the surrounding Sodalite lattice, which is not considered in the simulations. The Si-dummy bonds are regarded as Si-O bonds; this is the only way the dummy atoms enter the calculations. Total simulation times varied from 75 up to 100 ps with a constant time step length

of 1 fs (=10^{-15}s).

The TMA-Sodalite interaction parameters were obtained following *Kiselev et al*[27]. This class of parameters has proven to yield satisfactory results in earlier MD studies on diffusion and adsorption of hydrocarbons in zeolites[28]. Because only a small subsystem out of an infinite lattice is considered, electrostatics cannot be taken properly into account. Thus, neither the positive charge on the TMA cation, nor the negative charge on the zeolite lattice due to the presence of aluminum is considered. Therefor, only *Van Der Waals* atom-atom interactions between the TMA atoms and the Sodalite oxygen atoms are considered (the influence of the small silicon atoms in the zeolite lattice is assumed to be negligible and has been omitted). This approximation in the TMA-Sodalite interaction is expected to be reasonable, because it can be envisaged that the molecular mobility of TMA is mainly dominated by steric effects.

Zeolite lattice potential parameters are deduced from *ab initio* calculations on silica clusters[29] and the standard *Tripos* force field[30] was used for the intramolecular atom-atom interactions within TMA (bondlength variations are not taken into account).

A series of MD simulations was performed with an increasing level of complexity. First, the Sodalite ß-cage was kept rigid whereas TMA was allowed to move freely within in the cage. At the next level of complexity, the atoms of the Sodalite ß-cage were allowed to move freely as well. Thus in the latter case, both intramolecular TMA and zeolite lattice deformations were taken into account.

IV.3. Results and Discussion

In this section the results as obtained by MD and NMR will be discussed. The discussion starts off with the MD results because these studies represent the smallest time scale (100 ps) in which the mobility of TMA in the Sodalite ß-cage is monitored. Subsequently, the results for ^{2}H (microsecond time scale) and ^{13}C NMR (millisecond time scale) will be discussed. Initially, the approaches will be discussed separately, but at the end of this section a comparison will be made.

Molecular Dynamics (picosecond time scale)

In the first calculations, the Sodalite ß-cage is assumed rigid while TMA is flexible. In the MD calculations, TMA is considered in the non-deuterated form. No rotation of the organic is observed at room temperature. Only at elevated temperatures up to 973 K, some rotational mobility of TMA can be observed.

If the Sodalite lattice is unconstrained, however, this situation changes considerably. Figures IV.1a, b, and d display the rotation of TMA occluded in Sodalite at T=273 K, 153 K, and 123 K, respectively. The dots in these figures represent subsequent positions of one hydrogen atom of TMA at 50 fs time intervals. Thus the trajectories formed by the dots give direct information on the rotational movement of TMA occluded in the Sodalite ß-cage. From the figures, it can be deduced that the rotational movement of TMA at T=273 K is not severely hindered given the 'cloud' of positions over the simulation time. However, at temperatures lower than or equal to 123

K the rotational movement becomes hindered. For these low temperatures, two distinct orientations (Figure IV.1c) of TMA in the Sodalite ß-cage are observed. It should be noted, however, that the duration of the MD simulation is only of the order of 100 ps. Thus for longer times, say of the order of microseconds or even milliseconds, the molecular rotation may appear to be very fast. Close examination of the computational data reveals that intramolecular rotations of the CH_3 groups around the N-C bond in TMA do not occur.

The rotation of TMA in the ß-cages seems to be stimulated by the lattice deformations. At T=273 K, a spread in the average distance of two diametrically opposed oxygen atoms of 0.4 A was observed. Apparently, this fluctuation is large enough to cause a rapid rotation of TMA occluded in Sodalite. The lattice deformations are localized effects because the volume of the ß-cage was found to be nearly constant during the simulations; variations in the cage volume were only of the order of 0.5% of the total volume.

Although TMA is observed to rotate very rapidly, this does not mean that the organic can have any random orientation in the Sodalite ß-cage. Analysis of the data reveals that the TMA species 'hop' from one preferred orientation to another in the cage. The jumping frequency is directly related to the frequency at which the deformations of the Sodalite ß-cage occur. Figure IV.2 clearly visualizes this phenomenon. In this figure, the Sodalite cage and occluded TMA are displayed in the state they were in at t=1, 2, 3, ..., 70 ps. The view is perpendicular to one of the six-ring windows from which the Sodalite ß-cage is built up. Figure IV.2 allows two main observations: firstly it shows that the variance in the cage diameter is mainly caused by vibrations of zeolite oxygen atoms around their average position (Si-O-Si bond angle vibrations); the positions of the T-sites are observed to be mainly constant in time. Secondly, it shows that although the TMA species rotate very rapidly, the organics occupy only distinct symmetry-equivalent positions. This phenomenon can be explained by assuming a perfect molecular fit of TMA in the Sodalite ß-cage. In this case, TMA can only be accommodated in the ß-cage in a limited number of degenerated orientations due to steric hindrance. Because of symmetry, TMA is always in one of these orientations, but a 'hopping' between those orientations does occur.

The main conclusions to be drawn from this MD study are as follows. The distance between two diametrically opposed oxygen atoms in the ß-cage fluctuates by as much as 0.4 A around the time averaged value of 6.6 A. As no variation in the cage volume is observed, it can be concluded that this fluctuation is responsible for the rotational freedom of occluded TMA, which is further demonstrated by the total absence of TMA rotations in the rigid cage simulations. Additionally, the TMA-Sodalite interaction cannot be considered as a static 'hand in glove' system while TMA seems to be able to rotate rapidly at T=273 K. The rotational freedom of TMA occluded in the Sodalite ß-cage is significantly reduced at temperatures of 123 K or lower.

Figure IV.1
Rotational freedom of TMA occluded in the Sodalite ß-cage at T=273 K (a), T=153 K (b), and T=123 K (c). The dots in the figures display the position of one TMA hydrogen atom at 50 fs time intervals.

Figure IV.2
Various states of the Sodalite ß-cage and TMA during the MD simulation. In total, 70 states are displayed representing t=1, 2, 3, ..., 70 ps. The view is perpendicular to one of the six-ring windows from which the Sodalite ß-cage is built up.

²H NMR spectroscopy (microsecond time scale)

In first instance, solid deuterated TMABr is measured as a reference. The reference ²H NMR spectrum at 243 K consists of three components (Figure IV.3a): two axially symmetric powder patterns with a zero-asymmetry parameter and a quadrupolar splitting ($w_q/2\pi$) of 78 and 24 kHz, respectively, and an isotropic peak, which has less than 30% of the total intensity. The fact that some of the methyl groups of TMABr are mobile may be due to the presence of residual hydration water in spite of the fact that all samples had been carefully dried beforehand. The conclusion that can be drawn from the two powder patterns in Figure IV.3a is that two inequivalent, immobile sites exist for the methyl groups in TMABr as a solid, which may be due to the presence of the Br anions or hydration water, and, for comparison with the TMA species occluded in Sodalite, that more than 70% of the TMA species in the solid is immobilized on the microsecond time scale, as would be expected for a solid.

In the Sodalite ß-cage, the TMA species give rise to predominantly one isotropic peak. At 243 K this component represents more than 95% of the total spectral intensity (Figure IV.3b). At temperatures down to 153 K, the low-temperature limit of the equipment, the isotropic peak still remains the major component, but two minor powder patterns occur with $w_q/2\pi$ values of 24 and 78 Khz, having a combined intensity of 5% (Figure IV.3c). The spectra unambiguously indicate that 95% of the methyl groups of the TMA cations reorient isotropically in the Sodalite ß-cage. It is pointed out that if TMA species were in the intermediate dynamic range for ²H NMR, thus having short T_2 relaxation times, they would not contribute to the echo intensity under these conditions. In this case, because of this effect, no quantitative parameters can be obtained[31,32]. At present, however, due to the observed isotropic peak, these conditions do not apply.

Clearly, the TMA cations occluded in the Sodalite ß-cage are not immobilized by the surrounding zeolite lattice. This is a remarkable and unexpected effect. If the TMA would have been completely immobilized in Sodalite, a wideline spectrum consisting of powder pattern(s) with a non-zero symmetry parameter would have been observed. For such entirely rigid methyl groups $w_q/2\pi$ values of 165-175 kHz have been reported[33].

In order to explain the isotropic peak in the ²H NMR spectrum, both rapid rotation around the N-C bond of the CH_3 groups and fast librational motion of the N-C bond itself must be involved. In case of only one of these two motions still a wideline spectrum would have been observed, albeit that this would have been an axially symmetric powder pattern with a reduced $w_q/2\pi$ value. Therefore, the model with two types of rapid motion for the methyl groups is proposed. It corresponds to a virtually isotropic reorientation of the methyl groups of the TMA cation on the microsecond time scale.

At 153 K a small amount of the total TMA spectral intensity is reduced due to some immobility of the TMA cation. This yields a wideline spectrum consisting of two axially symmetric powder patterns similar to that observed for TMA as a solid. From this observation the offset of at least one of the two methyl group motions (rotation around the N-C bond, librational motion of the N-C bond) is concluded. This may very well be due to a decreased mobility of the surrounding O-atoms in the zeolite lattice that are part of the Sodalite ß-cage (see MD section).
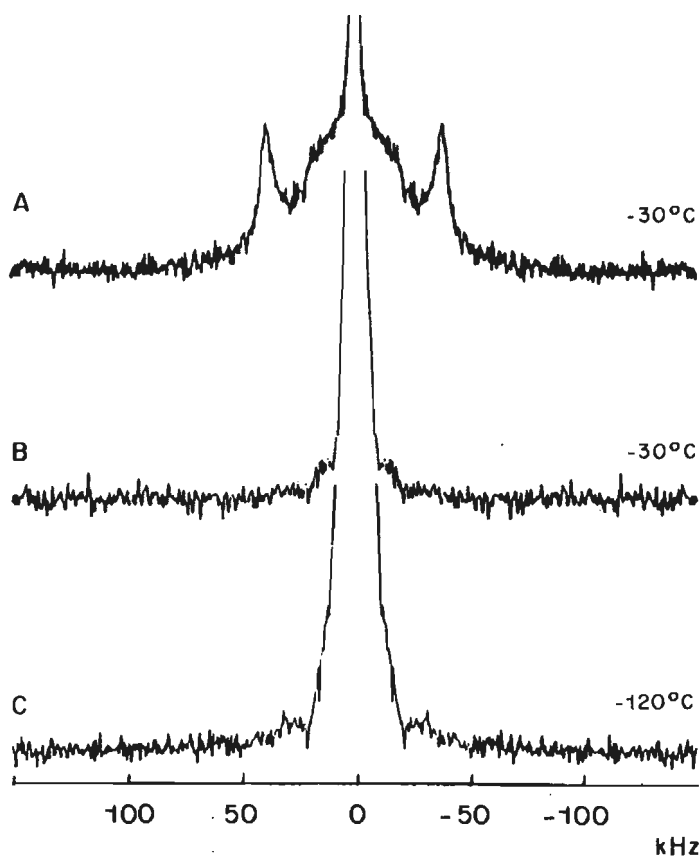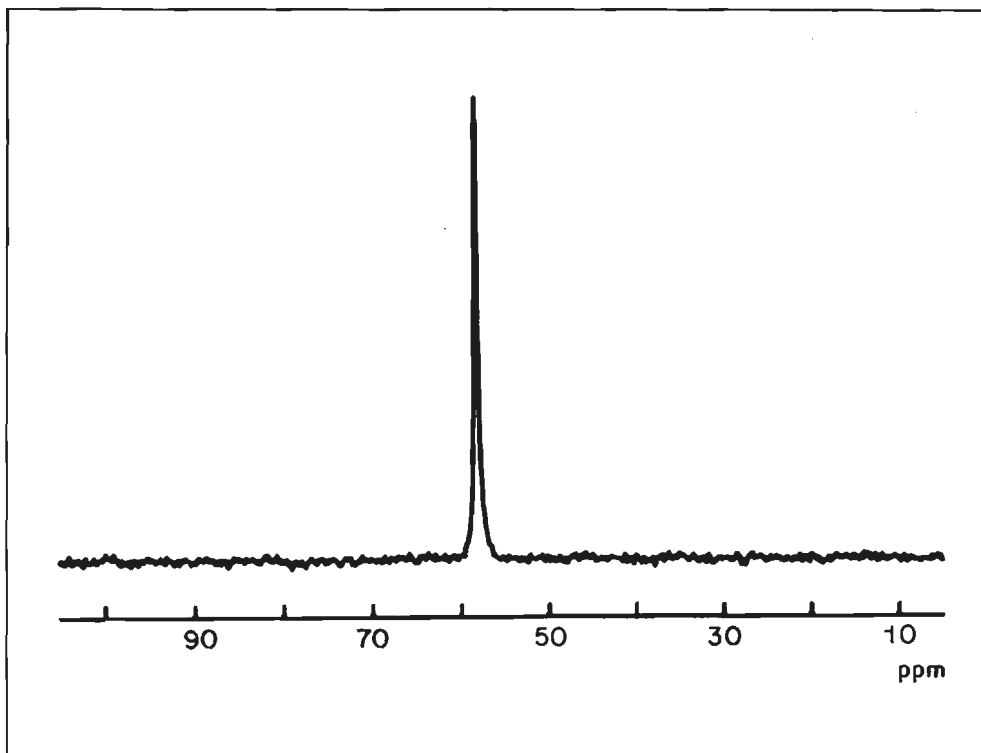
<u>Figure IV.4</u>
Room temperature 75.48 MHz high-resolution solid-state ^{13}C NMR spectrum of TMA occluded in the ß-cage of Sodalite. The width of the peak at 58.4 ppm is 32 Hz.

^{13}C NMR spectroscopy (millisecond time scale)

In addition to ^{2}H NMR, ^{13}C NMR line-narrowing experiments have been carried out to study the TMA (non-deuterated) mobility in Sodalite. Information about the TMA mobility can be obtained by determining which interactions cause the line-broadening observed in the ^{13}C spectrum.

Normally, if one wishes to obtain a well-resolved ^{13}C NMR spectrum of a solid-like sample, application of MAS and proton decoupling techniques is required[20,21]. In the resulting high resolution spectrum the peak positions contain the information of interest. For the present case of TMA in Sodalite (Figure IV.4) the methyl TMA peak is positioned at 58.4 ppm corresponding to an average pore size of 7 A for the Sodalite ß-cage, in agreement with earlier observations[23]. However, from the static ^{13}C NMR spectrum of TMA in Sodalite (Figure IV.5a) it is observed that the peak of the TMA methyl groups is already quite narrow without the application of line-narrowing techniques: 1.03 kHz. In general, the line broadening mechanisms in ^{13}C NMR spectra can be separated in mechanisms which lead to homogeneous broadening arising from molecular motion in the solid and mechanisms which lead to inhomogeneous broadening appearing as a chemical shift dispersion[34]. Even if a strong templating action is involved, an organic occluded in a zeolites cage is not entirely fixed and mobility will occur to some extent. In the case of TMA
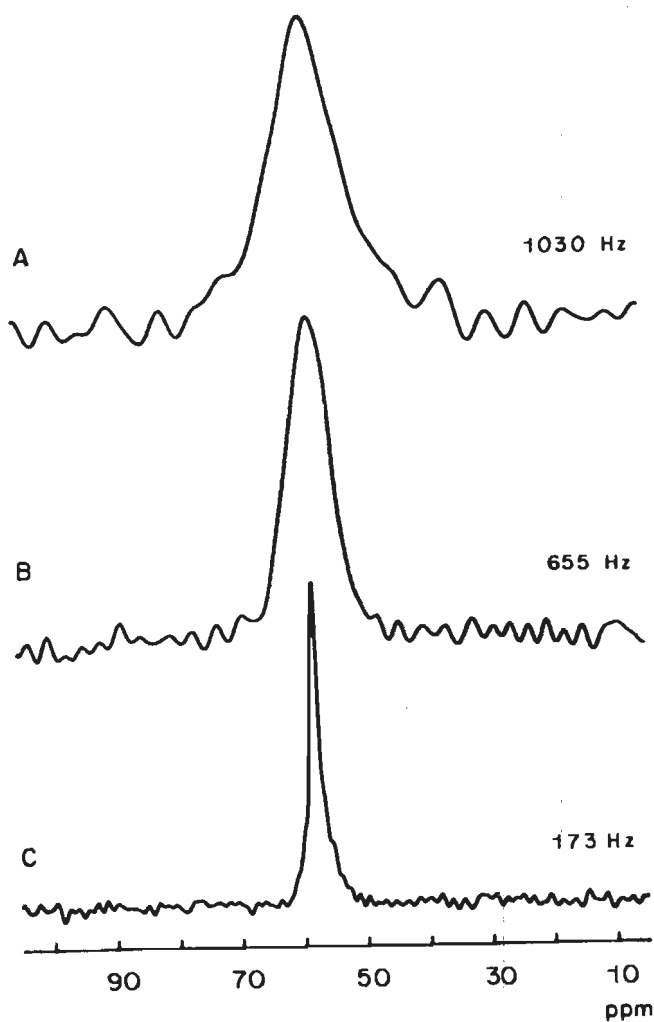
Figure IV.5

Room temperature 75.48 MHz ^{13}C NMR line-narrowing spectra of TMA in Sodalite under various conditions. a: The static spectrum, i.e. no proton decoupling and no MAS. The full width at half height is 1.03 kHz. b: The spectrum recorded with high power proton decoupling, but no MAS. The full width at half height is 633 Hz. c: The spectrum recorded with MAS, but no proton decoupling. The full width at half height is 173 Hz.

For the MAS experiments, a spinning speed of 3.04 kHz is applied. For the proton decoupling experiments, a B_1 field corresponding to a 4 μs 90° pulse is employed. The relaxation delay is 6 s and the contact time 5 ms.

in Sodalite, it provides a relaxation pathway for the ^{13}C magnetization via dipolar ^{13}C-^{14}N interaction with the ^{14}N (quadrupolar) spin[23,35] or modulates the resonance frequency via the anisotropic chemical shift[34]. The dominant inhomogeneous broadening interactions are anisotropy in the chemical shift, and scalar ^{1}H-^{13}C and dipolar ^{1}H-^{13}C coupling[36].

In the absence of any internal TMA methyl group motion in the Sodalite ß-cage the broadening due to dipolar interaction with neighboring hydrogen and nitrogen nuclei would have been about 20 kHz. Therefore, a substantial spontaneous averaging of these dipolar interactions, and the chemical shift dispersion along with it due to the same motion, is concluded.

A relatively large residual line width of the TMA peak, not yet averaged out by the internal motion, manifests itself in the presence of high-power proton decoupling; 633 Hz (Figure IV.5b). High power proton decoupling averages out all dipolar proton couplings. Consequently, the line broadening of 633 Hz is stemming from the dipolar ^{13}C-^{14}N interaction and anisotropy in the chemical shift. Therefore, since the line width in the high resolution spectrum (Figure IV.4) is only 32 Hz, a broadening of at least 601 Hz originates from these contributions. The major part of the line width is assumed to be due to strong coupling with the ^{14}N quadrupolar spin, and only a minor part is assumed to be due to the residual anisotropy in the chemical shift. The peak position in the high resolution ^{13}C NMR spectra of organics occluded in the pores of different zeolites has been correlated empirically to the pore diameters[23]. From this correlation and the calculated pore diameter fluctuation as computed in the MD simulations, it can readily be calculated that a maximum contribution of 1 ppm (=75 Hz) to the line broadening due to dispersion in the chemical shift should be observed in the static proton decoupled ^{13}C NMR spectrum (Figure IV.5b). Consequently, the remaining contribution to the total line broadening of 633 Hz can be entirely ascribed to homogeneous broadening via dipolar ^{13}C-^{14}N quadrupolar coupling. In this respect, it should be noted that the above mentioned contributions causing this line broadening are already substantially averaged out by the high TMA mobility. Therefore, the 601 Hz provides only a lower limit the dipolar ^{13}C-^{14}N coupling and the anisotropy in the chemical shift.

The 32 Hz line width observed in the high resolution spectrum (Figure IV.4) is caused by chemical shift dispersion and coupling with the ^{14}N spin. Hence, it follows that the dispersion in the chemical shift is maximally about 0.4 ppm. Using the empirical relation between chemical shift and pore diameter[23], a maximum fluctuation of 1 A in the Sodalite ß-cage diameter is measured.

Finally, it should be noted that the TMA motion in Sodalite is not entirely isotropic (i.e. *Brownian* motion as in liquids) and that some residual, anisotropic broadening (chemical shift and ^{3}C-^{14}N coupling) is left on the millisecond time scale since MAS is still capable of averaging the static line width further down to 173 Hz (Figure IV.5c). This indicates a hindered rotation of TMA in the Sodalite ß-cage, which can be envisaged as a 'hopping' motion from one orientation to another. However, the hopping frequency is very fast on the millisecond time scale.

In general, the ^{13}C NMR experiments confirm that TMA in Sodalite has a considerable motional freedom on the millisecond time scale, as expected on the basis of the ^{2}H NMR results. Spontaneous TMA motion already averages out the major part of the line broadening interactions.

Comparison of spectroscopic and computational results

From the present NMR results, it can be concluded that TMA cations occluded in Sodalite ß-cages have a considerable mobility. At least two types of TMA motion, each with its own

specific time scale, have to be invoked to account for all the data.

From ^{2}H NMR measurements it becomes clear that CH_3 rotation around the N-C bond and/or a librational motion of the N-C bond occurs on the microsecond time scale for TMA methyl groups occluded in zeolites. In contrast, MD simulations on the same system indicate that there is no rapid rotation of CH_3 groups around the N-C bond because of severe obstruction by the Sodalite ß-cage atoms. Since MD deals with a much shorter time scale (100 ps), the currently observed rotation around the N-C bond must be slow on the MD time scale but fast on the ^{2}H NMR time scale (microseconds). The librational motion of the N-C bonds in TMA is observed to be fast on the MD time scale and thus these movements are also traced with ^{2}H NMR. It is worth noting that MD predicts a freezing of librational motion of TMA at temperatures around 123 K. This temperature is in reasonable agreement with the temperature at which immobility starts to show up in the ^{2}H NMR measurements.

^{13}C NMR, too, reveals a high mobility for TMA occluded in Sodalite given the narrow peak in the static CP ^{13}C NMR spectrum (Figure IV.5a). With MD, a rather large fluctuation in the distance between two diametrically opposed oxygen atoms of the ß-cage is observed: 0.4 A. Such large fluctuations can also be deduced from the high resolution CP-MAS ^{13}C spectrum (Figure IV.4) in which a line width of 0.4 ppm is observed. This line width can be correlated with a maximum fluctuation of 1 A of the Sodalite ß-cage diameter. The agreement with the MD simulations is reasonable.

IV.4. Conclusions

An experimental and computational approach has been followed to describe and explain the dynamics of a TMA cation occluded in a ß-cage in zeolite Sodalite. Both the NMR techniques (solid state ^{2}H NMR and CP-MAS ^{13}C NMR) and the computational results from a MD simulation indicate that the TMA cation is able to perform a restricted rotational movement at temperatures above some 125 K. Moreover, internal rotations of the TMA methyl groups about the C-N axis were observed in the NMR experiments but not in the MD simulations. This might indicate that these rotations are slow on the MD time scale and fall in between the MD and ^{2}H NMR time scales.

From MD, it follows that the tumbling of TMA is stimulated by the fluctuations of the distance between two diametrically opposed oxygen atoms of the Sodalite ß-cage. Furthermore, MD simulations clearly show the four distinct and equivalent sites in the Sodalite ß-cage where the TMA CH_3 groups have the highest probability to reside. The simulations suggest that the TMA-Sodalite system is not a static one, but that TMA very rapidly 'hops' from one equilibrium orientation to another equivalent one. ^{2}H NMR reveals a larger rotational freedom of the TMA cation in the bromide salt as in the ß-cage. Clearly the interactions between the TMA cations and the zeolite are much weaker than those between TMA and the bromine ions. This observation is consistent with earlier reported inelastic neutron scattering studies[37].

The close agreement between the results obtained from well established and reliable

spectroscopic techniques and from a MD simulation indicates that computational approaches in zeolite research have gradually developed to valuable tools. These tools can be successfully applied for the interpretation and prediction of the interaction and dynamics of relatively large organic molecules in zeolites. It should be mentioned, however, that agreement with experimental (spectroscopic) results is only obtained if the dynamics of the zeolite structure is taken into account. This observation also indicates that MD simulations of the diffusivity of bulky molecules in zeolites have only little value if rigid structures are used. This point was already addressed in chapter III.

A point that finally needs to be addressed relates to the templating action of the TMA cation in the ß-cage during the formation/stabilization of zeolite Sodalite. The classical concept of a template is that of an organic molecule or cation which tightly fits within a porous zeolite ('hand in glove'). The high energy gain due to enhanced interfacial energy is supposed to be responsible for the structure directing effect of the template during the nucleation step and for the stabilizing effect on the zeolite crystals formed during the subsequent crystallization. As a result of the tight fit of the template and the intracrystalline space, a templating material is generally considered to be frozen in the zeolite.

The results of the present study show that the classical idea of templating might need some revision. Apparently, the perfect fit of a TMA entity in a ß-cage does not rule out the occurrence of rapid rotational hopping-type movements of a template. However, the (time averaged) orientation of a TMA cation is well defined.

References

1. E.M. Flanigen, Adv. Chem. Ser., 1973, 121, p. 119.
2. B.M. Lok, Zeolites, 1983, 3, p. 282.
3. G. Boxhoorn, O. Sudmeyer, P.H.G. Van Kasteren, J. Chem. Soc. Chem. Commun., 1983, p. 1416.
   E.J.J. Groenen, A.G.T.G. Kortbeek, M. Mackay, O. Sudmeyer, Zeolites, 1986, 6, p. 403.
   J.P. Van den Berg, P.C. De Jong-Versloot, J.J. Keijsper, M.F.M. Post, Stud. Surf. Sci. Catal., 1988, 37, p. 85.
   J.J. Keijsper, M.F.M. Post, ACS Symp. Ser., 1989, 398, p. 28.
4. R.M. Barrer, Stud. Surf. Sci. Catal., 1985, 24, 1.
5. R.A. Van Santen, J.J. Keijsper, G. Ooms, A.G.T.G. Kortbeek, Stud. Surf. Sci. Catal., 1986, 28, p. 169.
6. See e.g. C. Baerlocher, W.M. Meier, Helv. Chim. Acta., 1969, 52, p. 1853.
7. J.J. Keijsper, C.J.J. Den Ouden, M.F.M. Post, Stud. Surf. Sci. Catal., 1989, 43, p. 237.
8. L. Leherte, G.C. Lie, K.N. Swamy, E. Clementi, E.G. Derouane, J.M. Andre, Chem. Phys. Lett., 1988, 145(3), p. 237.
9. J.H. Davis, K.P. Jeffrey, M. Bloom, M.E. Valic, T.P. Higgs, Chem. Phys. Lett., 1976, 42, p. 390.
10. K.P. Datema, B.J.H. Van Boxtel, M.A. Hemminga, J. Magn. Reson., 1988, 77, p. 372.
    K.P. Datema, P.A. De Jager, M.A. Hemminga, J. Magn. Reson., 1989, 81, p. 599.
11. H.W. Spies, Colloid Polym. Sci., 1983, 261, p. 193.
12. H.W. Spies, Adv. Polym. Sci., 1985, 66, p. 23.
13. R. Eckman, J. Chem. Phys., 1982, 76, p. 2767.
14. I. Kustanovich, D. Fraenkel, Z. Luz, A.J. Vega, H. Zimmermann, J. Phys. Chem., 1988, 92, p. 4134.
15. A.J. Vega, Z. Lutz, Zeolites, 1988, 8, p. 19.
16. R.R. Eckman, A.J. Vega, J. Am. Chem. Soc., 1983, 105, p. 4841.
17. A.J. Vega, Z. Lutz, J. Phys. Chem., 1987, 91, p. 365.
18. Z. Lutz, A.J. Vega, J. Phys. Chem., 1987, 91, p. 374.
19. Z. Lutz, A.J. Vega, J. Phys. Chem., 1986, 90, p. 4903.
20. M. Mehring, 'Principles of High Resolution NMR in Solids', Springer Verlag, 1983, New York, USA.
21. R.R. Ernst, G. Bodenhausen, A. Wokaun, 'Principles of Nuclear Magnetic Resonance in One and Two Dimensions', Clarendon Press, 1987, Oxford, UK.
22. G. Boxhoorn, R.A. Van Santen, W.A. Van Erp, G.R. Hays, R. Huis, D. Clague, J. Chem. Soc. Chem. Commun., 1982, p. 264.
23. S. Hayashi, K. Suzuki, S. Shin, K. Hayamizu, O. Yamamoto, Chem. Phys. Lett., 1985, 113, p. 368.
24. S. Hayashi, K. Suzuki, K. Hayamizu, J. Chem. Soc. Faraday Trans., 1989, 85(9), p. 2973.
25. M.P. Allen, D.J. Tildesley, 'Computer Simulation of Liquids', 1987, Clarendon Press, Oxford, UK.
26. Sybyl Molecular Modelling Software version 5.2, 1989, Tripos Associates.
27. A.V. Kiselev, A.A. Lopatkin, A.A. Schulga, Zeolites, 1985, 5, p. 261.
28. See chapter III.
29. B.W. Van Beest, J. Verbeek, R.A. Van Santen, Catalysis Lett., 1988, 1, p. 147.
30. Sybyl Theory Manual version 5.2, 1989, Tripos Associates.
31. H.W. Spies, H. Sillesur, J. Magn. Reson., 1981, 42, p. 381.
32. A.J. Vega, Z. Lutz, J. Phys. Chem., 1987, 86, p. 1803.
33. R. Ikeda, A. Kubo, C.A. McDowell, J. Phys. Chem, 1989, 93, p. 7315.
34. D.L. Van Der Hart, W.L. Earl, A.N. Garoway, J. Magn. Reson., 1981, 44, p. 361.
35. J.G. Hexem, M.H. Frey, S.J. Opella, J. Chem. Phys., 1982, 77, p. 3847.
36. A. Abragam, 'The Principles of Nuclear Magnetism', 1961, Clarendon Press, Oxford, UK.
37. T.O. Brun, L.A. Curtiss, L.E. Itou, R. Kleb, J.M. Newsam, R.A. Beyerlein, D.E.W. Vaughan, J. Am. Chem. Soc., 1987, 109, p. 4118.

CHAPTER V

ION-EXCHANGE AND LOCATION OF NI²⁺ IONS IN SILICEOUS ZEOLITES

V.1. Introduction

It is well known that zeolites in the H-form act like solid acids, the acidity primarily depending on the aluminum content in the zeolite lattice[1] and hence they are used as components in acidic catalysts. The catalytic performance of zeolites can be modified by introducing cations via e.g. ion-exchange procedures. In particular, transition metal ions present in the micropores may act as alternative catalytic centers in reactions other than those requiring carbenium ions as intermediates[2]. In this chapter, special attention will be to ion-exchange characteristics of the siliceous polymorphs of the zeolites ZSM-5 and Mordenite.

The ion-exchange properties of ZSM-5 have been studied by various authors. *Chu* and *Dwyer*[3] measured ion-exchange isotherms for NH_4^+, H_3O^+, Cs^+, Cu^{2+}, Zn^{2+} and Ni^{2+} ions in ZSM-5. Independent of the Si/Al ratio of the various zeolites investigated, complete exchange of both univalent and divalent ions was observed. Selectivity data for a range of univalent and multivalent cations were reported showing that ZSM-5 has a marked preference for large, weakly hydrated cations (such as e.g. Cs^+). Studying the exchange properties of an Na-ZSM-5 having an Si/Al ratio of 39, *Matthews* and *Rees*[4] observed 100% exchange for univalent cations, whereas incomplete exchange was found with the divalent cations Ca^{2+} (33%), Sr^{2+} (50%), and Ba^{2+} (67%) and with the trivalent La^{3+} (33%). These results were achieved at 298 K. With increasing temperature, these values increased slightly.

The data reported by *Matthews* and *Rees*[4] show that in the highly siliceous ZSM-5, exchange of multivalent ions can be established to a limited extent only. Especially with zeolites having a low aluminum content it can be envisaged that the distribution of the aluminum ions in the zeolite framework may play a role. At high levels of aluminum dilution, the balancing of the positive charges of the multivalent cations may become difficult since with decreasing concentration of the randomly distributed negatively charged aluminum framework sites their average distance increases, which lowers the average coulombic interaction of the framework with multivalent cations.

The location, however, of divalent cations inside zeolites is still a matter of extensive debate. With high alumina zeolites, the concentration of divalent cations attainable is in general sufficiently high to allow determination of their location by standard XRD techniques[5,6]. However, in the case of siliceous zeolites, the levels of exchange are too low to allow the location of divalent cations to be determined by XRD experiments.

In order to elucidate the factors limiting the exchange capacity for multivalent ions in the siliceous zeolite ZSM-5 in more detail, the kinetics and degree of exchange of Ni^{2+} ions in ZSM-5 frameworks covering a wide range of Si/Al ratios have been measured. For comparison the degree of exchange with univalent ions (K^+ and Na^+) has been determined as well. By interpreting the results with a statistical model, in which it is assumed that Ni^{2+} is located in the ZSM-5 lattice near

an Al-O-Si-O-Al framework sequence (in the course of this chapter denoted as a NNN, Next Nearest Neighbor, -sequence), it is shown that the number of Ni^{2+} cations which can be accommodated in the zeolite is directly related to the number of NNN-sequences present in the framework.

The conclusions drawn from the Ni^{2+} ion-exchange modelling studies are strongly supported by the conclusions following from a computational model study on the location of Ni^{2+} in siliceous Mordenite. Using Lattice Energy Minimization techniques, it is shown that a combination of a Ni^{2+} ion located near an NNN-sequence is most favorable from an energetical point of view.

In section V.2, the basics of the computational methods used in this chapter will be discussed. Both the Lattice Energy Minimization technique and the statistical models used for the interpretation of the ion-exchange data will be treated. In section V.3, the computational and experimental setup is presented followed by section V.4 in which both the computational and the experimental results are presented and discussed. Finally, section V.5 closes this chapter with a summary of the main conclusions.

V.2. Computational Methods

In this section, the Lattice energy Minimization method used for the calculations on the location of Ni^{2+} ions in siliceous Mordenite is briefly discussed. Furthermore, the statistical models for the interpretation of the ion-exchange observations in siliceous ZSM-5 is presented.

V.2.1. Lattice Energy Minimization

In general, there are two approaches to the computational study on structural aspects of complex inorganic structures. One starts with the ionogenic nature of the attractive part of the chemical bonds. In addition, *Born* type repulsive interactions are introduced so that equilibrium distances can be calculated. Covalent interactions are considered as being corrections and are being accounted for by the additional introduction of *Van Der Waals* interaction terms or by explicit incorporation of polarization. The other approach has as its starting point the quantumchemical nature of the chemical bond. Approximate quantumchemical approaches used are usually limited to clusters. Only recently, practical schemes have been implemented applicable to infinite lattices. In this chapter, only attention will be paid to the first approach.

The rigid ion and shell model approaches[7] to be discussed in this section are based on the philosophy of the first approach outlined in the preceding paragraph. Bonding is assumed to be mainly ionic, so the potential used consists of a long range electrostatic term and a short range covalent one. The long range term due to Coulombic interactions is calculated using an *Ewald* summation of the electrostatic potentials due to point charges[9]. The short range potential employed is of a *Buckingham* type:

$$\Phi_{ij} = A_{ij} e^{-\frac{r_{ij}}{\tau_{ij}}} - \frac{C_{ij}}{r_{ij}^6} \qquad (V.1)$$

where r_{ij} is the distance between atom i and j and A_{ij}, C_{ij} and τ_{ij} are short range parameters. The repulsive term in equation (V.1) is of a *Born* repulsion interaction type characterized by an exponential r_{ij} dependence. The attractive term describes the *Van Der Waals* interaction between two polarizable atoms.

According to some authors[8], in studying structural features of zeolites it is essential to introduce in addition the bond-bending or three-body potential:

$$\phi(\theta) = k(\theta - \theta_0)^2 \qquad (V.2)$$

where $\Phi(\Theta)$ is the bond bending potential, Θ is the O-Si-O bondangle and Θ_0 is the tetrahedral angle. The term confers a degree of "tetrahedrality" to the SiO_4 groups.

The approximations for the potentials used so far constitute the rigid ion model. One can also include ionic polarizabilities, as is done in the shell model. According to this model the ion is thought to consist of a core and a massless shell interconnected by a spring. Usually, the spring is considered harmonic having a spring constant K. The polarization of a free ion is related to the charges and spring constant by:

$$\alpha = \frac{Y^2 e^2}{4\pi \varepsilon_0 K} \qquad (V.3)$$

where α is the ionic polarizability, e is the unit charge, Y the formal charge and ε_0 is the vaccuumpermittivity. In the shell model, the *Buckingham* potential and the bond bending three-body potential are defined between shells and not between cores.

Using these potentials, the technique of lattice energy minimization[7] is used to compute interatomic distances and angles and to predict several physical properties such as the dielectric constant and the elasticity constants. The forces on the atoms are computed and an iterative procedure is used to converge the atom positions to those positions where the energy is minimized and the forces on the atoms disappear.

Lattice energy minimization may be carried out at two levels: either the atomic positions only are adjusted until the energy minimum is found (constant volume minimization) or, in addition, the unit cell parameters are adjusted to remove any remaining strains in the lattice (constant pressure minimization). In this chapter, constant pressure calculations are performed.

An additional feature of the work presented in this chapter is that in some of the calculations the energy minimization is carried out in two stages: first, the framework of the siliceous zeolite is relaxed to its minimum energy confirmation, and then kept fixed while the extra-framework cations are adjusted to further minimize the energy.

The main difference between rigid ion and shell model calculations is that the shell model decreases the effective charges to be used in the *Ewald* summation (reduction to around 80%) and computes a frequency dependent dielectric constant. This phenomenon also causes the *Coulomb* interactions to decrease[10].

The potential parameters used in equations (V.1) and (V.2) are fitted to give good unit cell dimensions as well as elastic constants. Full formal charges are used to compute the electrostatic interactions. A more elegant and fundamental way of deriving potential parameters has been published recently by *van Beest et. al.*[11]. Using quantumchemical calculations on silica clusters, they arrived at a superb set of parameters to be used in equations (V.1) and (V.2).

V.2.2. Statistical Model for Ni²⁺ Ion-exchange

In the statistical model for the interpretation of Ni^{2+} ion-exchange observations, it is assumed that the nickel species present in the zeolite are Ni^{2+} ions which are charge balanced by two aluminum framework sites in the zeolite lattice. Furthermore it is assumed that the framework aluminum atoms are randomly distributed within the zeolite lattice. If this is the case, it is reasonable to state that the maximum amount of nickel that can be incorporated in the zeolite lattice is strongly dependent on the possibility of finding two aluminum atoms in close proximity to each other, i.e. separated by only one silicon atom in an Al-O-Si-O-Al sequence (NNN-sequence).

To support the ideas as outlined above, two statistical models have been developed. In the first one (in the course of this chapter denoted as the AN model), an analytical expression for the relationship between the molar Ni/Al ratio and the molar Si/Al ratio has been derived. The second model (denoted as the MC model) is a *Monte Carlo*-like numerical statistical procedure. The differences between these two approaches will become clear in the course of this section.

First the AN model will be focused. The calculation is performed on one unit cell which is entirely embedded in a zeolite matrix, i.e. surrounded by 26 other unit cells, in order to overcome boundary effects.

The probability, P_i, that a specific T-site labelled i (site i being either Si or Al) in a unit cell of a zeolite has a next nearest neighbor (NNN) site occupied by an aluminum atom is given by:

$$P_i = \frac{x\alpha_i}{N_{uc}-1}$$ (V.4)

where α_i is the number of different NNN T-sites of site i, x is the fraction of T-sites occupied by aluminum (x=Al/Al+Si) and N_{uc} is the total number of T-sites in the unit cell.

Equation (V.4) is valid for every T-site in the unit cell. The probability of finding an NNN site occupied by Al for *any* T-site in the unit cell is derived from equation (V.4) by summation over all T-sites in the unit cell:

$$\sum_{i=1}^{N_{uc}} P_i = \left(\frac{x}{N_{uc}-1}\right)\sum_{i=1}^{N_{uc}} \alpha_i$$ (V.5)

The number of Al-O-T-O-Al (T=Si or Al) sequences in the unit cell is now obtained by multiplying equation (V.5) by the number of aluminum atoms (N_{Al}) in the unit cell:

$$N_{Al-O-T-O-Al} = \left(\frac{xN_{Al}}{2(N_{uc}-1)}\right)\sum_{i=1}^{N_{uc}}\alpha_i \qquad (V.6)$$

The factor 1/2 is introduced to avoid double counting.

At this point, it should be noted that *Loewenstein's* rule is violated. However, when dealing with low aluminum contents, as is the case in this chapter, one can approximate $N_{Al-O-T-O-Al}$ by $N_{Al-O-Si-O-Al}$ because the probability of T also being an aluminum is almost negligible.

We stated earlier that, in our model, $N_{Al-O-Si-O-Al}$ equals the number of Ni²⁺ ions in the unit cell (N_{Ni}) and so from equation (V.6), with the approximation that for low aluminum contents $x=Al/Si$, the relationship between the Ni/Al and Si/Al ratio is readily established:

$$\frac{Ni}{Al} = \frac{N_{Ni}}{N_{Al}} = \frac{N_{Al-O-T-O-Al}}{N_{Al}} = \left(\frac{1}{2(N_{uc}-1)}\right)\left(\frac{Al}{Si}\right)\left(\sum_{i=1}^{N_{uc}}\alpha_i\right) \qquad (V.7)$$

Using $N_{uc}=96$ for ZSM-5 type zeolites and $\alpha_i=11.8$ for all values of i[12,13] and accordingly $\Sigma\alpha_i=1133$, equation (V.7) reduces to the simple form:

$$\frac{Ni}{Al} = 5.96\left(\frac{Al}{Si}\right) \qquad (V.8)$$

The analytical expression (V.8) can only be obtained if *Loewenstein's* rule is neglected and hence it can only be used in situations which deal with low aluminum contents. If one wishes to include *Loewenstein's* rule, the statistics become much more complicated. Therefore, in addition, a *Monte Carlo* procedure is employed in which *Loewenstein's* rule can be easily implemented. For this purpose, the number of NNN-sequences in a zeolite unit consisting of 3.3.3=27 unit cells has been calculated. Periodic boundary conditions have been used to overcome boundary effects. NNN connection vectors are constructed for the N_T T-sites in the unit (in the case of ZSM-5, NT equals $27N_{uc}=2592$). A connection vector C_i for a particular T-site labelled i is an M-dimensional vector with elements $c_{i,k}$ which represent the labels of the NNN's of site i: $C_i=(c_{i,1},c_{i,2},...,c_{i,M})$.

Obviously, for ZSM-5, the average dimension of C_i equals 11.8, i.e. the average number of NNN's for a ZSM-5 T-site[12,13].

The *Monte Carlo* procedure consists of generating an ensemble of N_{MC} units consisting of 27 unit cells. In each of these units, N_{Al} aluminum atoms are randomly distributed over the available T-sites in the unit. Thus generated aluminum containing units in the ensemble which violate *Loewenstein's* rule are rejected from the ensemble, reducing the number of units contributing to the calculation from N_{MC} to N_{MC}^*. Typical values for N_{MC} and N_{MC}^* lie in the order of 200,000. The total number of NNN-sequences is counted from the ensemble of units using the set of connection vectors C_i for each unit and the sites $c_{i,k}$ over which the N_{Al} aluminum atoms are randomly distributed. Let this total number be given by X. Following this procedure, the average number of NNN-sequences, $N_{Al-O-Si-O-Al}$, and thus the average number of Ni²⁺ ions, N_{Ni}, per unit of

27 zeolite unit cells is given by:

$$N_{Ni} = \frac{X}{N_{MC}^{\bullet}}$$ (V.9)

and so one finds:

$$\frac{Ni}{Al} = \frac{X}{N_{MC}^{\bullet} N_{Al}}$$ (V.10)

V.3. Computational and Experimental Setup

V.3.1. Location of Ni^{2+} Ions in Siliceous Mordenite; Lattice Energy   Minimization

In the calculations reported, all parameters were defined using a parametrization of the potential form as discussed in section V.2 fitted to properties of α-quartz. The parameters are presented in Table V.1.

Table V.1
Potential parameters for zeolite frameworks

Shell model

	q_{core}	q_{shell}	A	τ	C
Si4+	4	0			
Al3+	3	0			
O2-	0.869	-2.869			
Ni2+	-1.344	3.344			
Si...O			1283.9	0.321	10.66
Al...O			1460.3	0.299	0.00
O...O			22764.0	0.149	27.88
Ni...O			1582.5	0.288	0.00

Three-body potential for O-Si-O and O-Al-O:
$$k=2.097 \text{ eV.rad}^{-1}$$
$$\Theta_0 = 109.47°$$
Harmonic core-shell potential for
$$O: k=74.92 \text{ eV.Å}^2$$
$$Ni: k=93.70 \text{ eV.Å}^2$$

For the Mordenite structure, the structural data of *Mortier, Pluth* and *Smith*[14] are used. The positions of the symmetric extra-framework sites are derived by using data of *Mortier et. al.*[15,16]. Information and relative coordinates of both the Mordenite lattice and extra-framework sites,

together with the nomenclature used in this chapter, are given in Table V.2.

Relative stabilities of the all-silica and Ni-alumino-silicate Mordenites (unit cell composition $Si_{48}O_{96}$ and $NiSi_{46}Al_2O_{96}$, respectively) were calculated using the Lattice Energy Minimization procedure as described in a preceding section. All calculations are performed at constant pressure using the shell model.

V.3.2. Ni²⁺ Ion-Exchange in Siliceous ZSM-5

The ZSM-5 zeolites were synthesized following a standard recipe[17]. Tetrapropylammonium bromide was used as the templating agent. The samples were prepared under hydrothermal conditions (stirred at 170 °C for 3 days) in a mixture with the molar composition 40 SiO_2/ x Al_2O_3/2.5 Na_2O/5 TPABr/1000 H_2O. Upon completion of the synthesis, the organic template was removed by careful calcination in air at 500 °C. For all samples, the crystallinity was about 100%. Part of Table V.3 represents synthesis conditions and information about products.

Table V.2
Information on the Mordenite structure used.

Space group: C_mC_m (no. 63)
Lattice parameters: a=18.65 Å, b=20.45 Å, c=7.66 Å; α=ß=τ=90°.
Lattice Energy of relaxed all-silica structure: -12392.9 kJ/mol SiO_2.

Relative coordiantes of extra-framework sites

Site	x	y	z	multiplicity
I.1	0.0000	0.5000	0.0000	4
II.1	0.0000	0.1825	0.7500	4
III.1	0.1606	0.0000	0.7906	16
IV.1	0.0000	0.0000	0.0000	4

The calcined samples were transformed into the ammonium form by exchange with a 1M NH_4NO_3 solution. The samples thus obtained were exchanged with 1M $Ni(NO_3)_2$ and 1M KNO_3 solutions. All exchange experiments reported in this chapter were carried out at 90 °C. The chemical composition of the products thus obtained was determined by
means of Atomic Absorption Spectroscopy and X-ray Fluorescence following standard procedures

V.4. Results and Discussion

Just as section V.3, this section is also split up into two subsections. First, the lattice energy minimization calculations on the location of Ni²⁺ ions in siliceous Mordenite are presented. Finally, the studies on Ni²⁺ ion-exchange in ZSM-5 will be discussed.

Table V.3

Composition of synthesis mixtures and characteristics of ZSM-5 products and ion-exchanged samples

Synthesis mixture			Products		Exchanged samples	
No.	x	Si/Al	Si/Al	Cryst. (%)	K/Al	Ni/Al
1	1.00	20	23	90	0.78	0.24
2	0.50	40	32	100	0.81	0.19
3	0.25	80	50	100	0.76	0.11
4	0.10	200	158	100	0.80	-
5	0.05	400	213	100	-	0.03

V.4.1. Location of Ni^{2+} in Siliceous Mordenite; Lattice Energy   Minimization

In general, two types of localization can be distinguished. Firstly the Ni^{2+} ions can occupy well defined extra-framework sites[15,16] within the Mordenite lattice. The preference of Ni^{2+} ions for occupation of these sites can be thought of as stemming from favorable electrostatic interactions of the ions with the local framework structure around these sites. Secondly, it is possible that the location of Ni^{2+} ions is related to the distribution and siting of aluminum[18].

In this section, both the above mentioned possibilities for the case of Ni^{2+} in siliceous Mordenite will be investigated.

Structural Effects

Lattice Energy Minimization calculations were performed on Mordenite containing two aluminum ions and one Ni^{2+} ion as charge compensating cation per unit cell (Si/Al=23). In order to study structural effects only, the aluminum ions were not placed at specific Mordenite framework sites, but the resulting negative charge was smeared out over all T-sites.

A Ni^{2+} ion was initially placed at the extra-framework sites I.1, II.1, III.1 and IV.1. The ion was allowed to relax to its minimum energy position while the mordenite lattice was kept fixed

Table V.4

Shell model calculations on Mordenite containing one Ni^{2+} ions/unit cell:$NiT_{48}O_{96}$

Initial				Final			
Ni position[*]			Latt. E[**] (kJ/mol TO_2)	Ni position[*]			Latt. E[**] (kJ/mol TO_2)
x	y	z		x	y	z	
.0000	.5000	.0000	180.6	-.0054	.5786	-.2356	180.3
.0000	.1825	.7500	202.3	.4954	.0777	.6538	180.3
.1606	.0000	.7906	181.9	.1363	-.0064	.9317	181.4
.0000	.0000	.0000	182.9	-.0054	.1779	.2784	180.6

[*] Relative to a=18.65; b=20.45; c=7.66.
[**] Relative to the lattice energy of the all-silica structure (-12392.9 kJ/mol TO_2).

The charges are smeared out over the T-sites: q_T=3.9583.

at its minimum energy configuration, which followed from an energy minimization on the all-silica structure (see Table V.2). The results of these four calculations are presented in Table V.4.

From Table V.4 it can be seen that the Ni^{2+} ion has to be moved over a considerable distance before reaching a minimum. Starting from the four extra-framework sites, four different positions for the minimum are found corresponding to four different energies. This, as a matter of fact, indicates that the global energy minimum has not been found. However, Table V.4 shows that the relative lattice energies corresponding to the four final Ni^{2+} positions are all very similar, thus it can be envisaged that the potential energy surface is very flat, which makes it likely that, for these low Al/Si ratios, there is no preferential location of Ni^{2+} at extra-framework sites.

Al-O-(Si-O)ₙ-Al Sequence Effects

As became obvious in the preceding section, no convincing evidence for siting of Ni^{2+} cations at specific ion exchange sites in the Mordenite framework emerged from the calculations. In this section, various $Al-O-(Si-O)_N-Al$ (N>0 to obey *Loewenstein's* rule) sequences occurring in the zeolite framework will be focused. As will be shown, siting of Ni^{2+} ions can be directly related to the presence of specific $Al-O-(Si-O)_N-Al$ sequences.

In general, three different environments for Ni^{2+} ions can be defined in the Mordenite framework: the 12-ring main channel, the 8-ring channel (secondary pore, parallel to the main channel) and the 8-ring side pockets of the main channels.

Ni^{2+} ions were placed in each of these locations in turn, combined with a specific $Al-O-(Si-O)_N-Al$ sequence in the zeolite framework. The particular choice of locating the aluminum atoms at specific T-sites in the three types of environment mentioned above is somewhat arbitrary, but it is assumed that the specific location of pairs of aluminum in a given environment will have only a secondary effect. The Ni^{2+} ion was allowed to relax to its minimum energy position, while the zeolite lattice was kept fixed at its all-silica minimum energy configuration (see Table V.2). In these calculations the Al-Al interaction is explicitly taken into account.

Table V.5 represents the results obtained for Ni^{2+} ions in the three different locations combined with several $Al-O-(Si-O)_N-Al$ sequences.

Ni^{2+} in the 12-ring (main channel):

The first section of Table V.5 displays relative lattice energies for Ni^{2+} located in the 12-ring main channel in combination with several sequences (N=1-4) in the ring. Energies are calculated per mole TO_2 (T=tetrahedral lattice site occupied by either Si or Al) or per 1/48 mole $NiSi_{46}Al_2O_{96}$, and are given relative to the lattice energy of the relaxed all-silica Mordenite framework. Figure V.1 displays the aluminum positions chosen to obtain the various sequences.

It is obvious that Ni^{2+} is most strongly coordinated to the Mordenite lattice when it is in the neighborhood of a sequence with N=1. The energy gap observed when going from N=1 to N=2 is striking: $\delta=5.0$ kJ/mol. This energy gap is much less pronounced when going from N=2 to N=3: $\delta=1.5$ kJ/mol. An interesting feature appears for N>3. Apart from a large energy gap between the sequences with N=3 and N=4, it can be seen that sequences with N>3 are not able to coordinate Ni^{2+} ions to the Mordenite lattice (no energy minima could be found).

In conclusion, on can say that Ni^{2+} located in the 12-ring main channel of Mordenite is preferentially coordinated to an Al-O-Si-O-Al (NNN) sequence (the aluminum atoms under
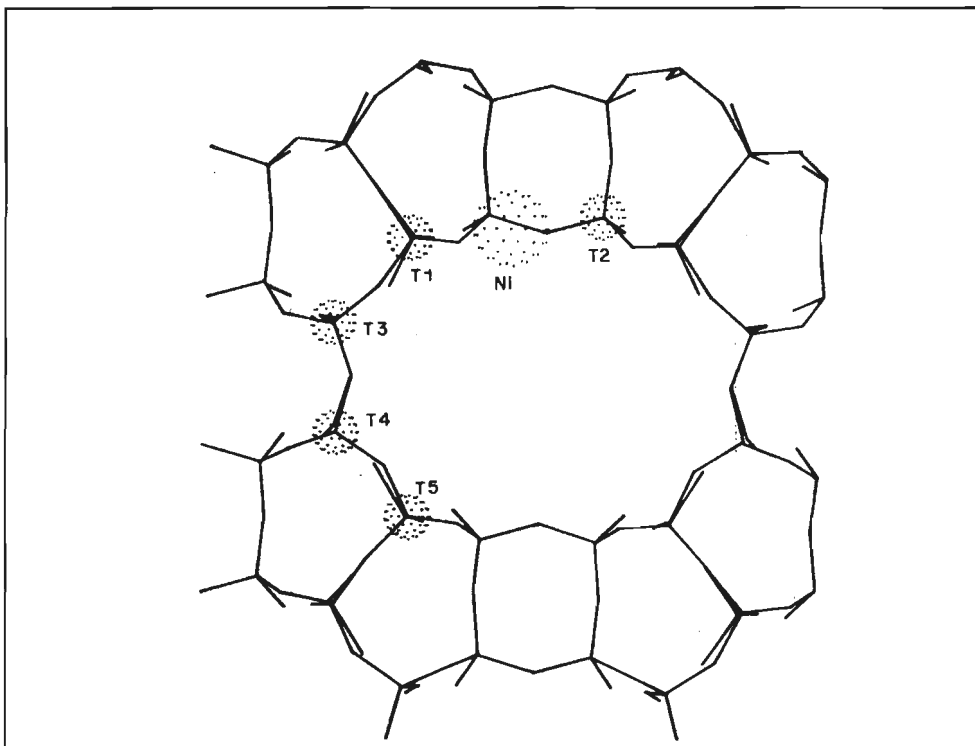
Figure V.1
Positions of the aluminum atoms which form the various Al-O-(Si-O)$_N$-Al sequences in the 12-ring main channel. N=1:T1-T2; N=2: T2-T3; N=3:T2-T4; N=4:T2-T5.

consideration labelled 1 and 2 in Figure V.1) in the 12-ring. The corresponding position of the Ni^{2+} ion is also displayed in Figure V.1. Furthermore, Al-O-(Si-O)$_N$-Al sequences with N>3 are not able to coordinate Ni^{2+} to the Mordenite lattice.

Ni^{2+} in the 8-ring (secondary pore):

The calculated results for Ni^{2+} located in the 8-ring are given in the second section of Table V.5. The aluminum positions chosen to obtain the sequences are displayed in Figure V.2. From the second section of Table V.5, it is clearly seen that the energy gaps between the different sequences in the 8-ring are much less pronounced. Again, the sequence with N=1 provides the strongest coordination of Ni^{2+} to the Mordenite framework. It should be noted, however, that coordination of Ni^{2+} in the 8-ring is favored over coordination in the 12-ring by an amount of 0.3 kJ/mol. Furthermore, coordination of Ni^{2+} to a sequence with N=2 in the 8-ring is only 0.1 kJ/mole less favorable than coordination to a sequence with N=1 in the 12-ring. The position of the Ni^{2+} ion corresponding to the 8-ring Al-O-Si-O-Al sequence (the aluminum atoms for this sequence are labelled 6 and 7) is also displayed in figure V.2.

Summarizing these results, we may conclude that Ni^{2+} is more strongly coordinated to the Mordenite lattice in the 8-ring secondary pore than in the 8-ring main channel. The differences between several Al-O-(Si-O)$_N$-Al sequences are less pronounced, which might be due to the fact

Table V.5

Shell model calculations on mordenite containing one Ni^{2+} ion/unit cell:
$Ni\ Al_2Si_{46}$. The lattice is fixed; the Ni^{2+} is allowed to relax.
Relative lattice energy of the all silica structure: -12392.9 kJ/mol SiO_2.
All lattice energies in this table are relative to the all silica structure

Section 1: Al-O-(Si-O)$_N$-Al sequences in the 12-membered ring (main channel) (Figure 1)

N	Al on T site	Position of framework Al x/a	y/b	z/c	Al-Al dist.	Equilibrium position of Ni^{2+} x/a	y/b	z/c	Relative lattice energy (kJ/mol TO$_2$)*
1	T1	0.2967	0.6910	0.5883		0.4461	0.6928	0.6880	137.8
	T2	0.5821	0.7214	0.2915	5.63				Δ = 5.0
2	T3	0.1886	0.5788	0.4991		0.5116	0.6620	0.5725	142.8
	T2	0.5821	0.7214	0.2915	7.80				Δ = 1.5
3	T4	0.1840	0.4304	0.5862		0.5161	0.6540	0.5606	144.3
	T2	0.5821	0.7214	0.2915	9.52				Δ = 7.4
4	T5	0.2953	0.3143	0.4964		no minimum found			ca. 151.7
	T2	0.5821	0.7214	0.2915	9.81				

Section 2: Al-O-(Si-O)$_N$-Al sequences in the 8-membered ring (secondary channel) (Figure 2)

N	Al on T site	Position of framework Al x/a	y/b	z/c	Al-Al dist.	Equilibrium position of Ni^{2+} x/a	y/b	z/c	Relative lattice energy (kJ/mole TO$_2$)
1	T6	0.1886	0.5788	0.4991		0.0716	0.5099	0.3818	137.5
	T7	0.0753	0.3816	0.2911	4.73				Δ = 0.4
2	T8	0.0785	0.6236	0.7934		0.0311	0.5078	0.5621	137.9
	T7	0.0753	0.3816	0.2911	6.14				Δ = 1.0
3	T9	0.9106	0.6233	0.7934		0.0216	0.5203	0.5681	138.9
	T7	0.0753	0.3816	0.2911	7.80				

Section 3: Al-O-(Si-O)$_N$-Al sequence in the 8-membered ring (side pocket) (Figure 3)

N	Al on T site	x/a	y/b	z/c	Al-Al dist.	x/a	y/b	z/c	
1	T10	0.6907	0.6901	0.9988		0.5556	0.6995	0.0260	136.7
	T2	0.5821	0.7214	0.2915	5.67				Δ = 3.3
2	T11	0.2953	0.6951	0.9992		0.5033	0.6850	0.6114	140.0
	T2	0.5821	0.7214	0.2915	7.40				Δ = 1.7
3	T11	0.2953	0.6951	0.9992		0.4373	0.6831	0.8705	141.7
	T12	0.6907	0.6901	0.5881	7.75				

* Relative to the lattice energy of the all SiO_2 structure
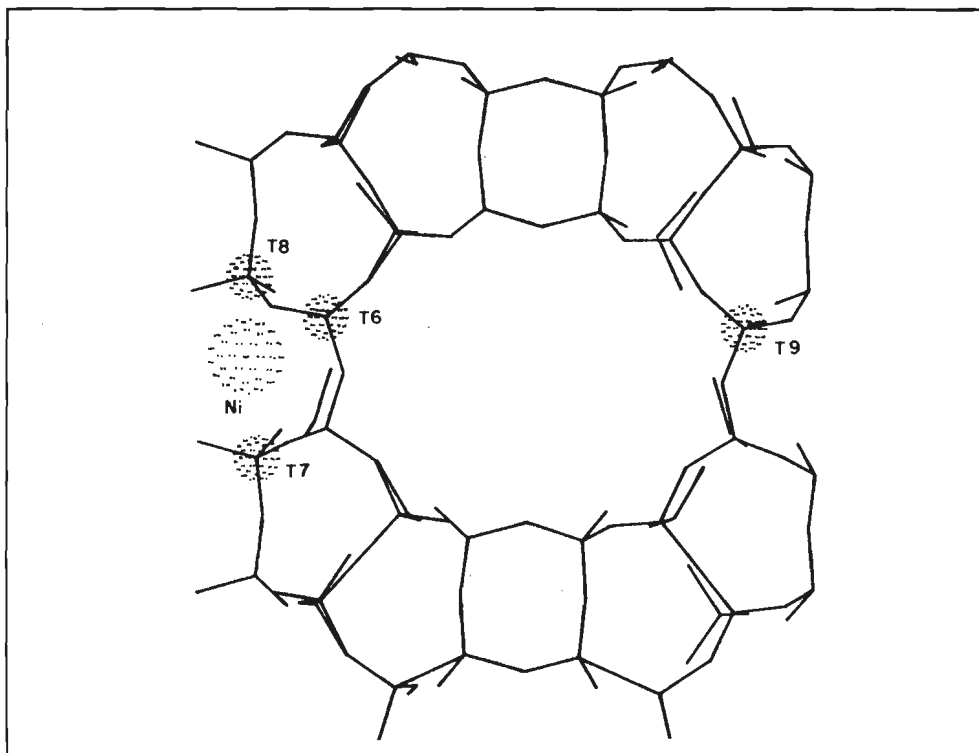
Figure V.2
Positions of the aluminum atoms which form the various Al-O-(Si-O)$_N$-Al sequences in the 8-ring channel (secondary pore). N=1: T6-T7; N=2: T7-T8; N=3: T7-T9.

that the Al-Al distances in the various sequences in the 8-ring are relatively small compared to the Al-Al distances in the 12-ring (see also Table V.5). This feature will gain more attention in a subsequent section.

Ni²⁺ in the 8-ring side pocket:

Results for Ni²⁺ located in the 8-ring side pocket are represented in the third section of Table V.5. The positions for the aluminum atoms in the various sequences are displayed in Figure V.3. Location of Ni²⁺ in a side pocket combined with an N=1 sequence (the aluminum atoms for this sequence are labelled 2 and 10 for this sequence) turns out to be the most stable configuration of the configurations considered in this section. Also in this case, increasing the value of N in the sequences very rapidly leads to less favorable configurations. The corresponding Ni²⁺ position is represented in Figure V.3.

V.4.2 Ni2+ Ion-Exchange in Siliceous ZSM-5

In this section, the results of the ion-exchange experiments and infra-red spectroscopy experiments on Ni²⁺ exchanged ZSM-5 samples will be discussed. Furthermore, some attention will be paid to the kinetics of ion-exchange. The results will be interpreted with the statistical models
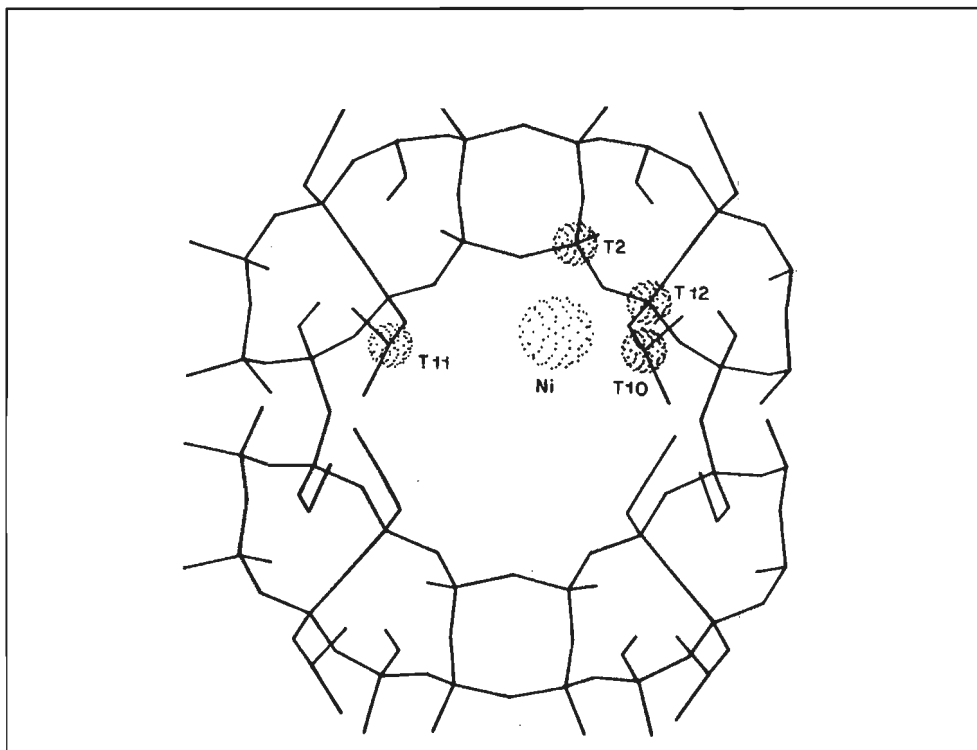
Figure V.3
Positions of the aluminum atoms which form the various Al-O-(Si-O)$_N$-Al sequences in the 8-ring side pocket. N=1: T2-T10; N=2: T2-T11; N=3: T11-T12.

as presented in a preceding section.

Exchange Experiments

In a first series of experiments the rate of exchange of Ni^{2+} ions from a solution for ammonium ions in the zeolite (the sample under consideration in these studies has a Si/Al ratio of 23; sample 1 from Table V.1) has been investigated (Figure V.4).

With increasing exchange time, the rate of Ni^{2+} exchange decreased and was virtually zero after 48 hrs., suggesting that equilibrium had been achieved within this time period. It is evident that prolonging the exchange time up to 100 hrs does not lead to higher nickel loadings. Whereas complete exchange would yield a Ni/Al molar ratio of 0.5, our experiments indicate that the maximum ratio obtained is about 0.24. Further experiments with the NH$_4$-ZSM-5 sample showed the rate of exchange to depend on the nature of the entering cation: compared to exchange with Ni^{2+} ions into NH$_4$-ZSM-5, exchange with K$^+$ ions was found to be complete within 1 hr, indicating a much higher rate of exchange (*cf.* Figure V.4). In earlier studies, it has also been recognized that the degree of exchange not only depends on the amount of aluminum in the framework but may also be influenced by the nature of the incoming cation[19].

In order to elucidate the factors limiting the exchange capacity for multivalent ions in siliceous zeolite ZSM-5, the degree of exchange of Ni^{2+} in NH$_4$-ZSM-5 frameworks covering a
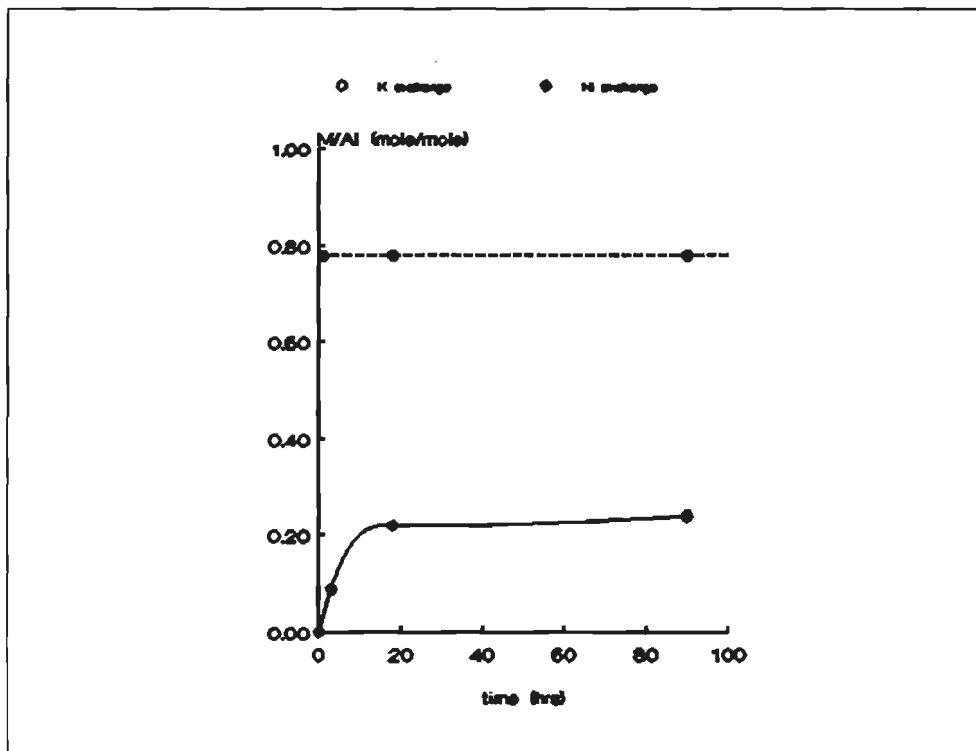
<u>*Figure V.4*</u>
M/Al ratio (M=K or Ni) for K and Ni ion-exchange from a solution for NH4+ ions in zeolite ZSM-5 (Si/Al=23) versus exchange time.

wide range of Si/Al ratios was measured. For comparison, the degree of exchange with the univalent K^+ ion was determined as well. In Table V.1 and Figure V.5 the Ni/Al ratio (after exchange for 48 hrs) and K/Al ratio (after exchange of 1 hr) are given for the NH_4-ZSM-5 samples differing in Si/Al ratio. Whereas the K/Al ratio is independent of the aluminum content, the Ni/Al ratio strongly decreases with increasing Si/Al ratio. Thus, exchange of monovalent ions is virtually complete and independent of the aluminum concentration, whereas the exchange with the divalent Ni^{2+} ion is incomplete. Exchanging an NH_4-ZSM-5 sample (Si/Al=23) with an 1M $NaNO_3$ solution also leads to complete exchange, i.e. the Na/Al ratio of the final Na-ZSM-5 is almost unity.

Infrared Spectroscopy

Infrared spectroscopy provides evidence that the Ni^{2+}, Na^+ and K^+ ions are introduced at ion exchange positions only. Table V.6 gives the intensities of the hydroxyl band at about 3600 cm⁻¹ for Ni,NH_4-ZSM-5, K,NH_4-ZSM-5 and Na,NH_4-ZSM-5 and, for comparison the starting NH_4-ZSM-5 sample (Si/Al=23). This latter sample is taken as a reference: I_0=0.518.

Whereas the hydroxyl band in the case of K- and Na-ZSM-5 has almost completely disappeared, the hydroxyl band for the nickel exchanged sample is still present. The metal over aluminum ratios for the various samples are calculated via:

The decrease in intensity of the 3600 cm⁻¹ bands observed with the K-, Na- and the
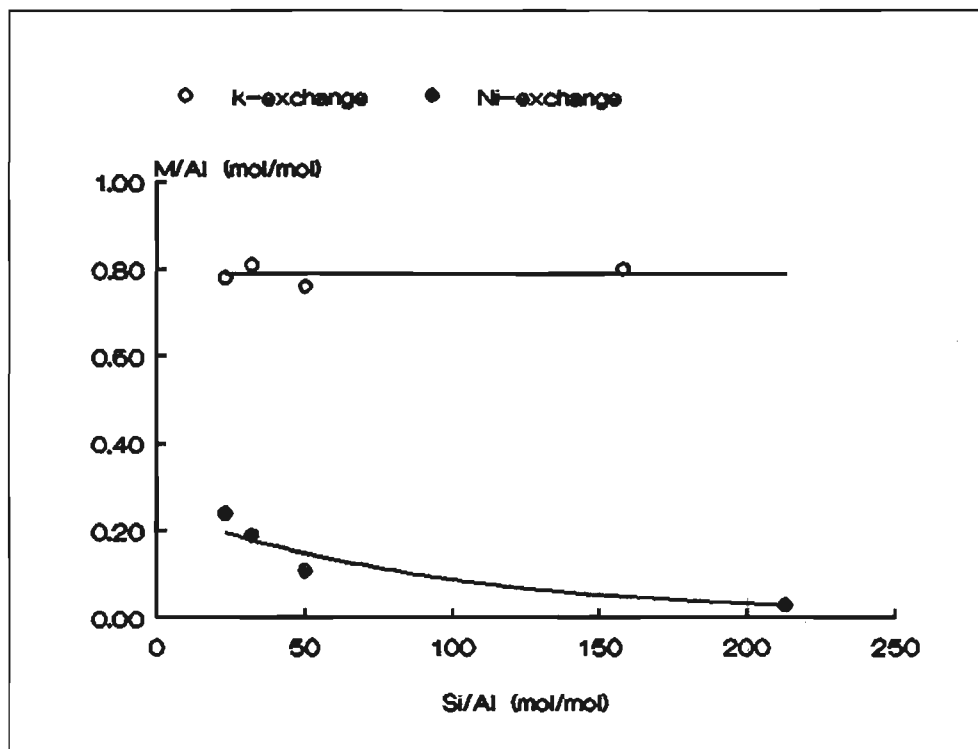
Figure V.5
M/Al ratio versus zeolitic Si/Al ratio for K^+ and Ni^{2+} exchange in NH_4^+-ZSM-5.

Table V.6
Intensities of the hydroxyl band at 3600 cm^{-1} for various ZSM-5 samples (Si/Al=23). The starting material, NH_4-ZSM-5 is taken as a reference.

Sample	I	/I_0	M^{n+}/Al
NH_4-ZSM-5	0.518	1.000	0.0
Ni,NH_4-ZSM-5	0.207	0.400	0.3
K,NH_4-ZSM-5	0.000	0.000	1.0
Na,NH_4-ZSM-5	0.000	0.000	1.0

$$\frac{M^{n+}}{Al} = \frac{1 - \frac{I}{I_0}}{n} \qquad\qquad (V.11)$$

Ni,NH_4-ZSM-5 agrees with the amount of K^+, Na^+ and Ni^{2+} introduced in these samples (*c.f.* Table V.1), indicating that these ions are indeed present at ion exchange positions.

Computational Section

Before interpreting the observed limited ion exchange capacity as discussed in the

preceding section with the statistical models, we will first focus on the identification and the number of possible extra-framework positions of Ni^{2+} in zeolite ZSM-5.

Studying the position of nickel ions in ZSM-5 with a relatively high aluminum content (Si/Al=15), *Zhenya et. al.*[20] claimed to have found evidence of two different cation positions for Ni^{2+} ions. Since per unit cell these two positions exist at four equivalent locations as required by symmetry considerations, each unit cell may accommodate eight cations.

In an attempt to identify the nature of the extra-framework sites for Fe^{2+} cations in ZSM-5, *Matthews and Rees*[4] employed *Moessbauer* spectroscopy. In agreement with data published by others they observed at least three sites, and probably even four.

All our nickel exchanged samples exhibited XRD powder diffractograms similar to that of NH_4-ZSM-5. If the nickel ions were indeed located at specific extra-framework sites, it would still be questionable whether such a small amount of Ni^{2+} ions could be detected by standard XRD techniques. Alternatively, this result can be explained by assuming that the Ni^{2+} ions are not located in preferred sites. That is, they are randomly distributed.

In our ZSM-5 sample with the highest amount of aluminum (Si/Al=23), on average about five aluminum atoms per unit cell are present. This in turn implies that in this particular zeolite at most 2.5 Ni^{2+} ions can be accommodated in the unit cell. All investigators agree that between four
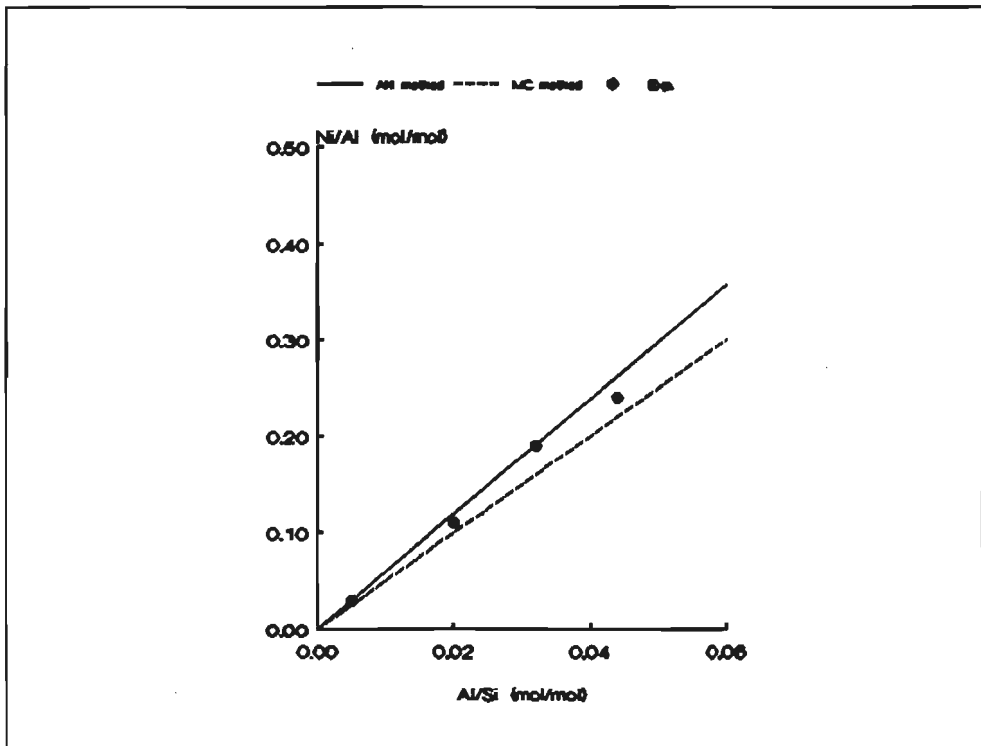

Figure V.6
Ni/Al molar ratio versus Al/Si molar ratio according to the Monte Carlo (MC) and the analytical (AN) procedure. Experimental values are given by the solid dots.

and eight extra-framework positions per unit cell are maximally present in ZSM-5. However, in this ZSM-5 sample (Si/Al=23), only 1.2 Ni^{2+} ions are present per unit cell. If the Ni^{2+} ions were indeed located at specific extra-framework sites, only a small amount of the possible cation positions would be occupied. Since the Ni/Al ratio strongly decreases with decreasing aluminum content in the lattice, it seems likely that at low aluminum concentrations the distribution and location of the aluminum ions in the framework is the factor which governs the extent of exchange with multivalent cations.

Figure V.6 displays the Ni/Al ratio according to the Monte Carlo (MC) and the analytical (AN) method. The slight differences in the slopes of the relations emerging from the MC and the AN procedure stems from neglecting *Loewenstein's* rule in the AN approach. Obviously, this difference increases with increasing aluminum content resulting in a lower Ni/Al prediction by the MC method.

It should be noted that both methods predict Ni/Al ratios which are too high for high aluminum contents (this feature is not displayed in the figure, but *e.g.* for Si/Al=1, the AN model predicts Ni/Al=5.96). This stems from the fact that in both methods *e.g.* sequences as Al-O-Si-O-Al-O-Si-O-Al are regarded as two NNN-sequences and hence are equivalent with the accommodation of two Ni^{2+} ions instead of 1.5. However, when dealing with low aluminum contents, as is the case in this paper, these double counting effects will not significantly influence the results. Also represented in Figure V.6 are the experimental exchange results. These values agree very well with the calculated ones. The slight deviation of the experimental data from the calculated relations might be due to a slight preferential siting of framework aluminum at one or more of the 12 symmetry-equivalent T-sites in the ZSM-5 unit cell. Furthermore, it is stressed that only NNN-sequences in the models are considered. The good agreement between experiment and modelling results indicates that there is almost no contribution from Al-O-(Si-O)$_N$-Al sequences with N>1.

V.5. Conclusions

In this chapter, it is shown that, according to our lattice energy minimization calculations, the existence of specific extra-framework sites for Ni^{2+} in siliceous Mordenite is doubtful. This conclusion is based on two observations.

Firstly, the small differences in the relative lattice energies for Ni^{2+} located at the four different extra-framework sites indicate hardly any preferences on structural grounds. Secondly, the relative lattice energies of the Ni-alumina Mordenites are observed to depend on the existence of specific Al-O-(Si-O)$_N$-Al sequences in combination with a Ni^{2+} ion in close proximity (compare relative lattice energies in Tables V.4 and V.5). In particular NNN-sequences (N=1) turned out to be very stable in comparison to sequences with N>1.

Not only the value of N, but also the specific location of the Al-O-(Si-O)$_N$-Al sequences in the mordenite structure proves to be important. In the case N=1, the calculations clearly indicate that Ni^{2+} is preferentially located in the 8-ring side pocket, followed by location in the 8-ring
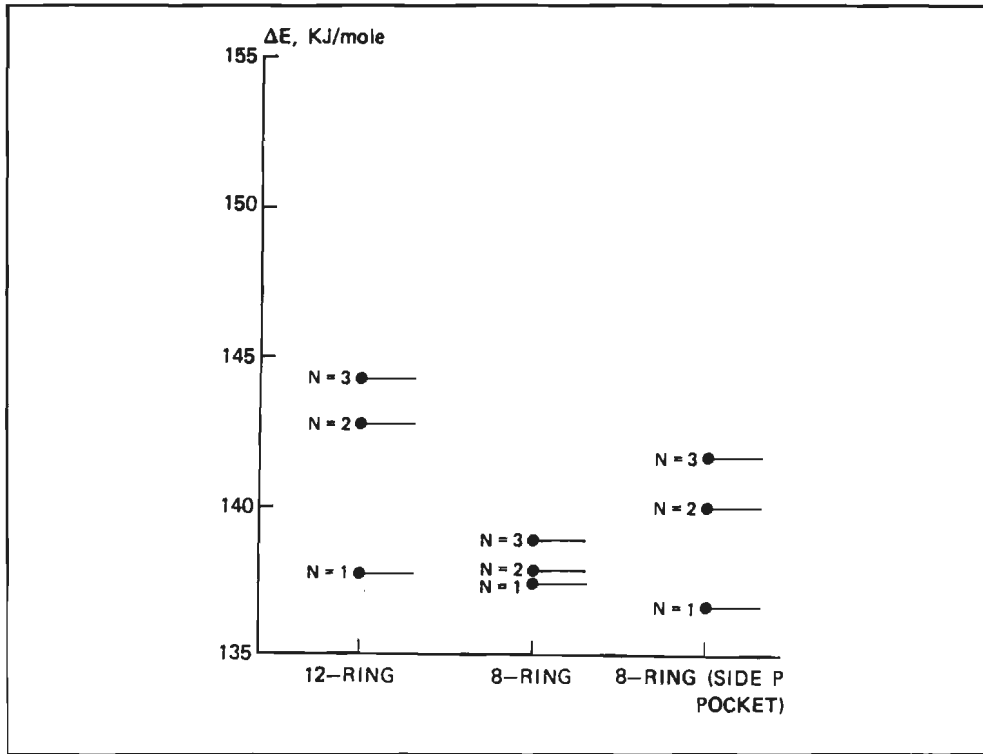
<u>Figure V.7</u>
Framework stability as a function of the location of the Ni²⁺ ion and the framework Al-O-(Si-O)$_N$-Al sequence.

secondary pore system. Location of Ni²⁺ in the 12-ring main channel proves to be less favorable. These findings are summarized in Figure V.7.

It is noted that the choice of particular Al-O-(Si-O)$_N$-Al sequences studied in this chapter is quite arbitrary. However, apart from N-values for the various zeolite framework sequences, the Al-Al distances in the sequences also play an important role, allowing us to regard the sequences chosen as general representatives of sequences anywhere in the lattice. In particular in the case of Ni²⁺ located in the Mordenite 8-ring secondary channel, this Al-Al distance effect is clear. The fairly high stability of Ni²⁺ ions which are coordinated to Al-O-(Si-O)$_N$-Al sequences (N=2, 3) in the Mordenite 8-ring channel with respect to coordination to similar sequences in the 12-ring main pore system or the 8-ring side pocket are obviously (partly) related to Al-Al distances, as displayed in Figure V.8.

The conclusions following from the lattice energy minimization calculations are fully compatible with observations from the Ni²⁺ ion-exchange experiments. With these experiments, it is shown that the degree of exchange of Ni²⁺ ions decreases markedly with decreasing aluminum content. Kinetic factors showed up clearly in comparing exchange rates for K⁺ and Ni²⁺ in NH₄-ZSM-5.

The agreement between the statistical models and experimental observations strongly supports the idea that Ni²⁺ is coordinated to Al-O-Si-O-Al (N=1) sequences in siliceous ZSM-5.
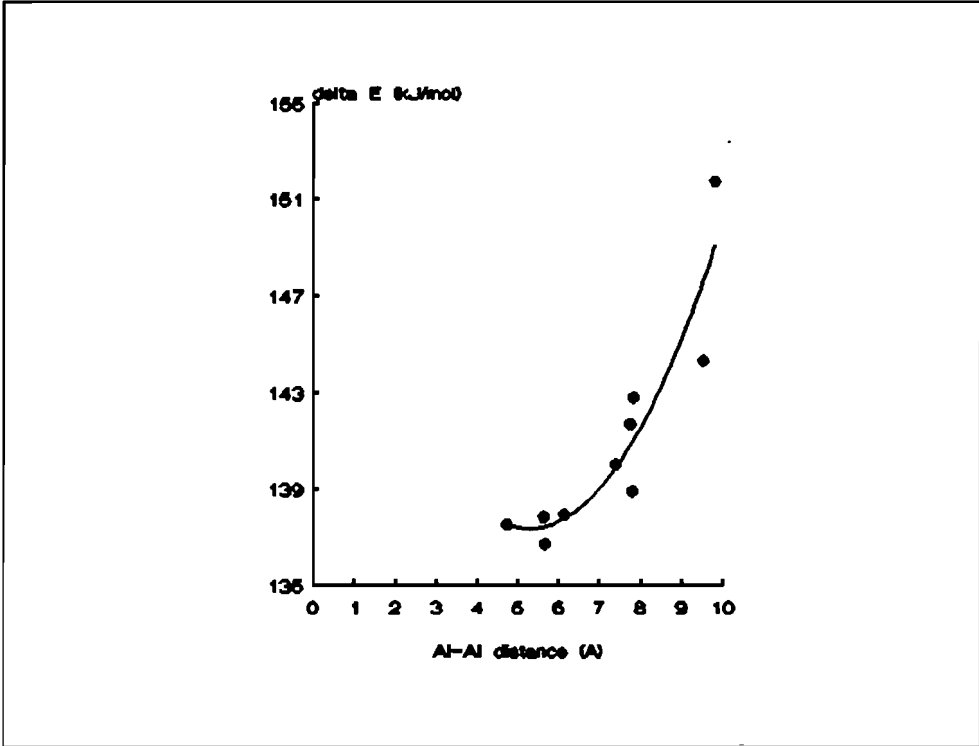
Figure V.8

Framework stability as a function of Al-Al distance related to the location of Ni^{2+} ions in Ni-alumino-silicate Mordenite. The curve is drawn as an eye-guide.

This is in full agreement with the lattice energy minimization calculations performed on siliceous Ni-alumino Mordenite. It can be envisaged that this phenomenon is the reason for the exchange capacity being limited to the occurrence probability of these sequences.

References

1. See e.g. M. Neuber, V. Dondur, H.G. Karge, L. Pacheco, S.Ernst, J. Weitkamp, Proc. Int. Symp. Innovation in Zeolite Materials Science, Elsevier, Amsterdam, 1988, p. 461.
2. Kh. Minachev, Ya. I. Isakov, J.A. Rabo (Ed.), in Zeolites Chemistry and Catalysis, 1976, 171, ACS Monograph.
3. P. Chu, E.G. Dwyer, ACS. Symp. Ser., 1983, 218, p. 59.
4. D.P. Matthews, L.V.C. Rees, Chem. Age India, 1986, 37(5), p. 353.
5. P.A. Maddox, J. Spachursky, J.M. Thomas, Catalysis Letters, 1988, 1, p. 91.
6. J.M. Thomas, C. Williams, T. Rayment, J. Chem. Soc., Faraday Trans. I, 1988, 84, p. 2915.
7. C.R.A. Catlow, W.C. Mackrodt (Eds.), Computer Simulation of Solids, Lecture Notes in Physics, 1982, 166, Springer Verlag.
8. C.R.A. Catlow, M. Doherty, G.D. Price, M.J. Sanders, S.C. Parker, Materials Science Forum, 1986, 7, p. 163.
9. R.A. Jackson, C.R.A. Catlow, Mol. Simulation, 1988, 1, p. 207.
10. R.A. van Santen, A. de Man, B.W. van Beest, Proc. NATO ASI Physicochemical properties of zeolitic systems and their low dimensionality, 1989, Dourdan, France.
11. B.W. van Beest, G.J. Kramer, R.A. van Santen, Phys. Rev. Lett., 1990, 64, p. 1955.
12. W.M. Meier, H.J. Moeck, J. Sol. State Chem., 1979, 27, p. 349.
13. C. Baerlocher, W.M. Meier, H.J. Moeck, Private Communications.
14. W.J. Mortier, J.J. Pluth, J.V. Smith, Mater. Res. Bull., 1975, 10, p. 1037.
15. W.J. Mortier, Compilation of Extra-Framework Sites in Zeolites, Butterworth and Co. Ltd. 1982.
16. W.J. Mortier, J.J. Pluth, J.V. Smith, Natural Zeolites (L.B. Sand and F.A. Mumpton, Eds.), 1978, p. 53.
17. US Patent 3, 702, 886 to Mobil.
18. E.G. Derouane, J.G. Fripiat, Proc. 6ᵗʰ Int. Zeolite Conf., Reno (USA), 1983, p. 717.
19. R.M. Barrer, R.P. Townsend, J. Chem. Soc. Trans. Faraday 1, 1976, 82, p. 661.
20. L. Zhenya, Z. Wangjon, Y. Qin, L. Gaunglie, L. Wangrong, W. Shuju, Z. Youshi, L. Bingxiong, Proc. 7ᵗʰ Int. Zeolite Conf., Elsevier, Amsterdam, 1986, p. 415.

SUMMARY

One of the main applications of zeolites is as a component of heterogeneous catalysts which are being used in several (petro-) chemical processes. Especially the proton forms of zeolites are known to be strong solid acids and hence are used in acid-catalyzed reactions such as cracking of heavy hydrocarbons.

This thesis covers a wide range of molecular phenomena which are of importance in zeolite catalysis research. Subjects under consideration are the synthesis of zeolites, the modification of catalytic properties of zeolites (ion-exchange) and the study of adsorption- and diffusion phenomena in zeolites. The major part of the studies described in the thesis is a combined computational-experimental approach. Although the systems under study may seem rather model-like, the basic concepts following from these studies are directly related to problems encountered in zeolite catalysis.

The theoretical methods used are Monte Carlo statistics, Molecular Dynamics, Lattice Energy Minimization calculations and statistical calculations. Experimental work described cover Pulsed Field Gradient (PFG-) NMR, D-NMR, ^{13}C-NMR, IR and zeolite synthesis.

Chapter II describes a method which can conveniently be used to simulate adsorption in zeolites. The applied method is known as the Monte Carlo technique and the adsorption characteristics of methane in various zeolites are studied. Special attention is paid to the influence of zeolite morphology and temperature. The zeolite structures under consideration are Faujasite, ZSM-5 and Mordenite. It appears that either narrow-pore zeolites (ZSM-5) or zeolites with preferential adsorption sites for methane (Mordenite) yield larger adsorption heat effects than wide-pore zeolites such as Faujasite. This result can be explained by a smaller adsorbate-zeolite interaction in the case of wide-pore zeolites and is graphically visualized by using computer graphics. The temperature effect on the heat of adsorption is analogously explained. The effect of the zeolitic chemical composition (Al/Si ratio and related with this ratio the amount of cations in the zeolite) on the adsorption characteristics appears to be dominated by the presence of (inorganic) cations. These cations may block preferential adsorption sites resulting in a decrease of the heat of adsorption. This effect is much less pronounced for wide-pore zeolites and in this case, electrostatic adsorbate-cation interactions seem to dominate.

In Chapter III, the dynamics of the adsorption process is studied. For this purpose, Molecular Dynamics simulations are being explored. The systems under consideration are methane in ZSM-5, Mordenite, Faujasite and EU-1, xenon in ZSM-5, methane in Mordenite and ethane and propane in ZSM-5. In all these systems, an increase in temperature is accompanied with an increase in adsorbate mobility and a decrease in heat of adsorption. The presence of preferential adsorption sites appears to decrease the adsorbate mobility to a large extent. However, with an increasing zeolite loading, all preferential adsorption sites are gradually filled resulting in an overall increase of adsorbate mobility. The methane in ZSM-5, Mordenite and EU-1 systems are used to study the anisotropy of diffusion. Both Mordenite and EU-1 have one-dimensional channel systems and hence the diffusion is characterized by a strong anisotropic behavior. ZSM-5 on the other hand has a three-dimensional channel system and diffusion can occur in all three directions (x, y, and z). In

ZSM-5, almost no anisotropy in the diffusion is observed. The last part of Chapter III is devoted to the diffusion of larger adsorbates in ZSM-5 such as ethane and propane. Especially the simulation of propane appears to be troublesome which is mainly due to the rigid molecule approximation of the adsorbates making the adsorbate-zeolite interactions rather unrealistic. Whenever possible, all computational results will be compared with experimental data and the interpretation of the simulations will be carried out with these experimental results.

The dynamics of the interaction between occluded template molecules and zeolites in the as-made form after synthesis is studied in Chapter IV. This chapter is a combination between organic synthesis, zeolite synthesis, NMR spectroscopy and computer simulation (Molecular Dynamics). The deuterated template molecule Tetramethylammoniumbromide (TMABr) is synthesized and subsequently used in a zeolite Sodalite synthesis. The zeolite with the deuterated template occluded was subsequently subject to a D-NMR analysis in order to elucidate the TMABr dynamics in the zeolite. Further studies on this subject are carried out by using ^{13}C-NMR. The experiments are interpreted by using Molecular Dynamics in which both the intra-molecular deformations of the TMABr molecule and the zeolite lattice vibrations are taken into account. The D-NMR measurements implicate that the occluded TMABr molecule is able to rotate freely. However, ^{13}C-NMR reveals a hindered rotation of TMABr inside the zeolite void space. The Molecular Dynamics calculations, finally, indeed reveal a large freedom of rotation. However, the observed rotation is more properly described by a "hopping" of the TMABr molecule from one orientation to another during which the symmetry of the TMA-zeolite system is always maintained.

Finally, in Chapter V, the location of exchanged divalent cations (especially Ni^{2+}) in siliceous zeolites is studied. Both experimental and theoretical methods are applied. The exchange capacity of Ni^{2+} cations in Na-ZSM-5 is measured. IR spectroscopy is used to check that the cations are exchanged on ion-exchange positions only. The Ni/Al ratio after exchange is found to be well below the theoretical maximum value of 0.5. This phenomenon is explained with a statistical model which relates the presence of a Ni^{2+} ion to the occurrence of an Al-O-Si-O-Al sequence in the zeolite lattice. The energetical basis of this model is further justified by Lattice Energy Minimization Calculations.

SAMENVATTING

Een van de hoofdtoepassingen van zeolieten is als component van heterogene katalysatoren die gebruikt worden in verschillende (petro-) chemische processen. Zeolieten in de proton-vorm staan bekend als vaste zuren en worden veel gebruikt in zuur gekatalyseerde reacties zoals het kraken van zware koolwaterstoffen.

Dit proefschrift behandelt een breed scala aan moleculaire aspecten die van belang zijn in zeoliet katalyse-onderzoek. Onderwerpen onder beschouwing zijn de synthese van zeolieten, de modificatie van de katalytische eigenschappen van zeolieten (ion-uitwisseling) en de bestudering van adsorptie- en diffusieverschijnselen in zeolieten. Het proefschrift is voor een groot deel een samenspel tussen theorie en experiment. Hoewel de studies wat modelmatig lijken, staan de basisconcepten die uit deze studies volgen in direct verband met problemen binnen het gebied van zeoliet katalyseonderzoek.

De gehanteerde theoretische methoden zijn Monte Carlo statistiek, Moleculaire Dynamica, Roosterenergie Minimalisatie en statistische berekeningen. Experimenten behelsen Pulsed Field Gradient (PFG-) NMR, D-NMR, ^{13}C-NMR, IR spectroscopie en zeolietsynthese.

Hoofdstuk II beschrijft een Monte Carlo methode waarmee adsorptie in zeolieten gesimuleerd kan worden. De adsorptiekarakteristieken van methaan in verschillende zeolieten worden bestudeerd. Er wordt met name aandacht geschonken aan de invloed van zeolietmorfologie en temperatuur. De zeolieten onder beschouwing zijn Faujasiet, ZSM-5 en Mordeniet. Het blijkt dat zeolieten met nauwe porieen (ZSM-5) of zeolieten die sterke adsorptie-sites voor methaan bezitten (Mordeniet) een grotere adsorptiewarmte veroorzaken dan zeolieten met grote porieen (Faujasiet). Deze observatie is te wijten aan een verminderde adsorbaat-zeoliet interactie in het geval van zeolieten met grote porieen. Analoog kan zo ook het effect van temperatuur op de adsorptiewarmte verklaard worden. De invloed van de chemische samenstelling van het zeoliet (Al/Si verhouding en daarmee samenhangend de hoeveelheid aanwezige cationen) op de adsorptiekarakteristieken blijkt gedomineerd te worden door de aanwezige (anorganische) cationen. Deze cationen kunnen sterke adsorptie-sites blokkeren wat resulteert in een afname in de adsorptiewarmte. Bij zeolieten met grotere porieen is dit effect veel minder geprononceerd en dan spelen voornamelijk electrostatische effecten een rol. Deze fenomenen zijn met behulp van computer graphics gevisualiseerd. Bovendien vindt waar mogelijk een vergelijk met experimentele data plaats.

In hoofdstuk III wordt de dynamica van het adsorptieproces bestudeerd met behulp van Moleculaire Dynamica berekeningen. De systemen onder beschouwing zijn methaan in ZSM-5, Mordeniet en EU-1, xenon in ZSM-5, ethaan in ZSM-5 en propaan in ZSM-5. In alle systemen veroorzaakt een toename in temperatuur een afname in de adsorptiewarmte en een toename in adsorbaatmobiliteit wat zich vertaalt in een toename in de diffusiecoefficient. De aanwezigheid van sterke adsorptie-sites blijkt de adsorbaatmobiliteit sterk te reduceren. Echter bij een toenemende zeolietbelading raken al deze adsorptie-sites bezet en wordt een scherpe toename in mobiliteit waargenomen. De anisotropie van de diffusie wordt bestudeerd aan de hand van methane diffusie in ZSM-5, Mordeniet en EU-1. Zowel Mordeniet als EU-1 hebben een een-dimensionaal

kanaalsysteem en derhalve vertoont de diffusie een sterk anisotropisch gedrag. ZSM-5 daarentegen heeft een drie-dimensionaal kanaalsysteem waardoor diffusie in alle richtingen kan plaatsvinden (x, y, en z). In ZSM-5 wordt slechts een zeer kleine anisotropie in de diffusie berekend. Tenslotte wordt in hoofdstuk III de diffusie van grotere adsorbaten zoals ethaan en propaan in ZSM-5 bestudeerd. Met name de simulatie van propaan is problematisch. Dit blijkt vornamelijk te wijten te zijn aan de star-molecuul benadering van propaan waardoor de beschrijving van de interactie tussen het zeoliet en propaan wat onrealistisch is. Evenals in hoofdstuk II worden ook in hoofdstuk III computer graphics gebruikt voor visuele ondersteuning bij de berekeningen. Bovendien worden ook, voor zover mogelijk, alle berekende diffusiekarakteristieken vergeleken met experimentele resultaten.

De dynamica van de interactie tussen geoccludeerde templaatmoleculen en zeolieten na synthese wordt in hoofdstuk IV bestudeerd. Dit hoofdstuk beschrijft een gecombineerde studie waarin organische synthese, zeolietsynthese, NMR spectroscopie en computersimulatie centraal staan. Het gedeutereerde templaatmolecule Tetramethylammoniumbromide (TMABr) is gesynthetiseerd met als doel om met dit gedeutereerde templaat zeoliet Sodaliet te synthetiseren. Dit zeoliet met het geoccludeerde templaat wordt vervolgens gebruikt om de dynamica van het TMA in het zeoliet middels D-NMR te bestuderen. Verder worden er ook ^{13}C-NMR metingen verricht ter verdere bestudering van de dynamica van het TMA. De experimenten worden geinterpreteerd met behulp van Moleculaire Dynamica berekeningen waarin zowel de interne bewegingen van TMA als de zeolietroostervibraties meegenomen zijn. De NMR studies laten een vrijwel vrij roterend TMA ion in het zeoliet zien. Echter, ^{13}C-NMR toont aan dat de rotatie van het geoccludeerde TMA gehinderd is. De Moleculaire Dynamica berekeningen tonen inderdaad aan dat TMA een vrij grote mate van rotatievrijheid heeft, maar dat de rotatie beschreven dient te worden als het "springen" van de ene orientatie naar een andere waarbij de symmetrie van het TMA-zeoliet systeem altijd bewaard blijft.

Tenslotte wordt in hoofdstuk V de locatie van uitgewisselde twee-waardige metaalionen (met name Ni^{2+}) in hoog-silica zeolieten bestudeerd. De gehanteerde methoden zijn zowel theoretisch als experimenteel van aard. De uitwisselingscapaciteit van Ni^{2+} ionen in hoog-silica ZSM-5 wordt gemeten. IR spectroscopie wordt gebruikt om na te gaan dat de cationen uitsluitend op ion-uitwisselingsposities gelocaliseerd zijn. De Ni/Al verhouding na uitwisseling blijft ver onder de theoretische waarde van 0.5. Deze observatie wordt verklaard met een statistisch model wat de aanwezigheid van een Ni^{2+} ion op een bepaalde plaats relateert aan het voorkomen van een Al-O-Si-O-Al sequentie in het zeolietrooster. De energetische basis van dit model wordt geverifieerd met Roosterenergie Minimalisatie berekeningen.

Nawoord

Toen ik in maart 1987 afstudeerde in de Chemie stond ik voor de keuze om of te promoveren aan het instituut voor Fundamenteel Onderzoek der Materie (FOM) in Amsterdam of in deze zelfde stad te gaan werken in een van s'werelds grootste industriele laboratoria, namelijk het Koninklijke/Shell Laboratorium, Amsterdam (KSLA). Ik heb voor het laatste gekozen en daar geen moment spijt van gehad. Het zij echter wel opgemerkt dat toendertijd de keuze mij bijzonder zwaar viel. Ik was namelijk ambitieus genoeg om een doctorstitel na te streven. Dat deze ambitie is gebleven in de loop van de tijd moge blijken uit dit proefschrift dat thans voor U ligt. Dat dit proefschrift tot stand is gekomen berust echter voor het merendeel op louter toeval; het is nooit mijn intentie geweest, noch die van het KSLA management, om aan het KSLA te promoveren. Echter, toen de kans zich voordeed heb ik de gelegenheid met beide handen aangegrepen.

Promoveren doe je niet alleen, zo heb ik kunnen ervaren. Onderzoek doen is jezelf deels afhankelijk stellen van anderen voor morele en technische steun. Allereerst wil ik Karin noemen. Dat dit proefschrift aan jou is opgedragen zegt genoeg. Bedankt voor je steun en begrip. Mijn ouders dank ik voor hun goede zorgen en voor het scheppen van de mogelijkheden dat ik kon studeren. Ik ben het gehele KSLA zeer erkentelijk voor het feit dat mij de mogelijkheid werd geboden om fundamenteel onderzoek te doen en om dit werk te publiceren. Met name wil ik enige directe collega's noemen.

In de eerste plaats dank aan Berend Smit. Jouw wetenschappelijke inbreng is groot geweest en bovendien heb jij mij ertoe aangezet om dit proefschrift te schrijven. Klaas-Pieter Datema, ik denk met zeer veel plezier aan onze samenwerking terug. Foppe Visser, hetzelfde geldt voor jou; onze discussies achter de terminal waren diepgaand, zowel wetenschappelijk als persoonlijk. Andreas Nowak, ik heb je als post doc ontmoet aan de Royal Institution in Londen en vervolgens ben je een collega geworden; bedankt voor je wetenschappelijke inbreng en ook voor de grandioze tijden die ik heb mogen beleven in Londen. Collega's van me die op de afdeling werkten waar ik ter werk gesteld werd toen ik pas bij Shell begon: Jan Keijsper, Ton Wielers en Peter Lednor, jullie hebben ertoe bijgedragen dat mijn 'CGP-tijd' onvergetelijk is geworden. Herman Kuipers, bedankt voor je inspirerende discussies. Munro Mackay, bedankt voor je assistentie. Van mijn overige collega's wil ik noemen: Wessel Ijlstra, Dik de Bruyn, Renee Driessen (UVA) en Gert-Jan Kramer.

Gedurende de werkzaamheden beschreven in dit proefschrift heb ik veel contacten buiten KSLA gehad. Deze contacten heb ik altijd als plezierig en nuttig ervaren. Dank aan Marinus Vaarkamp (TUE), Rob Jackson (University of Keele, UK), Prof. Catlow (University of Keele, UK), Prof. Thomas (Royal Institution, London), Steve Pickett (Royal Institution, London), Laurens Siebeles (FOM, Amsterdam), en Ineke Korevaar van den Dries (Shell) die mij zo bijgestaan heeft in de moeilijke uren die het printen van dit proefschrift teweeg hebben gebracht.

Tenslotte wil ik de personen bedanken die mij zeer intensief begeleid hebben gedurende het werk en het schrijven aan dit proefschrift. Allereerst Martin Post. Martin, gedurende de gehele

periode ben jij mijn directe chef geweest. Wij hebben vaak langdurige wetenschappelijke discussies gevoerd vaak onbeslist eindigend of in remise omdat ik te koppig was om toe te geven. Hoe dan ook, ik heb van je geleerd om accuraat en solide de wetenschap te bedrijven en ik ben je daar zeer dankbaar voor. Prof. Tony Cheetham (University of Oxford). Tony, it was a great pleasure and honor for me having you as my second supervisor. Tenslotte Prof. Rutger van Santen. Rutger, bedankt voor je intensieve en gedegen begeleiding. Zonder jou zou dit proefschrift niet in de huidige vorm gereed zijn gekomen.

Curriculum Vitae

Constantinus Johannes Jacobus den Ouden werd op 30 mei 1961 te Dordrecht geboren. In 1977 behaalde hij het eindexamen MAVO aan de Kardinaal de Jong MAVO in Zaandam. Daarna behaalde hij het eindexamen HAVO in 1979 en Atheneum in 1981 beide aan het Blaise Pascal College in Zaandam.

In augustus 1981 begon hij de studie Chemie aan de Vrije Universiteit van Amsterdam alwaar hij in 1984 het candidaatsexamen aflegde. Zijn afstudeeronderzoek vond plaats in de vakgroep Fysische en Theoretische Chemie onder leiding van Prof. Dr. C.A. de Lange en Prof. Dr. E.J. Baerends en betrof de beschrijving van orientatieverschijnselen van kleine moleculen opgelost in vloeibare kristallen middels NMR spectroscopie. Daarnaast heeft hij zich beziggehouden met de ontwikkeling en implementatie van een nieuwe numerieke procedure om integraties in quantumchemische berekeningen uit te voeren. In maart 1987 legde hij het doctoraalexamen Chemie met bijvak Theoretische Fysica met goed gevolg af.

In april 1987 trad hij in dienst bij Shell. Hij werd gestationeerd op het Koninklijke/Shell Laboratorium, Amsterdam waar hij zich gedurende de eerste drie jaar heeft beziggehouden met het introduceren en integreren van rekenkundige methoden in zeoliet katalyse en synthese onderzoek. De studies die hij daarvoor uitvoerde zijn in dit proefschrift beschreven.

In maart 1988 startte hij naast zijn werkzaamheden de studie Chemische Technologie aan de Technische Universiteit van Twente. In September 1990 behaalde hij het ingenieursexamen. Het onderwerp van zijn afstudeeronderzoek behelsde de studie en modellering van industriele kristallisatieprocessen en werd onder toezicht van Prof. Dr. Ir. T. Reith uitgevoerd.

Sinds maart 1990 is hij binnen Shell werkzaam als chemicus en procestechnoloog op het gebied van petroleum residu-hydroconversie. Zijn taken behelsen katalysatoronderzoek en procesontwikkeling.

STELLINGEN

behorende bij het proefschrift

COMPUTATIONAL STUDIES IN ZEOLITE SCIENCE;

AN INVESTIGATION OF GUEST-HOST INTERACTIONS

van

C.J.J. den Ouden

1. Interferentietermen verschijnen in de quantummmechanische uitdrukking van een observabele doordat de golffunctie van het beschouwde systeem wordt geschreven als een superpositie van golffuncties, die eenvoudiger systemen dan het beschouwde systeem beschrijven.

    L.D.A. Siebeles
    Private Communications

2. Het is niet ondenkbaar dat met *in situ* NMR metingen van de omzetting van koolwaterstoffen in zeolitische katalysatoren nieuwe inzichten worden verkregen die direct kunnen leiden tot optimalisatie van bestaande productieprocessen.

    M.W. Anderson, J. Klinowski
    Nature, 1989, 339, 200

3. Het is aannemelijk dat de fase overgang van α-quartz naar ß-quartz wordt geinduceerd door een met de temperatuur toenemende ioniciteit van de Si-O binding.

    B.W.H. van Beest, G.J. Kramer, R.A. van Santen
    Phys. Rev. Lett., 1990, 64, 1955

4. Waterstofbrugvorming kan van doorslaggevende betekenis zijn voor micelvorming. Uit recente computersimulaties blijkt het echter geen voorwaarde te zijn.

    A.H. Beesley, D. Fennell Evans, R.G. Laughlin
    J. Phys. Chem., 1988, 92, 791
    B. Smit, P.A.J. Hilbers, K. Esselink, L.A.M. Rupert, N.M. van Os, A.G. Schlijper
    Nature, 1990, 348, 624

5. De synthese route van niet-oxidische materialen zoals nitriden en carbiden via vloeistofreacties is tot nu toe weinig geexploreerd. Gezien de veelzijdigheid in morfologie en textuur, en daarmee samenhangend de veelzijdigheid in toepassingen, van oxidische materialen die vanuit oplossing gevormd kunnen worden, dient deze bereidingswijze voor niet-oxidische materialen meer aandacht te krijgen.

    R.W. Chorley, P.W. Lednor,
    Advanced Materials, in press

6. Moleculaire Dynamica simulaties blijken geschikt te zijn om zelfdiffusie van geabsorbeerde moleculen in zeolieten te beschrijven. De uitbreiding van dergelijke simulaties naar het gas-vaste stof grensvlak is eenvoudig te realiseren en kan leiden tot een beter begrip van diffusie van moleculen in zeolietkristallen waarbij een concentratiegradient de drijvende kracht is.

    Dit proefschrift, hoofdstuk III

7. Evenals bij de omzetting van substraten door enzymen is ook bij de synthese van zeolieten met behulp van templaatmoleculen het systeem niet alleen te beschrijven op grond van de moleculaire geometrie. In beide gevallen spelen ook de dynamische aspecten van de interacties een belangrijke rol.

    Dit proefschrift, hoofdstuk IV

8. Een stelling die betrekking heeft op een foutieve meting of interpretatie van een collega wetenschapper dient argwaan op te roepen; zij komt doorgaans voort uit gemakzucht van de bedenker van de stelling.

9. Het is niet aan te bevelen om Hermans' roman *Nooit Meer Slapen* te lezen alvorens met een promotie-onderzoek te beginnen.

    W.F. Hermans in *Nooit Meer Slapen*, 15de druk.
    Uitgeverij De Bezig Bij, Amsterdam, 1979.

10. Een mens verraadt zich in de bijwoorden.